UNIVERSITÀ DEGLI STUDI DI PADOVA

Dipartimento di Scienze Chimiche

Corso di Laurea Magistrale in Scienza dei Materiali

Tesi di Laurea

Investigating interphases modification *via* ethylene carbonate derivatives in high voltage NMC622||graphite lithium-ion batteries by *operando* SHINERS

Relatore: Prof. Christian Durante

Correlatore: Dr. Masoud Baghernejad (Helmoltz Institute Münster)

Controrelatore: Prof. Denis Badocco

LAUREANDA Griggio Angela

Matricola 2004655

ANNO ACCADEMICO

2022 - 2023

This page was intentionally left blank

This page was intentionally left blank

“Fall in love with some activity, and do it! Nobody ever figures out what life is all about, and it doesn't matter. Explore the world. Nearly everything is really interesting if you go into it deeply enough. Work as hard and as much as you want to on the things you like to do the best. Don't think about what you want to be, but what you want to do. Keep up some kind of a minimum with other things so that society doesn't stop you from doing anything at all.”

— Richard P. Feynman

Dedicata a mia nipote Lia

-

Dedicated to my niece Lia

ABSTRACT

Solid Electrolyte Interphase (SEI) has a crucial role in lithium-ion battery performance. In batteries with NMC positive electrode with excess Nickel as $LiNi_{0.6}Mn_{0.2}Co_{0.2}O_2$ (NMC622), especially when operated at high voltage (> 4.3 V), the dissolution of transition metals and cross-talk to the negative electrode can lead to SEI damage, rendering the formation of an effective SEI even more important to extend battery lifetime. The incorporation of additive molecules in the electrolyte can favor the formation of stable and effective interphases. In this work the electrochemical performance of four ethylene carbonate-derivative additives, namely fluoro-, chloro-, vinyl-, ethylene carbonate and vinylene carbonate (FEC, ClEC, VEC and VC, respectively) is studied in NMC622||graphite pouch cells operated to a cut-off voltage of 4.5 V, in tandem with morphology analysis of the aged electrode and gas chromatography-mass spectrometry (GC-MS) study of the electrolyte. Improved cycle life and reduced impedance were found for VEC-containing cells, even though products of electrolyte degradation were identified by gas chromatography-mass spectrometry. Additionally, for ClEC, which shows the best capacity performance, but shorter cycle life and reduced Coulombic efficiency, multiple degradation products are shown by GC-MS. Moreover, SEI understanding is still hindered by its reactivity towards the air, its nanometric thickness, and the possible mechanical damage following battery disassembly. Therefore, to gain real-time information about the SEI, *operando* Shell-isolated nanoparticles enhanced Raman spectroscopy (SHINERS) was performed.

Contents

TABLE OF FIGURES 3
LIST OF TABLES 5
LIST OF ABBREVIATIONS 6
1 INTRODUCTION 8
2 BATTERIES: BASIC PRINCIPLES AND MATERIALS 10
2.1 LITHIUM ION BATTERY (LIB) 10
2.2 NEGATIVE ELECTRODE 12
2.3 POSITIVE ELECTRODE 15
2.4 ELECTROLYTE 18
2.5 INTERPHASE 20
3 NMC CHALLENGES AT HIGH VOLTAGE 24
4 ETHYLENE CARBONATE DERIVATIVE ADDITIVES 27
5 *OPERANDO* SHINERS 34
3.5 RAMAN 34
5.1.1. ENHANCED RAMAN SPECTROSCOPIES 37
5.1.2. APPLICATION IN INTERPHASE STUDY 39
6 MOTIVATION 42
7 MATERIALS AND METHODES 43
5.1 CHEMICALS AND MATERIALS 43
5.2 ELECTROLYTE PREPARATION 44
5.3 CELL ASSEMBLY 44
5.3.1 ELECTRODE PREPARATION 44
5.3.2 SWAGELOK® CELL ASSEMBLY 44
5.3.3 LI-FUN PREPARATION 45
5.4 POTENTIOSTATIC INVESTIGATION 45
5.5 GALVANOSTATIC CYCLING 45
5.6 ELECTROCHEMICAL IMPEDANCE SPECTROSCOPY (EIS) 46
5.7 ANALYSIS OF AGED COMPONENTS 46
5.7.1 GAS CHROMATOGRAPHY - MASS SPECTROMETRY (GC-MS) AND HIGH RESOLUTION-ACCURATE MASS SPECTROMETRY (HRAM-MS) 46
5.7.2 SCANNING ELECTRON MICROSCOPY (SEM) AND ENERGY DISPERSIVE X-RAY (EDX) 47
5.8 NANOPARTICLE SYNTHESIS 48
5.9 RAMAN-SAMPLE PREPARATION 48
5.10 RAMAN ANALYSIS 49

8 RESULTS AND DISCUSSION ____ 50
8.1 ELECTROCHEMICAL INVESTIGATION ____ 50
8.2 SURFACE STUDY ____ 59
8.3 ELECTROLYTE DECOMPOSITION INVESTIGATION ____ 60
8.4 *OPERANDO* SHINERS ____ 64
9 CONCLUSION AND OUTLOOK ____ 68
10 BIBLIOGRAPHY ____ 69
11 AKNOWLEDGEMENTS ____ 87
12 APPENDIX ____ 90

TABLE OF FIGURES

Figure 1: Lithium-ion battery scheme, showing its operation. Graphite negative electrode on copper current collector is on the left, layered oxide positive electrode on aluminum is on the right. The dotted lines represent the separator. At the bottom the reactions for the charge process are reported.[11] _____ 11
Figure 2: Different geometries for battery cells a) cylindrical, b) prismatic, c) pouch (adapted from [13]) and d) coin. (Adapted from[10]) _____ 11
Figure 3: Crystal structure of the main negative electrode materials lithiated, as in the battery charged state. a) graphite, b) lithium titanate, c) silicon. [16] _____ 12
Figure 4: a) SEM micrograph indicating the basal and edge planes of graphite.[23] **b)** Stages of electrochemical intercalation of lithium into graphite.[20] _____ 13
Figure 5: Main degradation mechanisms of Si electrodes originating from the large volume expansion of Si during lithiation.[13] _____ 14
Figure 6: Comparison of main cathode materials classes in terms of potential and specific capacity. LCO stands for ''lithium cobalt oxide'', LMO for ''lithium manganese oxide'', NCM for ''nickel cobalt manganese oxide'', NCA for ''nickel cobalt aluminum oxide'' LFP for ''lithium iron phosphate''. Additionally to the materials discussed in the text, LCP stands for ''lithium cobalt phosphate'', LFSF for ''lithium iron fluorosulfate'', and LTS for ''lithium titanium sulfide". (Adapted from [16]) _____ 15
Figure 7: Crystal structure of the three main classes of materials applied as positive electrodes: **a)** 1D olivine **b)** 2D layered **c)** 3D spinel. In yellow are lithium ions, in blue oxygen and in red TM (or phosphorous in one-eight of the tetrahedral sites of olivine). [43] _____ 16
Figure 8: Plot of thermal stability, discharge capacity and capacity retention for different stochiometries of NMC. [50] _____ 17
Figure 9: **a)** Mosaic model of the SEI.[83] **b)** Schematic structure of SEI.[77] _____ 20
Figure 10: a) Reduction of EC and EMC to form semicarbonates.[12] **b)** EC reduction to CO_3^- radical and ethene, and ring attack by the radical anion to form alkyl carbonates. [12] **c)** ring opening at the acyl oxygen. [57] _____ 23
Figure 11: Specific energy of NMC111||graphite, NMC622||graphite and NMC811||graphite cells in 1 M $LiPF_6$ in EC:EMC (3:7 v/v). The full columns represent the specific energy of the 5th cycle (1 C-rate), the dashed part of the columns of the 300th cycle (1 C-rate). [115] _____ 25
Figure 12: a) Structures of VC decomposition products deduced from NMR.[136] **b)** Calculated pathway for oligomer formation from VC.[137] **c)** Proposed VC reduction pathways based on synthesis of reduction products.[140] _____ 29
Figure 13: a) Ring opening of FEC. **b)** Polymerization of FEC to poly(FEC) **c)** Cross-linking mechanism of poly(FEC). (Adapted from [152]) _____ 30
Figure 14: VEC reduction pathways calculated by DFT. [157] _____ 32
Figure 15: **a)** Proposed radical initiators for VEC polymerization formed by anodic oxidation.[158] **b)** Ring opening and further possible reaction pathways of VEC (R': CH=CH2) (Adapted from [159]) ___ 33
Figure 16: The potential energy diagram comparison of anharmonic and harmonic oscillator.[169] _ 34
Figure 17: Example of a dipole moment varying around a_0.[169] _____ 35
Figure 18: Schematic illustration of Rayleigh scattering as well as Stokes and anti-Stokes Raman scattering. The laser excitation frequency (n_L) is represented by the upward arrows and is much higher in energy than the molecular vibrations. The frequency of the scattered photon (downward arrows) is unchanged in Rayleigh scattering but is of either lower or higher frequency in Raman scattering.[169] _____ 36

Figure 19: Scattering, absorption, extinction, and local field efficiencies (Q_{sca}, Q_{ABS}, Q_e, Q_{NF}, respectively) for a silver nanoparticle with radius a = 22 nm immersed in water. These quantities are proportional to the corresponding cross-sections (Q =σ/πa2). [172] 38
Figure 20: Li-FUN cell holder schematic. [187] 46
Figure 21: Schematic of the optical Raman cell (Adapted from [75]) 49
Figure 22: First and second cycle of CV in NMC622||graphite three electrode Swagelock T cell, with NMC as WE. For each electrolyte, additive concentration is 0.5 M and scan rate is 150 µV/s. 51
Figure 23: Specific discharge capacity and Coulombic efficiencies of the tested concentrations as reported in the legend in picture for **a)** VEC **b)** ClEC **c)** FEC and **d)** VC 53
Figure 24: a) Discharge capacity, **b)** normalized capacity (state of health), **c)** initial Coulombic efficiency, **d)** accumulated energy for the optimum concentration of each additive. 55
Figure 25: a) Differential capacity plot (dQ/dV) for the first charge of cells with optimum additive concentration. **b)** First cycle of CV in Li-metal||graphite three electrode Swagelock T cell, with graphite as WE. For each electrolyte, additive concentration is 0.5 M and scan rate is 150 µV/s. Dotted lines indicate the onset of the peak, defined as the potential where the current grows over - 0.05 mA 56
Figure 26: a) Nyquist plots of the full NMC622||graphite Li-FUN cell, at 3.8 V (50% SOC) during the first and 100th charge after formation for optimum additives concentration and reference and the obtained fit, as reported in the legend. **b)** Difference between average charge and discharge voltage ΔV, for optimum concentration of each additive and reference. 58
Figure 27: Scanning Electron Microscopy images of graphite anodes respectively **a)** pristine**,** or after 100 cycles in **b)** reference **c)** VEC **d)** ClEC **e)** FEC **f)** VC electrolytes with optimum additive concentration. **g)** Energy dispersive X-ray images of graphite anodes cycled in ClEC containing additive 59
Figure 28: Comparison of GC-MS chromatograms of the electrolytes recovered from galvanostatically charged/discarged NMC622||graphite Li-FUN cells: **a)** for optimum concentrations of each additive and reference after 100 cycles; **b)** for each additive and reference after formation (light colors) and after 100 cycles (saturated colors), focusing on the retention times of the investigated additives; **c)** for ClEC, after 100 cycles, after formation and the pristine electrolyte, limited to retention times of CLEC's decompositions products. **d)** Mass spectra of the fragment pattern obtained by electron ionization at the retention times corresponding to peaks 1, 2 and 3 in the chromatogram in c. **e)** Extracted ion chromatograms of the characteristic chlorine containing $[M+NH_4]^+$ adducts formed by chemical ionization using ammonia as reagent gas, selected m/z of 156.0422 and 158.0392 were extracted with a mass window of 5 ppm. **f)** Proposed structures of the three individuated compounds. 62
Figure 29: SHINERS spectra at OCP and -4.5 V for **a)** reference, **b)** VC, **c)** FEC, **d)** ClEC, **e)** VEC acquired with 10% laser power (wavelength reported in Fig.A10), 30 s and 5 acc., baseline subtracted and smoothed with LabSpec6. 65

Figure A 1: a) Specific discharge capacity for the reference electrolyte obtained from the two different cycling procedures applied. **b)** Measured NMR of the BrEC additive in DMSO (red) and calculated NMR of BrEC from NIST database (black) **c)** Specific discharge capacity tmEC 0.15 M and 0.5 M **d)** CV of tmEC containing additive and reference, with aged indicating the electrolyte stored in dryroom for 2 weeks. 90
Figure A 2: a) CV of CF_3EC containing additive and reference **b)** Specific discharge capacity for CF3EC investigated concentrations and reference **c)** Difference between average charge and discharge voltage ΔV for CF3EC 91

Figure A 3: Complete range data **a)** discharge capacity, **b)** normalized capacity (state of health), **c)** accumulated energy for the optimum concentration of each additive. 91
Figure A 4: ΔV for each investigated concentration **a)** VEC, **b)** ClEC, **c)** FEC, **d)** VC 92
Figure A 5: a) dQ/dV plot for the first charge of VEC investigated concentrations **b)** Average cell voltage during charge and discharge. 92
Figure A 6: Nyquist plot for each cycle at 50% SOC during charge for reference and each additive optimum concentration. 93
Figure A 7: Equivalent circuit used to fit EIS data. Block A models the ohmic resistance of the electrolyte. Block B is to take in account inductive effects of the external circuitry and from cell geometric effects, evident for data points with -Z"< 0. Block C reproduces the semicircles with so-called ZARC elements, describing the dynamics of the double layer and the charge transfer. 94
Figure A 8: Scanning Electron Microscopy images of graphite anodes respectively **a)** pristine**,** or after 100 cycles in **b)** reference **c)** VEC **d)** ClEC **e)** FEC **f)** VC electrolytes with optimum additive concentration. 95
Figure A 9: HRAM-MS fragment pattern for ClEC decomposition products 95
Figure A 10: Unelaborated SHINERS spectra of graphite surface for **a)** Ref (OCP, -4.5 V 30 min red laser, others green laser), **b)** VC (red laser) **c)** FEC (-2.4 V green laser, others green laser) **d)** ClEC (OCP, -4.5 V 30 min red laser, others green laser) **e)** VEC (OCP, -2.4 V red laser, others green laser) at -2.4, -3 and - 4.5 V vs NMC. **f)** Microscope image of graphite surface before and after charge, acquired from the Raman microscope at OCP and at the end of charge in the optical cell. 96
Figure A 11: Spectra of the pure reference electrolyte and pure additives. Baseline corrected with LabSpec 6.6.2. software. All acquired at 100% laser power. Reference red laser, 10 s, 5 acq., FEC red laser, 10 s, 3 acq., ClEC red laser 30 s 3 acq., VC green laser 30 s, 3 acq, VEC green laser, 10 s 3 acq.. Dashed lines indicate EC and PF_6^- peaks as assigned in the figure. Peaks non assigned in reference spectra belong to EMC.[176] 97

LIST OF TABLES

Table 1: Overview of the chemicals and materials used within the thesis comprising information about supplier and purity 43
Table 2: Structure, name and abbreviation of the used additives. Weight and molar concentration of the additives in the prepared electrolytes 44

Table A 1: Values of Resistance (R), Q and α of CPE elements from the fitted set of EIS data 94

LIST OF ABBREVIATIONS

ATR-FTIR attenuated total reflectance fourier-transform infra red

BrEC bromoethylene carbonate

CE counter electrode

CEI cathode electrolyte interface

CF_3EC trifluoromethyl ethylene carbonate

ClEC chloroethylene carbonate

CPE constant phase element

CV cyclic voltammetry

DEDOHC 2,5-dioxahexanedioic acid diethyl ester

DFT density functional theory

EC ethylene carbonate

EDX energy dispersive x-ray

EIS electrochemical impedance spectroscopy

EMC ethylene methylene carbonate

EV electric vehicles

FEC fluoroethylene carbonate

GC-MS gas chromatography-mass spectrometry

HRAM-MS high resolution-accurate mass spectrometry

LEC lithium ethylene carbonate

LEDC lithium ethylene dicarbonate

LFP $LiFePO_4$

LIB lithium-ion battery

LMC lithium methylene carbonate

LMNO $LiNi_{0.5}Mn_{1.5}O_4$

LMO $LiMn_2O_4$

LSPR localized surface plasmon resonance

LTO lithium titanate

NCA $LiNi_xCo_yAl_zO_2$

NMC $LiNi_xMn_yCo_zO_2$

NMR nuclear magnetic resonance

OD optical density

PC propylene carbonate

RE reference electrode

Ref reference electrolyte

SEI solid electrolyte interphase

SEM scanning electron microscopy

SERS surface enhanced Raman spectroscopy

SHINERS shell-isolated nanoparticle enhanced Raman spectroscopy

SOC state of charge

SOH state of health

SOTA state of the art

TERS tip-enhanced Raman spectroscopy

TM transition metals

tmEC tetramethyl ethylene carbonate

VC vinylene carbonate

VEC vinyl ethylene carbonate

WE working electrode

XPS x-ray photoelectron spectroscopy

XRD x-ray diffraction

1 INTRODUCTION

Energy storage covers an important role in fighting climate change, reducing air pollution, and building a more sustainable economy by limiting dependence on fossil fuels. This is also acknowledged by the strategy of the European Union towards the objective of zero net emissions of greenhouse gases by 2050 and reduction of them at a minimum of 55% by 2030, compared to 1990 levels.[1] Both stated sub-goals of obtaining 40% of the energy mix from renewable energy by 2030 and to set at zero emissions from new cars by 2035 require the increase in production and efficiency of rechargeable electrochemical energy storage systems necessary for grid stability and electric vehicles.

Batteries are just one of the main electrochemical storage technologies, together with supercapacitors and fuel cells, which are complementary in terms of power and energy density, so that none of them can satisfy all the requirements for every application.[2–4] Battery technology has attracted a growing interest, as shown by the increasing number of publications in the field, which has grown 4.5 times faster than general published literature between 2010 and 2017.[5]

After its first commercialization in 1991 by Sony, lithium-ion batteries (LIB) were initially applied mostly in portable electronics, thanks to their exceptional low weight and high energy density compared to other battery chemistries such as nickel-cadmium (Ni-Cd) or nickel-metal hydride (Ni-MH).[5] Although Ni-Cd batteries present good rate capability, good performance at low temperatures and long lifetime, the presence of a “memory effect” limits the available capacity over time, while nickel-metal hydride systems that do not present this issue are limited in power performance.[3] Despite the concerns for safety in abuse conditions and capacity degradation, LIBs have become attractive and replaced the other chemistries for a large range of applications, including, for example, power tools and uninterruptible power supplies. Nowadays, LIBs development is driven by the design requirements of electric vehicles (EV), since 43% of the manufactured LIBs was directed to this market already in 2016, with the prevision of reaching 50% in 2025.[5]

Materials development for this application has been directed towards meeting the demands for longer ranges, requiring a higher energy density and a higher capacity, while maintaining a good lifetime by reducing capacity fading and processes leading to cell failure. In addition, other relevant factors addressed are cost, safety, and charging speed.[6]

Besides developing new and improved electrode materials, investigating new electrolyte formulations is a key aspect of battery research. The composition of the electrolyte influences the reactivity at the electrode/electrolyte interface, while the addition of modified additives allows the formation of modified interphases with tailored properties. The study of these interphases however, requires the application of advanced techniques.[7, 8]

2 BATTERIES: BASIC PRINCIPLES AND MATERIALS

2.1 LITHIUM ION BATTERY (LIB)

Lithium-ion batteries are secondary battery devices, meaning that they have the capability to be reversibly charged and discharged. Battery devices have a sandwich structure in which active materials with different standard potentials are deposited on metallic current collectors, for instance, graphite on copper for the anode and $LiCoO_2$ on aluminum for the cathode. To avoid short-circuiting, in between the electrodes there is a polymeric or ceramic layer working as separator. The separator is soaked in an electrolyte that coordinates the cations enabling ion transport, which in state-of-the-art LIB is typically a mix of organic carbonates containing a lithium salt. The cell voltage depends on the difference in the electrochemical potential of the electrode materials.

Before the development of lithium-ion batteries, different chemistries were applied for rechargeable systems, such as Ni-Cd. Electrodes were based on the respective hydroxides, and it used proton as exchanged cation in water-based alkaline electrolytes, thus limiting the voltage window to 1.25 V due to electrolysis reaction.[9] Since lithium has the lowest standard potential and the lowest weight, it is an ideal candidate for storage systems with high energy densities. Lithium based batteries were enabled by the discovery of materials able to intercalate alkali metals reversibly, and required the use of organic electrolytes due to lithium reactivity.[10]

In state-of-the-art (SOTA) LIB, the positive electrode is usually constituted of particles of layered lithium transition metal (TM) oxides, mixed with carbon for increased electronic conduction and a polymeric binder, while graphitic carbon is used as the negative electrode.[11] The linear and cyclic carbonates used as electrolyte solvents are respectively, for example, ethylene carbonate (EMC) or propylene carbonate (PC) and ethylene methylene carbonate (EMC) or dimethylene carbonate (DMC), in which a lithium salt is dissolved. [12]

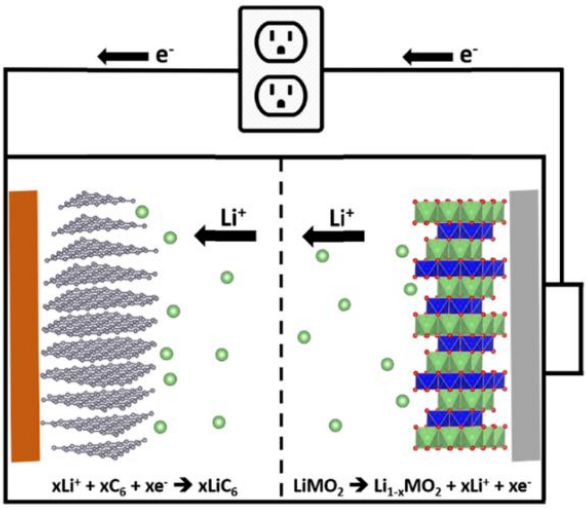

Figure 1: Lithium-ion battery scheme, showing its operation. Graphite negative electrode on copper current collector is on the left, layered oxide positive electrode on aluminum is on the right. The dotted lines represent the separator. At the bottom the reactions for the charge process are reported.[11]

During the charging process, the positive and negative active materials are respectively oxidized and reduced according to the reactions reported in **Figure 1**. Those are reversible and take place the other way around during discharge. More in detail, under the application of an external current, lithium ions are extracted by the positive electrode, the transition metals are oxidized, and lithium, transported through the electrolyte, is intercalated in the graphite, which gets reduced. In the first charge/discharge cycle the electrolyte is also oxidized at the positive electrode and reduced at the negative one, forming interphases from decomposition products of the electrolyte componenets on the electrode´s surface. In an ideal case, the formed interphases allow subsequent stable cycling without further electrolyte decomposition and limited influence on Li-diffusion processes.

The electrode layers can then be arranged in different geometries to optimize the material usage, to form cylindrical, prismatic or pouch cells, as shown in **Figure 2**. Pouch cells can also have wound electrodes similarly to prismatic ones.

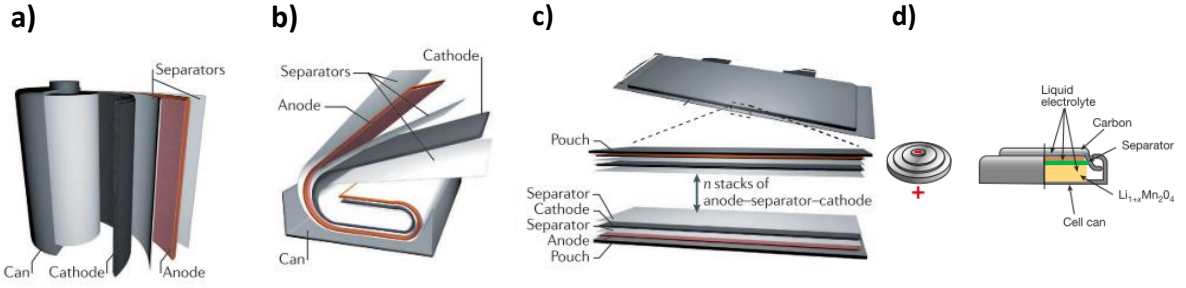

Figure 2: Different geometries for battery cells a) cylindrical, b) prismatic, c) pouch (adapted from [13]) and d) coin. (Adapted from[10])

2.2 NEGATIVE ELECTRODE

Lithium-based secondary batteries initially used lithium metal as negative electrode. With its very low redox potential (-3.04 V vs standard hydrogen electrode) and high theoretical specific capacity (3,860 mAh/g), it enables the highest cell voltage and energy density. Therefore, a lot of research is still directed at elaborating methods to introduce it in practical devices.[14] Nevertheless, its application is hindered by safety hazards caused by non-uniform lithium deposition, forming metallic dendrites, piercing the separator and leading to complete self-discharge and eventually to thermal runaway of the cell. Moreover, the severe consumption of active lithium and increased electrolyte decomposition for SEI formation on the surface of the negative electrode accounts for the poor cycle life of Li-metal batteries.[15]

An important step that led to the commercialization of lithium-ion batteries was Yoshino's introduction of petroleum coke as negative electrode in 1985.[5] Since then, mainly carbonaceous materials have been employed as active material for the anode, due to their low redox potential, high specific capacity and dimensional stability, as well as low cost and widespread availability.[17, 18] Other materials that are applied as negative electrodes are the spinel $Li_4T_5O_{12}$ (LTO), also based on lithium intercalation, or alloying materials such as silicon, germanium and tin.[16]

Carbonaceous materials can be divided in graphitic and non-graphitic, based on the level of order, even if a definite threshold does not exist and the so-called graphites also contain a variable ratio of crystalline and amorphous domains. Both amorphous carbon and graphite can be obtained naturally or synthesized from by-products of the petroleum and coal industry.

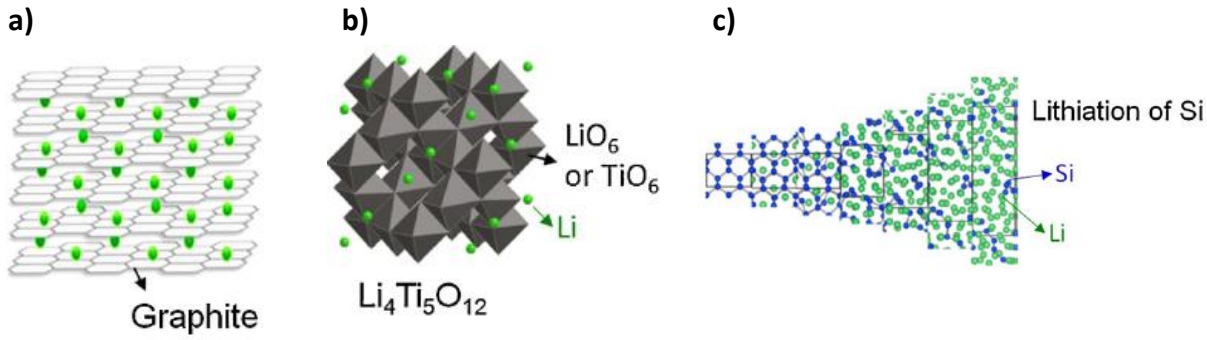

Figure 3: Crystal structure of the main negative electrode materials lithiated, as in the battery charged state. a) graphite, b) lithium titanate, c) silicon. [16]

Crystallinity, microstructure, and micromorphology of the carbonaceous material affect the quality of sites for lithium intercalation and eventually its theoretical capacity. Coke carbon was lately substituted for graphite, once the challenge of exfoliation was overcome by the incorporation of EC in the electrolyte[19], because of its high intercalation potential and lower capacity.[20] However, amorphous carbons could be a possibility for high-rate applications.[18]

Nowadays, graphite is the most utilized anode material due to its theoretical gravimetric and volumetric capacity of 372 mAh/g and 850 mAh/cm^3. It is formed by stacked layers of hexagonally arranged sp^2 hybridized carbon atoms, held together by Van der Waals interactions. Ideally, the layers can be stacked in ABC or the more thermodynamically stable ABA configuration, but real graphite also presents defects that modify the ideal structure.[21, 22] Graphite presents a flake-like morphology with two kinds of surfaces, basal and edge plane, as seen in **Figure 4a.**[23] Upon lithium intercalation, the staking order of graphene layers changes to AAA, with lithium ions located in the center of the hexagon. Lithium intercalation in graphite happens gradually in a potential range of 0 to 0.25 V vs. Li|Li$^+$, following a staging mechanism. As shown in **Figure 4b**, it is possible to observe well-defined potential plateaus in which two staging phases, characterized by the incorporation of different lithium amounts, coexist. The volume change upon lithium intercalation is about 10%.[24] A limitation of graphite is its rate capability, which is limited by the risk of lithium plating.[25]

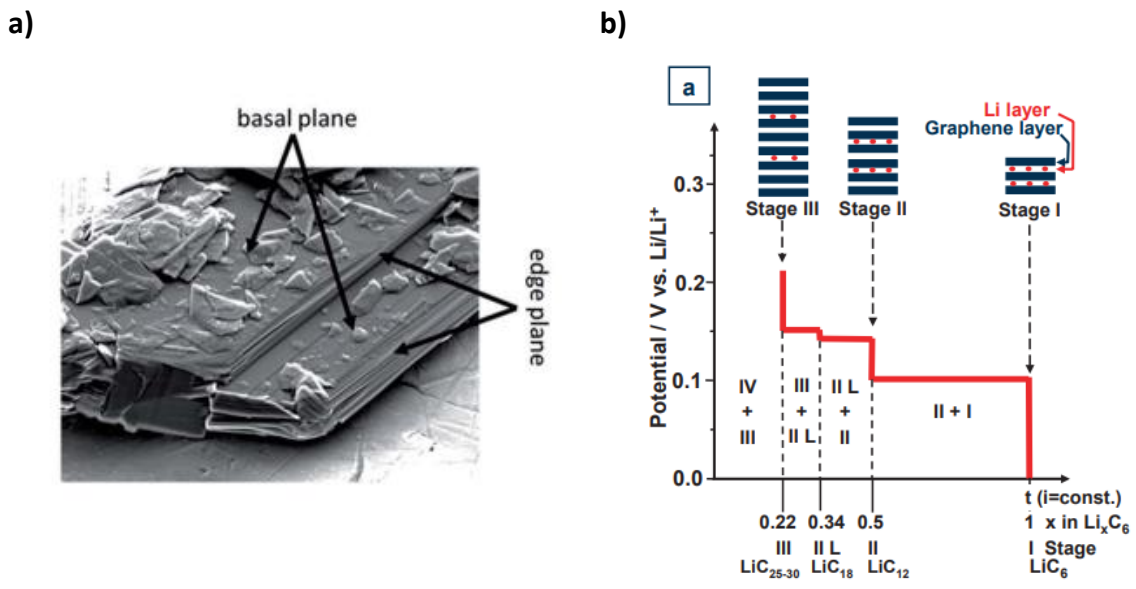

Figure 4: a) SEM micrograph indicating the basal and edge planes of graphite.[23] **b)** Stages of electrochemical intercalation of lithium into graphite.[20]

Because of the absence of lithium plating, the spinel LTO finds use in those applications where safety is of paramount importance. However, due to its high working potential (1.55 V vs. Li|Li$^+$)[26] and low specific capacity (175 mAh/g)[27], the attainable energy density is significantly reduced compared to graphite. Despite its 3D lithium transport pathway, it is not suitable for high-rate applications since the lithium diffusion coefficient and electronic conductivity are relatively poor.[28] Nevertheless, it allows for long and stable cycling thanks to the limited volume change upon lithiation of just 0.2%.[29]

Silicon is regarded as a promising anode material to obtain high-energy density LIBs. Its advantages can be traced back to the high content of lithium that can be accepted in its structure, leading to specific capacity as high as 3 579 mAh/g, together with its low voltage of 0.3 V vs. Li|Li$^+$ and abundance, compared to other alloying materials.[30,31] Upon charge at room temperature, silicon forms different amorphous alloy phases with increasing lithium content.[32] However, this comes with significant volume changes up to 300%, resulting in microcracking with consequent electrical contact loss and continuous SEI breakage and reformation (as depicted in **Figure 5**).[33] Therefore, to enable the practical application of silicon, modification strategies have to be implemented to face the extreme capacity fading and limited cycle life. A variety of nanosized structures able to accommodate the large volume variation such as nanoparticles, nanowires, and nanotubes, have demonstrated enhanced mechanical integrity and significantly improved electrochemical performance. [34–37] In terms of industrial feasibility, strong attention is focused on silicon oxide and silicon/graphite composites.[38,39] Moreover, to tackle the SEI instability, the use of suitable electrolyte additives is regarded a viable approach.[40,41]

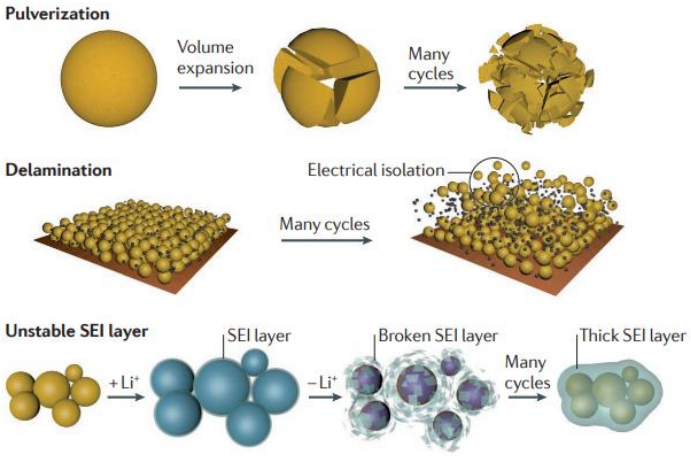

Figure 5: Main degradation mechanisms of Si electrodes originating from the large volume expansion of Si during lithiation.[13]

2.3 POSITIVE ELECTRODE

Several different materials have been studied as cathode active material in LIBs so far. The design of a suitable material for this purpose has to follow some ideal requirements regarding composition, structure, chemical and electrochemical properties, besides the always desirable environmental safety and low cost.[6, 17, 42]

Regarding the composition, it should contain a highly redox-active TM. It should react reversibly upon lithium intercalation and de-intercalation but also quickly and with a high free reaction energy. These last characteristics lead to high power performance, high voltage, and capacity. The structure should be stable and not undergo phase transitions during intercalation or deintercalation of lithium ions from the crystal structure. A good electronic conductivity of the material is advisable to minimize the need for additional conductive fillers, which decreases energy density, maximizes the electrochemically active area, and optimizes electron transfer.[42]

Different classes of active materials containing varying TM redox couples have already been synthesized and investigated. Up to this point, the most relevant cathode materials are $LiCoO_2$ (LCO), $LiNi_xMn_yCo_zO_2$ (NMC) and $LiNi_xCo_yAl_zO_2$ (NCA) (both with variable stoichiometries), $LiFePO_4$ (LFP) and $LiMn_2O_4$ (LMO). The specific capacities of the mentioned materials vs. their operational potential are compared in **Figure 6.**[6]

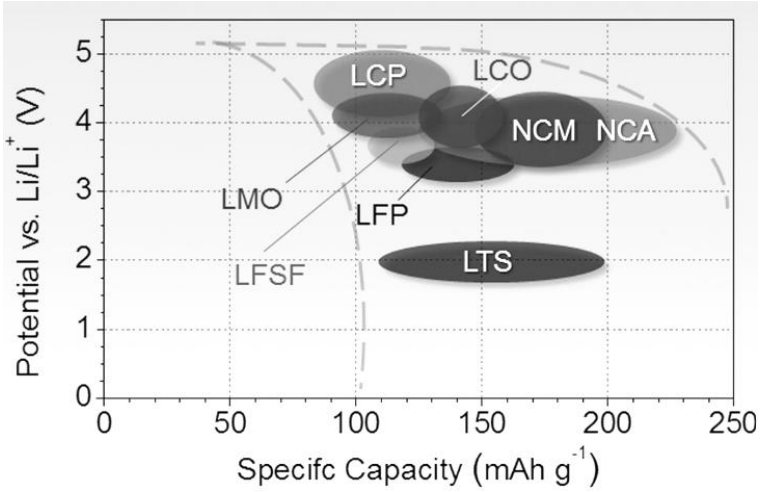

Figure 6: Comparison of main cathode materials classes in terms of potential and specific capacity. LCO stands for ''lithium cobalt oxide'', LMO for ''lithium manganese oxide'', NCM for ''nickel cobalt manganese oxide'', NCA for ''nickel cobalt aluminum oxide'' LFP for ''lithium iron phosphate''. Additionally to the materials discussed in the text, LCP stands for ''lithium cobalt phosphate'', LFSF for ''lithium iron fluorosulfate'', and LTS for ''lithium titanium sulfide''. (Adapted from [16])

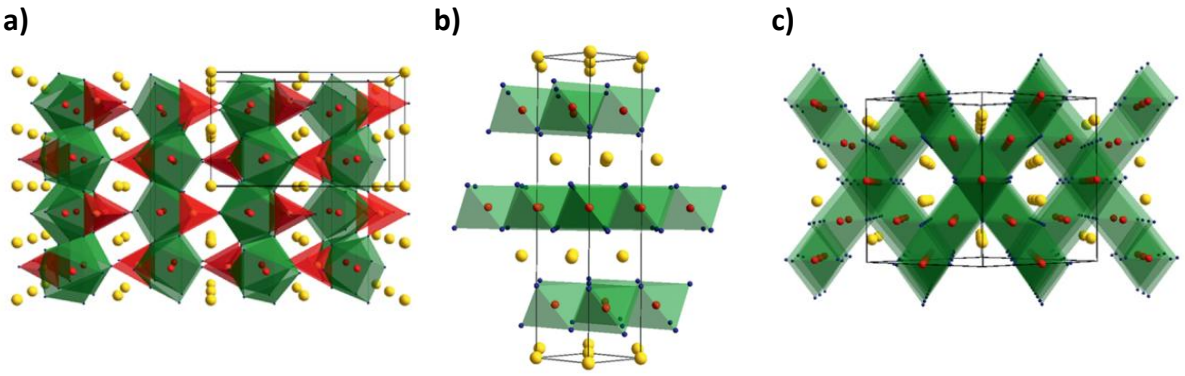

Figure 7: Crystal structure of the three main classes of materials applied as positive electrodes: **a)** 1D olivine **b)** 2D layered **c)** 3D spinel. In yellow are lithium ions, in blue oxygen and in red TM (or phosphorous in one-eight of the tetrahedral sites of olivine). [43]

The cathode active materials can also be classified in 1D, 2D or 3D based on their crystal structure, represented in **Figure 7**, and therefore dimensionality of the ion diffusion pathways

Many compositions of lithium TM phosphates with 1D olivine structures have been studied, differing in the included TM. These comprised iron, manganese, nickel, vanadium, and cobalt with LFP being the most successful formulation.[16, 44, 45] A drawback is its poor conductivity, but practical use is enabled by formation of small particles and addition of conducting phases, typically carbon.[46] For this reason, the volumetric energy enabled by this material is rather low, but thanks to its low price and high safety, in state-of-the-art LIB it is applied for heavy-duty uses or stationary applications.[6] Furthermore, LFP operating voltage is rater low, 3.45 V vs. $Li|Li^+$. To increase it and consequently improve energy density, despite its low capacity and crystalline density, a possibility is to substitute Fe with other metals.[45] Nevertheless, total substitution with nickel or cobalt to form $LiNiPO_4$ and $LiCoPO_4$ leads to very high potential materials that operate outside the voltage stability window of commercial organic electrolytes.[45],[47] $LiMnPO_4$ and $LiMn_{0.7}Fe_{0.3}PO_4$, obtained by substituting iron totally or partially with manganese lead to materials with electronic conductivities lower than LFP.[48]

Lithium layered TM oxides with 2D structure are a very promising class of cathode materials. $LiCoO_2$ was applied in the first commercial lithium battery system, its structure being similar to previously studied intercalation materials such as dichalcogenides.[17] Despite a high theoretical capacity (274 mAh/g assuming complete Li extraction), just 50% of the available lithium can be extracted due to structural and chemical instability. Moreover, rising costs of cobalt, its toxicity, and ethical issues regarding the extraction make the use of cobalt problematic.[49]

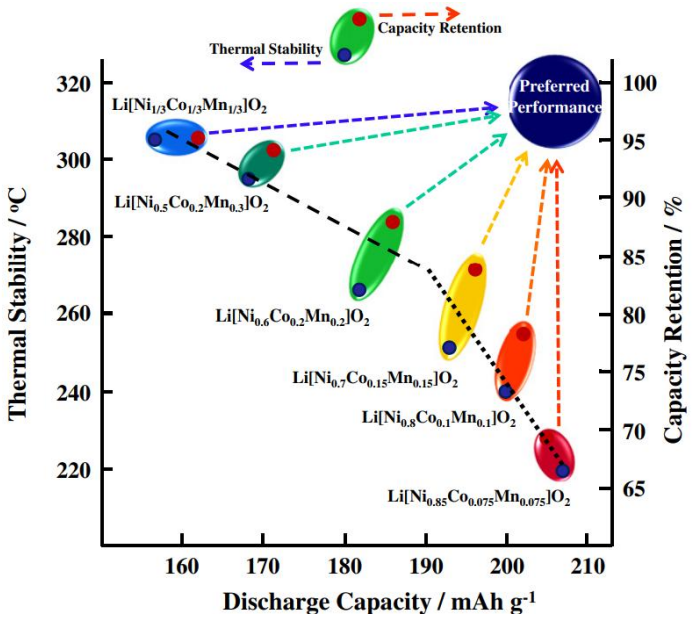

Figure 8: Plot of thermal stability, discharge capacity and capacity retention for different stochiometries of NMC. [50]

The isomorph stoichiometric $LiNiO_2$ is unstable due to lithium and nickel facile mixing[51], while partial substitution of cobalt with nickel allows to reversibly extract more lithium and thus increase practical capacity compared to LCO.[52] The introduction of electrochemically inactive Mn and Al allows to stabilize the structure, even if it comes at the expense of capacity.[53] Therefore, careful adjustment of the composition has led to the commercial success of NCM and NCA, with a good balance between energy density, stability, safety, and cost. NMC is usually reported in short with a number next to the initial of the transition metals, indicating their respective stoichiometric ratio, as exemplified for NMC111 ($LiNi_{0.33}Mn_{0.33}Co_{0.33}O_2$). NMC compounds with increasing nickel content are attracting interest due to reduced cobalt content and higher energy densities. However, shifting from NMC111 to Ni-rich materials impacts the safety, capacity and cycle life of the final cell, following the trend showed in **Figure 8.**[50]

The most relevant representative of transition metal oxides with 3D spinel structure is $LiMn_2O_4$ (LMO) and its partially Ni substituted version $LiNi_{0.5}\,Mn_{1.5}O_4$ (LNMO), characterized by a high operating voltage of 4.7 V and thus large theoretical capacity (>250 mAh/g), while LMO low theoretical capacity (148 mAh/g) is one of its limitations.[6, 54, 55] The spinel structure offers the advantages of safety and higher rate capability, arising from the chemically stable Mn^{3+}/Mn^{4+} couple and facile lithium mobility in the 3D framework, respectively.[17] Major drawbacks are the gradual capacity loss due to Jahn-Teller distortion of Mn^{3+}, Mn dissolution in the electrolyte and electrolyte decomposition on the surface.[56]

2.4 ELECTROLYTE

The electrolyte has the primary role of enabling lithium diffusion from one electrode to the other. It comprises a conducting salt dissolved in a mixture of solvents. Additives, in concentrations of lower than 10 wt.%, can also be added to the formulation to improve specific properties.[57]

Most commercially available LIBs employ organic solvents introduced to fulfill the requirement of a larger electrochemical stability window compared to aqueous electrolytes. Nonetheless, electrochemical stability towards the very low potential of lithium and lithiated graphite is realized in a kinetic (passivation through SEI) rather than thermodynamic way, in actual devices.[58]

As solvents, mix of multiple species are commercially adopted this is necessary to equilibrate the necessary properties that are not met by any component by itself. Most electrolytes contain ethylene carbonate (EC), which enabled the operation of LIB with a graphitic anode. In fact, the decomposition products of EC on the graphite surface protect it from exfoliation, which represented a limitation for batteries previously employing PC as solvent.[59] Moreover, the high polarity of EC is necessary for the dissociation of the conducting salt.[12]

However, since EC is solid at room temperature, it must be mixed with solvents with a lower melting point. Linear carbonates present low boiling points, low viscosity, and a low dielectric constant, and can form homogeneous mixtures with EC at any ratio.[12] Due to their effect of lowering the melting temperature and viscosity, linear carbonates are also crucial for good ionic transport. Therefore, they are commonly employed, even if their low flash point decreases the safety of the battery.[60] Examples of used co-solvents are EMC, used in this work, DMC and diethyl carbonate (DEC).

As conducting salt, lithium hexafluorophosphate ($LiPF_6$) is the choice for SOTA LIBs. This is due to a well-balanced combination of properties that are not met by any other conducting salt. In fact it has averagely good conductivity, result of the combination of its moderate values for dissociation constant and ionic mobility, thermal stability, anodic stability and chemical stability towards moisture. Nevertheless, it has some major drawbacks that limit its application and also render its preparation and purification challenging. Namely its sensitivity to trace amounts of water and high temperature. In solution, there is an equilibrium between

$LiPF_6$ and its dissociation products LiF and PF_5, favored at high temperatures. This can lead to further electrolyte decomposition due reactions as ring opening and ether links attack by PF_5, that is a strong lewis acid, and the formation of corrosive products such as HF and POF_3 by hydrolysis of the labile P-F bond.[12]

Chemical, thermal and electrochemical instability of the electrolyte, lead to its decomposition. This is connected to processes that contribute to performance deterioration. These phenomena comprise: parasitic reactions with charged active material, as well as HF formation due to moisture, connected to dissolution of active material. Inter-reactions of electrolyte components are also possible, as well as dissolution of the interphase and electrode cross-talk. Moreover, corrosion of current collectors may happen. Thermal effects connected to slow kinetics or accelerated degradation can furthermore lead to thermal runaway.[12]

Nowadays, the basic formulation of the electrolyte is industrially established, comprising the previously described components. Therefore, research on electrolyte additives is more widespread than research on completely new electrolytes since adding small amounts of a compound does not require any drastic change in the production.[12]

Many different additives have been tested and proved to enhance various aspects related to battery performance and safety. For better battery safety, there are additives that can lower electrolyte flammability, reacting with OH and H radicals to stop combustion, such as Tris(2,2,2-trifluoroethyl) phosphate.[61] Others can provide overcharge protection by acting as redox shuttles at potentials over the cathode cut-off, such as 2,5-di-tertbutyl-1,4-dimethoxybenzene.[62] In addition, it is possible to even terminate battery operation by forming insulating polymeric films in abuse conditions with additives in which polymerization gets activated at overcharge voltages.[63]

For better battery performance, there are additives able to improve interphase properties, reduce irreversible capacity and gas generation during SEI formation and long-term cycling, protect the cathode active material, and also improve physical properties of the electrolyte.[64]

Additives influencing SEI can be categorized as reductive type or as reactive type, based on their electrochemical stability. The latter, which are not reduced during battery operation, modify the SEI by various mechanisms. Examples of it are scavenging radical anions, thus

changing the relative amount of species in the SEI.[65] Others can be directly incorporated in the SEI, as Li_2CO_3.[66, 67] Others can operate through interaction with reduction products, as CO_2.[68, 69] Further possible mechanisms are to stabilize radical anion intermediates by aromatic compounds[70] or by adsorption on the electrode surface.[71]

In an ideal case, reductive additives are reduced at potentials higher than the reduction potential of the solvents and form an interphase with modified properties due to the deposition of their reduction products on the electrode surface.[72] Various derivatives of isocyanates[73], cyclic sulfites[74], and unsaturated molecules as vinylene carbonate[75] have been suggested to form polymer-like species on the negative electrode. Species such as thiophene and phenyl derivatives can also be oxidized at the positive electrode surface and form a protective interphase on the cathode.[76]

2.5 INTERPHASE

The term interphase indicates the passivation layer of decomposition products formed on the surface of electrodes. It is important to make a distinction from the term interface, which ideally indicates a 2D layer, that does not correctly describe the nature of the passivation layers that we find in battery devices.[77] The interphase at the anode side is indicated with the term SEI (Solid Electrolyte Interphase), while for the cathode side the terms CEI (Cathode Electrolyte Interface) or SPI (Solid Permeable Interface) have been coined.[78]

A layer of electrolyte reduction products with properties of a solid electrolyte was first observed on lithium metal after contact with the electrolyte.[79] It was later found that stable graphite cycling was allowed by insoluble reduction products from EC reduction deposited on the anode surface forming a similar layer.[80]

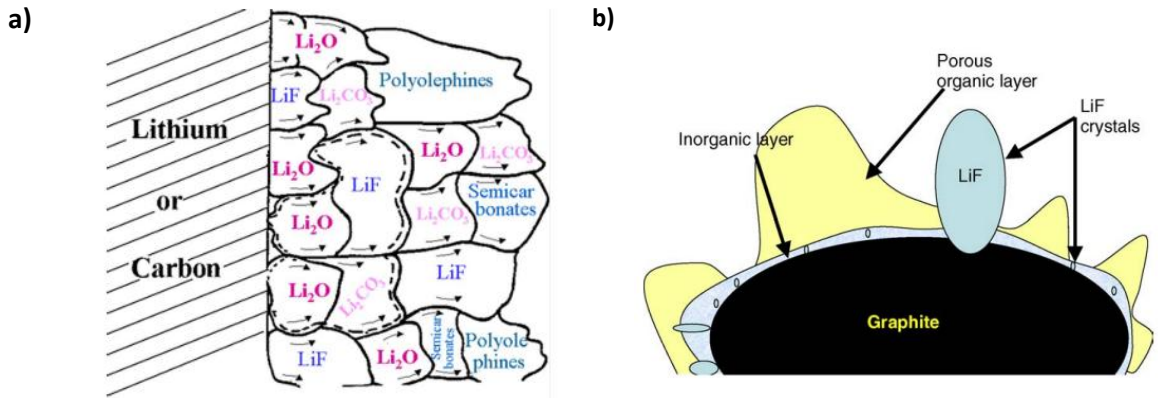

Figure 9: **a)** Mosaic model of the SEI.[84] **b)** Schematic structure of SEI.[78]

The SEI is a very important constituent of LIBs, since the employed organic electrolytes are not thermodynamically stable towards the low potential of lithiated graphite, because the lowest unoccupied molecular orbital (LUMO) of the solvent is lower than the Fermi level of the anode material. For this reason, the electrolyte solvents are reduced at the electrode´s surface during cycling. Therefore, the formation of an SEI is needed to enable long-term cycling by preventing electrolyte decomposition.

Ideally, the interphase is required to have some specific characteristics.First, electronic conductivity should be minimal, and Li^+ transport should be maximal. It should be uniform in morphology and composition, flexible to accommodate volume changes, but compact and well adhering to the electrode surface. It should also be formed from stable and insoluble components.[12] This is because the SEI composition and morphology and its evolution have an important role in battery performance. For example, one reason for capacity fading was found to be related to impedance growth following thick interphase formation. Also, self-discharge finds a correlation with continuous SEI growth.[81–83] Irreversible capacity loss in the first cycles was also found to be proportional to the electrode area and thus associated with SEI formation.[59]

For this reason, the SEI has been studied thoroughly, and various models have been elaborated to describe its structure, composition, formation mechanisms, and evolution. However, a complete description is still missing to this point.[85–87] At first, a 2D layer model was proposed to describe the SEI structure on lithium metal. Later, a two-layer model made of a more internal compact layer and an external porous one was proposed.[79, 88] The models proposed for lithium metal were also adopted for SEI on carbonaceous anodes, and moreover a 3D model where SEI products are partially intercalated in the graphite layers was introduced.[89] To explain why alkyl carbonate solvents with long alkyl chains cannot provide an efficient interphase, a supercapacitor model in which C=O negative charge anchors the reduction products to the surface was proposed.[90] In light of the experimental findings on SEI composition, the mosaic model, represented in **Figure 9a,** was elaborated and is nowadays largely adopted.[91] The structure emerging is a dual layer formed of organic and inorganic components. A more internal, compact SEI, mainly formed by inorganic components and an external, more porous SEI, mostly formed by organic components. The last is interpenetrated by the electrolyte, behaving like a gel, as schematically represented in **Figure 9b**. This

difference is also underlined by distinct diffusion behaviors of lithium throughout the interphase thickness, which have been proposed to be a kick-out mechanism in the inorganic layer, while in the outer inorganic layer lithium (and solvent) diffuse following the Fick's law.[92] The SEI thickness is inhomogeneous and ranges from 20 Å to several hundreds of Ångstrom and it's hard to measure directly due to mechanical damage during cell disassembly. In model systems, it has been calculated on average from its capacitance, obtained from EIS measurements.[93] It was also reported for studies on highly ordered pyrolytic graphite that the composition and thickness of SEI differ on the graphite edge and basal planes, with the basal plane being mostly covered by a thin layer of inorganic species and the edge plane, where lithium mostly intercalates, showing a thicker deposit with a prevalence of organic compounds.[94–96] The exact composition of SEI is influenced by different electrolyte compositions, different types of carbon/graphite, various cell formation processes, and environmental conditions as temperature. However, main component experimentally found in the SEI on graphite are $(CH_2OCO_2Li)_2$, $ROCO_2Li$, Li_2CO_3, ROLi, LiF, Li_2O, polycarbonates, LiOH, $Li_2C_2O_4$.[97]

To show how these products are formed, a first mechanism, shown in **Figure 10a,** was proposed for reduction on the lithium anode, in which coordination of Li^+ with the carbonyl group enables electronation of the carbonate molecules and nucleophilic attack between two radical anions, forming semicarbonate (also called alkyl carbonate) molecules, comprising lithium ethylene dicarbonate (LEDC), for EC, lithium methylene carbonate (LMC) and lithium ethylene carbonate (LEC) for EMC.[12] A more energetically reasonable ring opening mechanism, shown in **Figure 10b**, was later proposed based on the study of the intermediate products produced by photoionization and radiolysis. It was proposed that radical polymerization could form a 3D network of branched polymers.[98, 99] A further mechanism, shown in **Figure 10c**, involving acyl-oxygen cleavage, was proposed to explain CO formation from EC as demonstrated from analysis of gasses from isotope labelled molecules. This mechanism could coexist with the previous, that account for ethene gas formation.[100] The conducting salt also participates in the SEI formation. Chemical reduction of $LiPF_6$ has been shown to form LiF, for example.[101] Moreover, the complex composition can be explained by further products formed from aging and reaction with electrolyte components of the initially formed SEI components.[102]

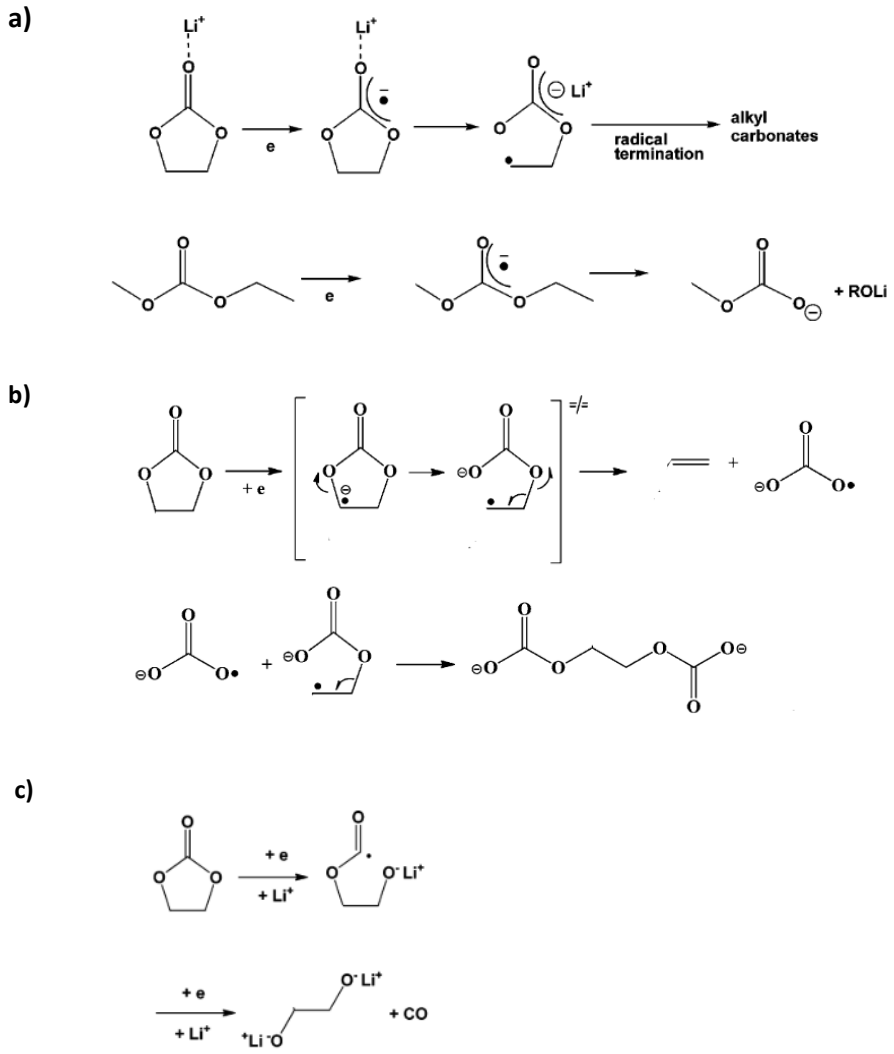

Figure 10: a) Reduction of EC and EMC to form semicarbonates.[12] **b)** EC reduction to $CO_3^{\cdot-}$ radical and ethene, and ring attack by the radical anion to form alkyl carbonates. [12] **c)** ring opening at the acyl oxygen. [57]

About CEI, it was initially less investigated; however, the interest in high voltage cathodes renders its understanding of crucial importance due to sustained electrolyte oxidation reactions and material degradation that can be mitigated through its modification.[103] Early x-ray photoelectron spectroscopy (XPS) studies showed a composition similar to SEI, with just relative organic content (lithium alkyl carbonates) and thickness varying depending on the material, while inorganic species comprising Li_2CO_3, LiF, and phosphorous oxides differed with the cathode material.[78] Products such as Li_2CO_3 can already be found on the cathode surface deriving from residual synthesis species, while LiF and $Li_xPF_yO_z$ are found as $LiPF_6$ decomposition products.[104, 105] Electrolytes can also be chemically oxidized by oxygen released from the cathode.[106] Cross-talk of SEI components can additionally contribute to CEI composition.[107, 108]

3 NMC CHALLENGES AT HIGH VOLTAGE

Batteries delivering high energy densities are required to fulfill the requirements of the EV market. Energy is defined as the product of capacity and average cell voltage, which are strictly related to the nature of electrode materials.[20] At the anode side, graphite is applied with an already large theoretical specific capacity, but silicon and silicon composite anodes could further enhance the anode capacity, and the implementation of lithium metal could give the maximum theoretical capacity with the lowest voltage.[23] Nevertheless, at the cathode side, energy is limited both from capacity and voltage. High-voltage spinel cathodes are promising candidates for next-generation batteries; however, electrolyte decomposition and the concurrent degradation reactions at electrode/electrolyte interfaces at such high voltage are critical barriers to their commercialization.[109] At present, NMC materials with stochiometric and moderate amounts of nickel (e.g. NMC111, NMC532, NMC622) have acceptable stability, safety and cost for application in commercial systems, but their capacity does not reach the requirements for next-generation EV.[110] Two strategies can be pursued to further increase the capacity of NMC electrodes: one is to increase the nickel content, resulting in enhanced specific capacity of the electrode, and the other is to raise the applied cut-off voltage, thus extracting more lithium ions from the crystal structure.[50, 111–114] As shown in **Figure 11**, NMC622 associated with cycling to voltages over 4.2 V reported the best results in terms of energy, but increased voltages also result in the degradation of the energy retained at higher cycle numbers.

Although stable cycling is observed for cut-off potentials up to 4.3 V for moderate nickel content materials as NMC532 and NMC622, with cycling up to 4.5 V or higher, the degradation mechanisms observed for NMC materials appear to be more pronounced and contribute to a faster capacity fading.[115]

Multiple interconnected degradation mechanisms discussed in the following take part in the capacity fading of cells containing (high voltage) NMC electrodes.

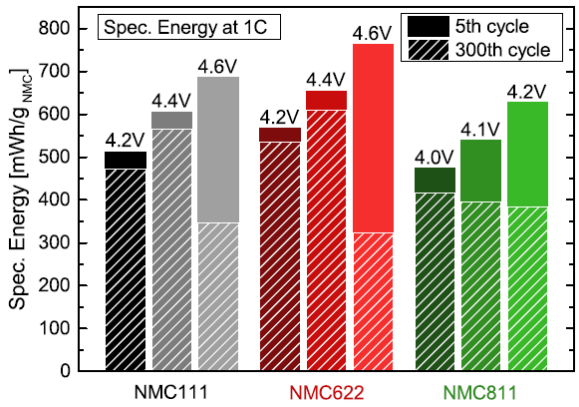

Figure 11: Specific energy of NMC111||graphite, NMC622||graphite and NMC811||graphite cells in 1 M $LiPF_6$ in EC:EMC (3:7 v/v). The full columns represent the specific energy of the 5th cycle (1 C-rate), the dashed part of the columns of the 300th cycle (1 C-rate). [116]

Cation mixing due to the similar ionic radius of Ni^{2+} and Li^{+} causes the loss of active lithium sites. In fact, a high degree of delithiation leads to the formation of a very unstable crystal structure due to extended depletion of the lithium layers, and the severe cation mixing allows to stabilize the structure and prevent its collapse. With increasing disorder, reconstruction of the surface crystal structure is observed: the formation of lithium vacancies in the surface layers promotes phase transformations from rhombohedral to a disordered spinel phase and even NiO rock salt phase, starting from the surface and penetrating for tens of nanometers into the particle structure.[117] This results in increased resistance due to reduced lithium ion mobility in these structures.[118]

The structural change is also accompanied by oxygen release, with consequent electrolyte oxidation, swelling of the cell due to the gas and risk of explosion and fire. Oxygen release has been observed to correlate with the formation of CO and CO_2, explained by the oxidation of ethylene carbonate from reactive (singlet) oxygen, which is found to originate from the structural changes occurring on NMC surface.[116] Oxygen and CO_2 are in addition originating from Li_2CO_3 surface impurities by chemical or electrochemical reduction. These impurities result from synthesis residues, mainly Li_2O that slowly convert to LiOH and Li_2CO_3 under reaction with H_2O and O_2 in the atmosphere.[119]

Moreover, dissolved transition metals have been detected in the electrolyte when NMC is highly delithiated;[120] however, the dissolution mechanism is still not clear.[121] One main proposed mechanism is the disproportionation of manganese +3 in presence of hydrofluoric acid, formed by $LiPF_6$ hydrolysis, leading to soluble Mn^{2+}. Manganese(III) is not present in NMC but is proposed that it could be formed in the surface layers in presence of oxygen defects and

due to a weaker M-O bond at high potentials.[122] Other proposed mechanisms are the mechanical detachment of active material due to particle cracking and metal solvation by PF_6 anion or migration of metals in the oxygen layers due to low concentration of oxygen vacancies arising from synthesis, or Mn^{3+} formed on the spinel crystal structure arising on the surface.[123] Most importantly, the presence of transition metals at the negative electrode side has been correlated to the impedance rise of the anode and cell failure due to lithium dendrite formation.[113, 124] Due to the low potential of graphite, metallic manganese was proposed to be formed via reduction at the anode surface, causing an increased electrolyte decomposition.[124] However, Zhan *et al.* reported that the oxidation state of manganese deposited on the surface is 2+ and postulated that Mn^{2+} accumulates in the SEI by an ion-exchange reaction with Li^+, thus blocking lithium ion diffusion. This was further confirmed by Gilbert *et al.,* also underlying the loss of active lithium by lithium trapping in the SEI.[125,126]

Furthermore, contributing to NMC capacity fading is the cracking of primary particles, resulting in active material loss due to contact failure. Again, this is connected to structural changes since the anisotropic increase in lattice parameters due to the repulsion of the oxygen layers at highly delithiated states leads to repeated expansion and contraction over cycling, which can be regarded as the origin of particle cracking.[127]

To mitigate the capacity fading of NMC materials, several strategies have been investigated: First, single crystal NMC exhibited reduced degradation and is thus considered more appropriate for high voltage applications.[128, 129] Increased structural stability was obtained by core-shell and gradient concentration structures with manganese-enriched outer layer.[130] In addition, multiple elements have been introduced as dopants. For example cation doping with Mg^{2+} or Ca^+ have proven to reduce cation mixing.[131, 132] Various kinds of surface coating proved to be beneficial; for instance, at high voltage, improved capacity retention was obtained with $FePO_4$ coating, preventing electrolyte reaction.[133] Moreover, carbon matrices proved to enhance structural stability.[134] Furthermore, several film-forming additives, such as tripropargyl phosphate, can stabilize the interphase and inhibit gas generation.[135]

4 ETHYLENE CARBONATE DERIVATIVE ADDITIVES

There is a wide variety of electrolyte additives, some of which improve battery performance by modifying interphases, SEI or CEI alike. Currently, the two most commonly used additives are vinylene carbonate (VC) and fluoroethylene carbonate (FEC). Their structure is similar to EC but they have been reported to be reduced at a higher potential, compared to EC, and passivate negative electrodes surface. The formed decomposition products generally influence positively discharge capacity, capacity retention, self-discharge and gassing. However, there is no agreement on how exactly the products deposited at the interphase lead to the modified performance.

VC has been extensively studied: Aurbach *et al*. first investigated the effect of VC on graphite, LNO and LMO electrodes. They reported reduced irreversible capacity and increased stability during prolonged cycling at high temperatures (60°C) for graphite, improved kinetics for cathode materials, and reduced impedance, also at room temperature, for both. Based on additional XPS and Fourier-transform infra red (FTIR) signatures found on both electrode surfaces in the presence of VC, they attributed this impact to the ability of VC to form polymeric and oligomeric species and reduce the formation of more resistive LiF and Li_2CO_3.[136] Ota *et al.* additionally studied the composition of the formed SEI on graphite by means of nuclear magnetic resonance (NMR) and time-of-flight secondary ion mass spectroscopy. Moreover, they studied the composition of evolved gasses, finding suppression of ethylene, carbon monoxide and methane formation, typically coming from solvent decomposition, and additional formation of carbon dioxide and acetylene when VC was added. Acetylene is proposed to result from the reductive decomposition of VC to form lithium vinylene dicarbonate $(CHOCO_2Li)_2$ (LVD). Moreover, acetylene could further polymerize to polyacetylene. CO instead would result from divinylene dialkoxide $(CH=CHOLi)_2$ formation, while CO_2 results from VC decarboxylation, leading to the formation of lithium carboxylate (RCOOLi). Furthermore, they affirmed that lithium divinylene dicarbonate $(CH=CHOCO_2Li)_2$ (LDVD) was formed on the graphite surface. Based on NMR results, the structures shown in **Figure 12** were proposed for VC decomposition products, respectively compound 1 is

poly(VC), compound 2 is a polymeric carbonate resulting from VC ring opening and compound 3 is a VC oligomer.[75] Wang *et al*., based on density functional theory (DFT) calculations, proposed that VC is initially reduced to a more stable intermediate than EC, which can then decompose to form a radical anion. The radical then undergoes a series of reactions leading to products such as LDVD, LiC (lithium carbide), LVD, and ROLi. These compounds differ from EC reduction products because they contain double bonds that can undergo further polymerization. Moreover, if the radical anion attacks the double bond of VC or the carbon anion nucleophilicly attacks the carbonyl carbon of VC, low-order oligomers with repeated vinylene and carbonate-vinylene units can respectively be formed, as shown in **Figure 12b**. They also reported that otherwise, the ring opening can occur on the unreduced EC moiety, via an intramolecular electron transfer transition state, in which VC just helps the intermediate formation and is not consumed.[137] El Ouatani *et al.* found that poly(VC) obtained from VC radical polymerization is the major observed product on both electrodes, by a combined analysis and simulation of the XPS core and valence spectra of the interphase on $LiCoO_2$ and graphite surface, at different potentials during the first charge.[138] In an attempt to further clarify SEI composition Michan *et al.* and Grugeon *et al.* synthesized the products of VC reduction by different routes.[139,140] From NMR, XPS, gas chromatoghraphy-mass spectrometry (GC-MS) and FTIR results, they first identified poly(VC), Li_2CO_3, lithium oxalate and lithium formate ($Li_2C_2O_4$, and HCO_2Li), but no LVD and LDVD. Also, they did not observe CO_2 as evolved gas but ascribed it to an excess reducing agent that would consume all of it to form $Li_2C_2O_4$, Li_2CO_3 and HCO_2Li. The second additionally found LDVD and polyacetylene to be formed, and proposed different routes that the additive may follow in more (i.e. direct contact with the electrode surface) or less reducing conditions, reported in **Figure 12c**. Wang *et al.* in a comparative study of VC and FEC in LCO||graphite pouch cells, indicated a VC concentration between 2 and 4 wt.% as optimum since it provided high Coulombic efficiency (CE) low self-discharge, small increase in charge-discharge polarization, as well as acceptable charge transfer impedance. Most beneficial effects were obtained for FEC in high concentrations, up to 6 wt.%, except for large gas generation under long term cycling, at 40°C.[141]

FEC was first applied as an additive for $LiCoO_2$||graphite cell systems by Mcmillan *et al*. after their studies on ClEC.[142] It was then studied in multiple cell chemistries, demonstrating improved capacity retention by formation of protective films both on anode and cathode

materials.[143–150] Concerning its effect on graphite, Profatilova *et al.* reported an increased LiF content and reduced impedance on graphite anodes.[151]

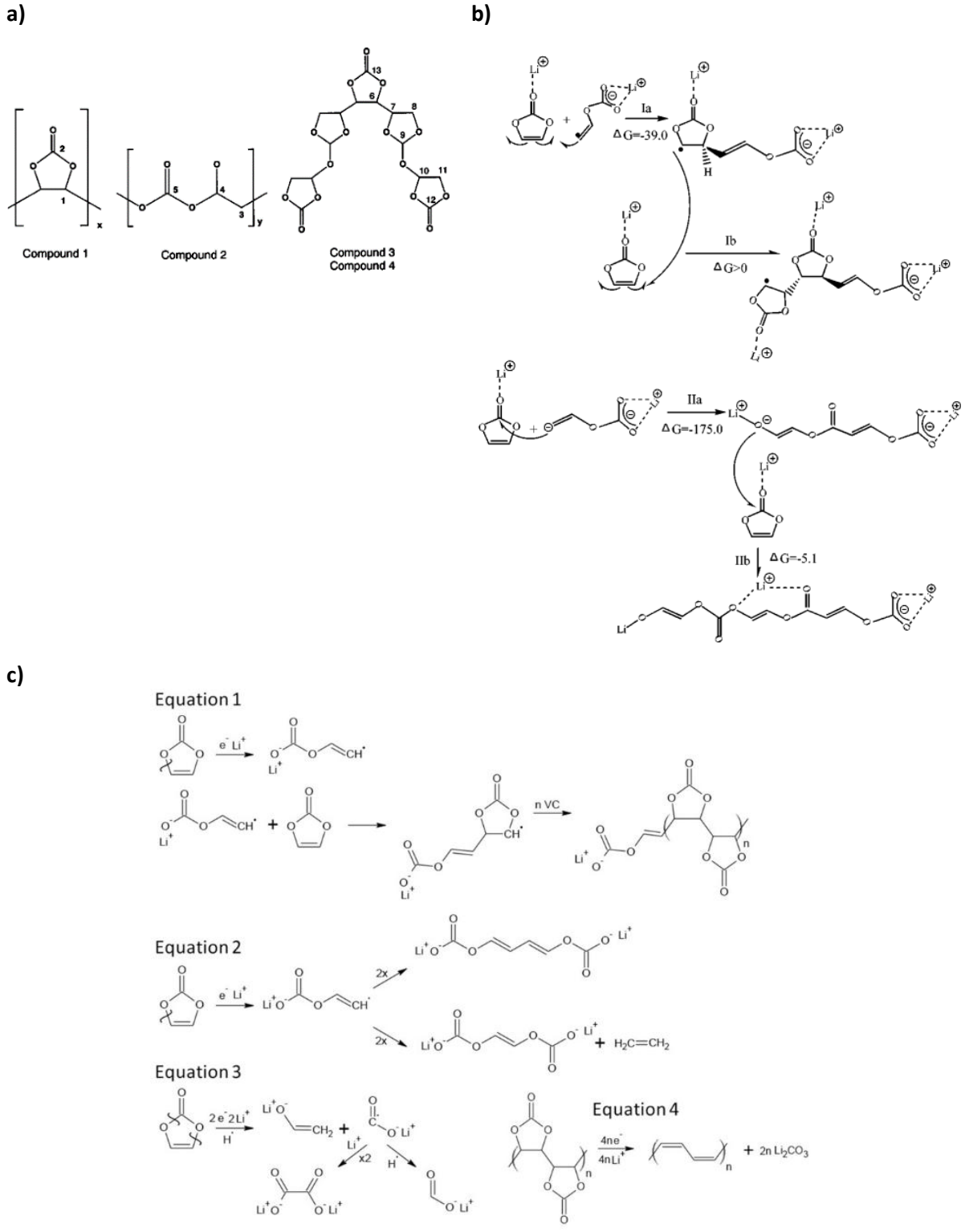

Figure 12: a) Structures of VC decomposition products deduced from NMR.[75] **b)** Calculated pathway for oligomer formation from VC.[137] **c)** Proposed VC reduction pathways based on synthesis of reduction products.[140]

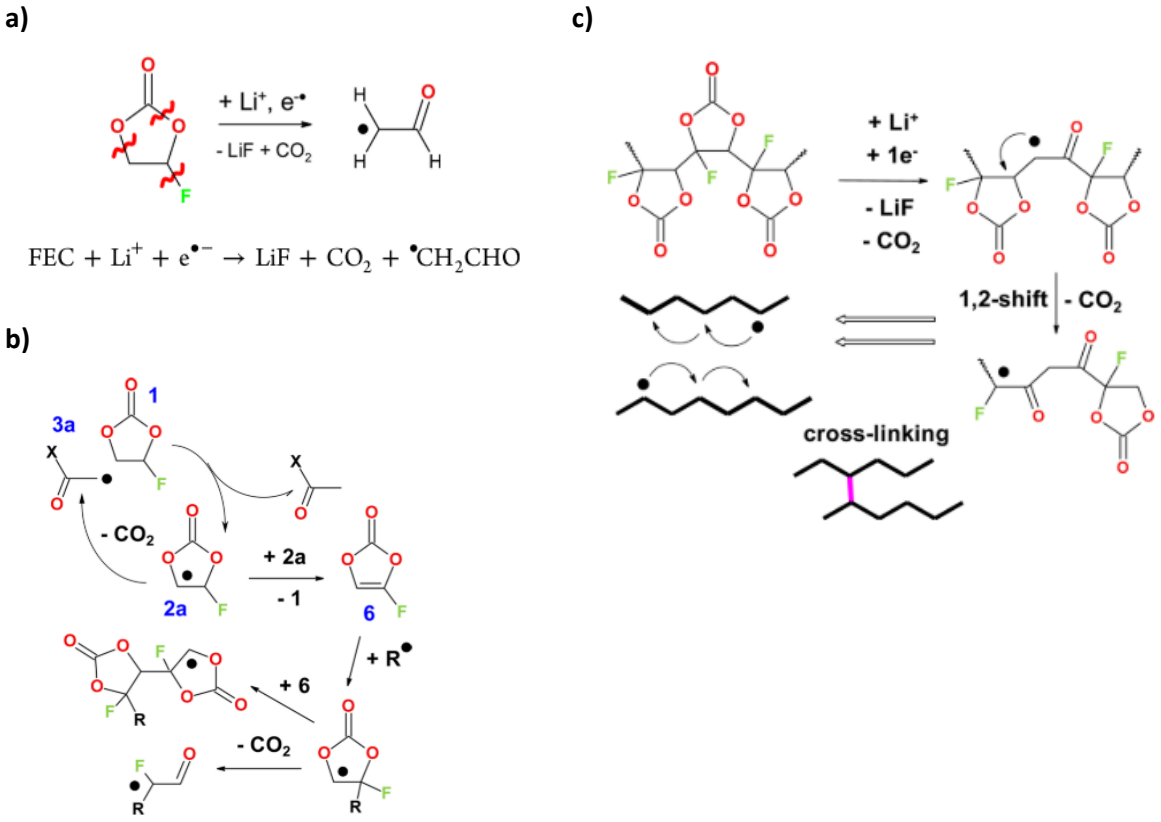

Figure 13: a) Ring opening of FEC. **b)** Polymerization of FEC to poly(FEC) **c)** Cross-linking mechanism of poly(FEC). (Adapted from [152])

Zhao *et al.* reported a reduced quantity of lithium alkyl carbonates in the SEI, attributed to suppression of EC decomposition. Moreover they reported LiF formation, to which it was attributed the increase of SEI resistance and rigidity, leading to its breakage and consequent capacity loss with high FEC content . Moreover, they proposed radical polymerization of double-bond-containing lithiated alkyl carbonates as reaction pathway for formation of polymeric species, starting from reduced VC formed from FEC defluorination. [153] Shkrob *et al.* experimentally investigated the redox chemistry of FEC by means of radiolysis, laser photoionization, electron paramagnetic resonance, and transient absorption spectroscopy. They concluded that FEC follows the ring opening pathways in **Figure 13a**. Living polymerization can be initiated by radical 3a (**Figure 13b**) leading to a ring containing polymer. Therefore, they ascribed FECs´ superior performance to its ability to form highly crosslinked polymer networks when poly(FEC) is reduced, as shown in **Figure 13c**.[152]. However, in contrast with these results, Okuno *et al.* deduced from DFT calculations, that defluorination is the main reaction taking place due to a lower activation barrier.[154] Moreover, synthesis of FEC reduction products by Michan *et al*. showed the presence of a VC intermediate rather than intermediates leading to poly(FEC) formation.[139] Nie *et al.* experimentally studied the

composition of SEI after formation on binder free graphite in a half cell containing standard electrolyte plus 3 wt.% FEC. Comparing it with SEI formed in absence of FEC, a lower concentration of lithium alkyl carbonates and similar LiF concentration was found, indicating a diminished $LiPF_6$ reduction. Additionally, Li_2CO_3 and a polymeric species (assigned as poly(FEC)) were observed. The SEI was also thinner (10–20 nm), but with a grainier structure, ascribed to the higher content of inorganic species.[155] A study in LCO||graphite pouch cells charged to 4.4 V by Liu *et al.* reported that in the presence of 5% FEC, an SEI is formed both on cathode and anode, with the cathode film containing more fluorine in organic species, suggesting a preferential ring opening mechanism at high voltage, while defluorination appears to be favored at the anode.[156]

Vinyl ethylene carbonate (VEC) was first studied by Hu *et al.* as additive, showing that a 5 vol% concentration suppresses graphite exfoliation and allows cycling in PC, in a Li-metal|graphite cell. They measured graphite surface *ex-situ* after one charge to 0.1 V vs. $Li|Li^+$ with FTIR and found peaks that were assigned to $ROCO_2Li$, Li_2CO_3, and ROLi. XPS revealed binding energies correspondent to C–C, C–O, C=O and OCO_2 groups, in accordance with IR results. Upon sputtering, a peak corresponding to C-Li bond appeared too. Butadiene was detected as formed gas. They also performed DFT calculations of reduction pathways, revealing a series of possible reactions, reported in **Figure 14**.[157] Chen *et al.* performed a study of the anodic oxidation of VEC on gold, with analysis of reaction products by ATR-FTIR and gel permeation chromatography (GPC), showing the presence of high molecular weight polymers formed at 3.6 V, specifically polycarbonates consisting of EC-like and VC-like carbonate rings linked by aliphatic methylene and methyl branches, initiated by the proposed allyl radicals reported in **Figure 15a**.[158]

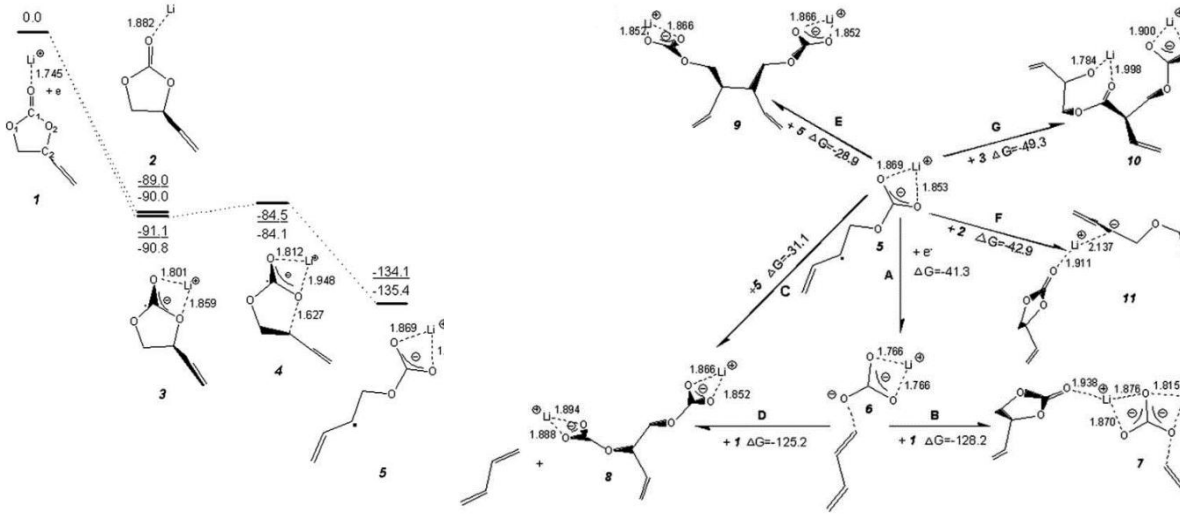

Figure 14: VEC reduction pathways calculated by DFT. [157]

Tsubouchi *et al*. analysed surface films formed on highly oriented pyrolytic graphite edge plane electrodes in 1 M $LiClO_4$, EC/DEC after potential sweep to 0.1 V vs. $Li|Li^+$ by ATR-FTIR and XPS. VEC-derived surface films were found to be composed of lithium alkyl carbonates and contained a relatively large amount of Li_2CO_3, compared to the one obtained in standard electrolyte. This was explained by considering the reactivity of the intermediate radical compound formed from ring-opening by one-electron reduction, as shown in **Figure 15b**. For VEC the intermediate (1) is not strongly stabilized by resonance structures involving just the allyl group. As a result, Li_2CO_3 should preferentially be formed through further one-electron reduction reactions, rather than $LiOCO_2R$ from radical recombination.[159] S. Xu *et al.* further characterized SEI formed by VEC added at different concentrations (0.5, 1, 3, 5, 10 vol%) in Li-metal|graphite cell. They found improved discharge capacity for VEC content of 1 vol% and attributed it to a balanced suppression of EC reduction, observed by intensity changes of CV peaks. ATR-FTIR showed two additional peaks at around 1802 and 1769 cm^{-1} when VEC was used, which they assigned to be related to polycarbonate formed by some polymerization of VEC.[160] Petibon *et al*. investigated VEC effect on performance in full pouch cells ($LiCoO_2$||graphite) charged to 4.2 V for concentrations of 0.5, 1, 2, 5, 6 wt.%. They reported that VEC cannot passivate the graphite surface, based on dQ/dV and GC-MS results. The observed increase with VEC content of the reduction peak corresponding to EC reduction suggested that VEC reduction products may as well be further reduced at this potential. No apparent beneficial effect on discharge capacity, Coulombic efficiency and charge end-point slippage resulted from the addition of VEC at any concentration.

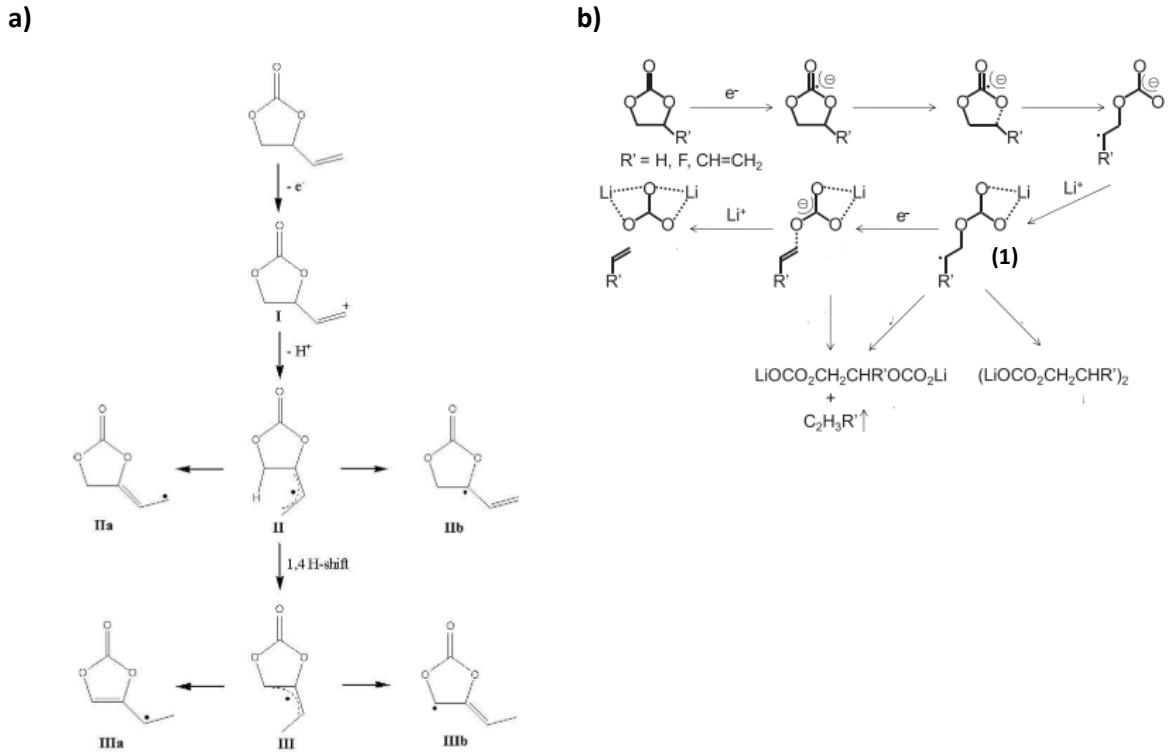

Figure 15: **a)** Proposed radical initiators for VEC polymerization formed by anodic oxidation.[158] **b)** Ring opening and further possible reaction pathways of VEC (R': CH=CH2) (Adapted from [159])

Polarization reduction was the only reported benefit; however, large gas formation upon cycling was observed as a major drawback. The impedance of the negative electrode appeared not influenced by VEC presence leading to the conclusion, in contrast with previous studies in half cells, that no VEC reduction product is deposited on graphite surface. Positive electrode impedance increased for concentrations over 4% was correlated to the deposition of products of further reduction, indicated by the additional current observed in dQ/dV.[161, 162] Zuo *et al.* instead reported improved performance for NMC442||graphite cells charged to 4.5 V when 2 wt.% VEC was added, ascribing it to the formation of an effective interface on both anode and cathode.[163] Forestier *et al*. reported that VEC is solvating lithium ions and thus is transported across the Li_2CO_3 inhomogeneous SEI under the effect of an electric field.[164]

Chloroethylene carbonate (ClEC) has been just briefly studied in the past. Shu *et al*.[165, 166] reported the ability of ClEC to passivate the graphite surface and optimally reduce first cycle capacity loss in PC based electrolyte for a volume fraction of 0.3. Used as additive (5 vol%) in a PC/EC electrolyte it allowed long cycle life in a $LiCoO_2$||graphite full-cell, with 20% capacity loss after 800 cycles. However, low Coulombic efficiency and extra irreversible capacity were observed, ascribed to LiCl solubility and thus chemical shuttle effect. Winter *et al.* additionally reported CO_2 formation and consumption in *operando* in a similar electrolyte system.[167, 168]

5 *OPERANDO* SHINERS

3.5 RAMAN

Raman spectroscopy is a powerful technique based on the inelastic scattering of light. It allows the investigation of Raman's active vibrational energy levels of molecules. In non-resonant Raman the employed wavelengths are in the IR-visible range, so that electronic transitions are not involved.

Linear and non-linear molecules have respectively $3n-5$ and $3n-6$ independent vibrational modes, arising from the $3n$ internal degrees of freedom of a molecule, with n number of atoms of the molecule, subtracting rotations and translations. Each vibration mode can be described in first approximation from a harmonic oscillator of frequency $\nu_{vib} = \frac{1}{2\pi}\sqrt{\frac{K}{\mu}}$ where K is the force constant, which is function of the bond energy, and μ is the reduced mass, given by $\frac{1}{m_1}+\frac{1}{m_2}$ with m_1 and m_2 masses of the atoms. The potential energy associated to the harmonic oscillator is $U = \frac{1}{2}KX^2$ where X is the internuclear distance. Since molecules can just be in quantized energy states, vibrational energy levels are quantized, with energy $E_{vib} = \left(v_i + \frac{1}{2}\right)\nu_{vib}\, h$, where v is an integer quantum number and h is the Planck constant. The occupation of these energy levels follows a Boltzmann distribution. The fundamental state has energy $E_{vib} = \frac{1}{2}\nu_{vib}\, h$.

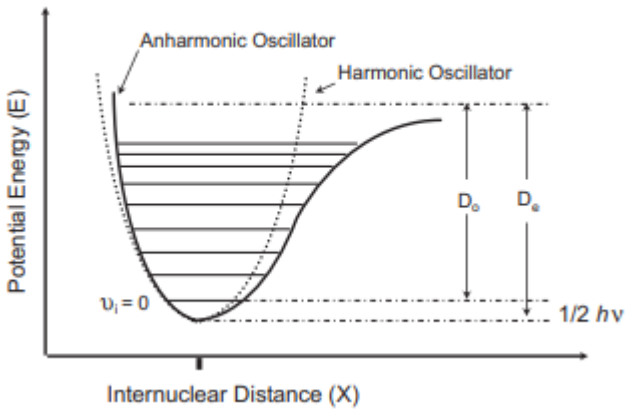

Figure 16: The potential energy diagram comparison of anharmonic and harmonic oscillator.[169]

Molecules in higher energy levels still have the same vibrational energy but will differ in the probability of finding the electron cloud more displaced from the equilibrium position.

While the harmonic oscillator is a good approximation when the dipole moment is linearly proportional to the displacement, more often, a correction is necessary to explain phenomena as unevenly separation of energy levels, combination of vibrational modes and overtones. The anharmonic potential is called Morse potential, and the arising energy levels are

$$\mathrm{E_{vib}} = \left(\mathrm{v_i} + \frac{1}{2}\right)\mathrm{v_{vib}\,h} - \left(\mathrm{v_i} + \frac{1}{2}\right)^2 \mathrm{v_{vib}\,h}\,\chi.$$

For a vibrational mode to be Raman active, it has to lead to a variation of the polarizability α. Polarizability depends on the molecular structure, the mass of the atoms, and the strength of the bond, so it is a function of the instantaneous position of atoms, that changes when perturbated from an electromagnetic field E.

The perturbation is expressed as $\mathrm{dQ} = \mathrm{Q_0}\,\cos(2\pi \mathrm{v_{vib}} t)$, where $\mathrm{v_{vib}}$ is the frequency of the vibrational mode involved and $\mathrm{Q_0}$ is the maximum displacement (<10% of the bond length).

Polarizability can be expressed as $\alpha = \alpha_0 + \left(\frac{\mathrm{d}\alpha}{\mathrm{dQ}}\right)_0 \mathrm{dQ}$, in which the term $\left(\frac{\mathrm{d}\alpha}{\mathrm{dQ}}\right)_0$ is the first order term of the induced dipole moment P, indicating the variation of α around the equilibrium position.

The term inelastic scattering stems from the fact that light is not absorbed, as in the complementary IR spectroscopy, but instead, an incident photon perturbates the system leading to the emission of another photon with different energy. Part of the radiation is also absorbed, leading to the undesired fluorescence effect.

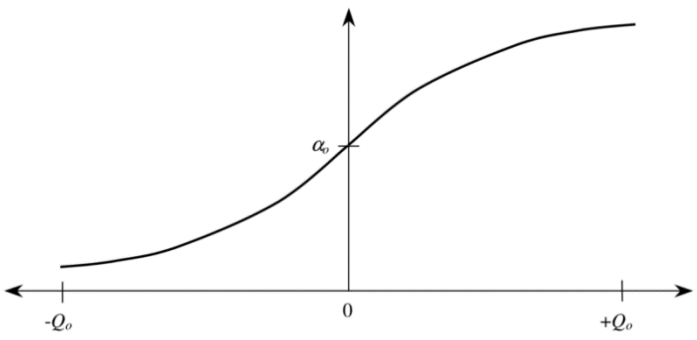

Figure 17: Example of a dipole moment varying around a_0.[169]

To understand where the frequency of the emitted photon arises from, it is necessary to look at the induced dipole moment $P = \alpha E$. In fact, when electromagnetic radiation hits a molecule, it causes an oscillation, at the same frequency ν_0 of the incident field, of the electronic cloud of the involved atoms. This leads to a charge separation, namely an induced dipole.

The Taylor series expansion of the moment associated to the induced dipole is

$$P = \alpha_0 E_0 \cos(2\pi\nu_0 t) + \left(\frac{d\alpha}{dQ}\right)_0 dQ\, E \{\cos[2\pi(\nu_0 - \nu_{vib})t] + \cos[2\pi(\nu_0 + \nu_{vib})t]\}$$

The first term represents the elastic scattering, also called Rayleigh scattering, while the second term represents the two components of the first order inelastic scattering, which arise just if $\left(\frac{d\alpha}{dQ}\right)_0$, the polarizability variation, is not zero, explaining the selection rule for Raman.

As shown by the cosine arguments, the photons resulting from inelastic scattering have frequency $\nu_0 - \nu_{vib}$ and $\nu_0 + \nu_{vib}$, so that the spectra are commonly plotted as $\Delta\bar{\nu}$, defined as Raman shift, in cm^{-1} unit, given by $\frac{\nu}{c}$, c being light speed. The component with negative Raman shift is called Anti-Stokes, while the one with positive Raman shift is called Stokes. It generally has higher intensities and thus is commonly the observed one.

The two limitations of Raman spectroscopy are the low intensity of the Raman signal, since most of the light is scattered elastically, and fluorescence intereference.

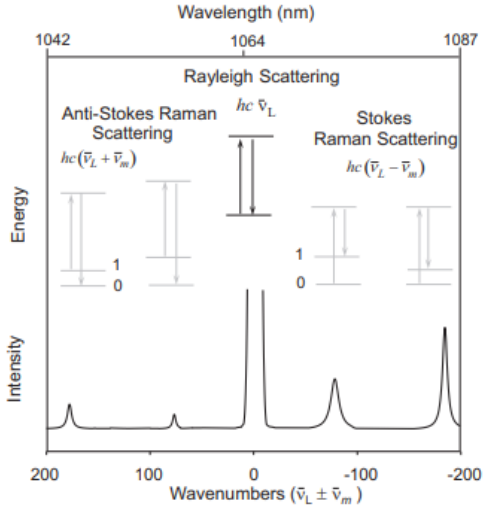

Figure 18: Schematic illustration of Rayleigh scattering as well as Stokes and anti-Stokes Raman scattering. The laser excitation frequency (n_L) is represented by the upward arrows and is much higher in energy than the molecular vibrations. The frequency of the scattered photon (downward arrows) is unchanged in Rayleigh scattering but is of either lower or higher frequency in Raman scattering.[169]

Practically, there are some approaches to tackle these drawbacks. First, the light source employed needs to have a high intensity, but also to be collimated to allow high resolution, and be monochromatic in order to fix the energy of the virtual state. Lasers are used for this purpose. Higher wavelengths lead to lower fluorescence probability, higher Raman shifts but lower cross-section and thus intensity, since cross-section is proportional to the fourth power of the Raman shift.

Confocal Raman systems, employ a microscope to focus the light on the sample and to collect the emitted radiation. This allows to have a very intense laser excitation in a restricted area, resulting in an increase in the signal intensity, and also to have a higher spatial resolution.

A possibility to enhance the Raman signal is also given by measurement close to nanostructured metallic materials in conditions of localized surface plasmon resonance (LSPR), that provide a signal enhancement.

5.1.1. ENHANCED RAMAN SPECTROSCOPIES

Surface Enhanced Raman Spectroscopy (SERS) effect was first observed in 1974 by Fleischmann *et al.*, that collected the Raman spectra of Pyridine absorbed on a roughened silver electrode.[170]

The observed enhancement is two-folded, both electromagnetic and chemical. The electromagnetic enhancement, in the order of 10^8, originates from the field amplification of both the incident and emitted field in the proximity on nanometallic structures in plasmon resonance conditions. The chemical enhancement, in the order of 10^2 , originates from the increased cross-section for an adsorbed molecule compared to a free one.[171]

The LSPR at the origin of electromagnetic enhancement can be explained in the quasi-static (dipolar) approximation for spherical particles of size lower than light wavelength, and is reasonably good for spherical particles up to 100 nm. In this case the results of the Mie theory, necessary to correctly describe the field response in bigger nanoparticles where the field phase changes over the volume, are leading to the same results as the quasi-static approximation.

From the calculation of the internal and external field the polarizability

$\alpha\,(\omega) = 4\pi a^3\,\frac{\varepsilon\,(\omega) - \varepsilon_m}{\varepsilon\,(\omega) + 2\varepsilon_m}$ is obtained, where ε_m is the dielectric constant of the surrounding medium. This is at maximum when the denominator $|\varepsilon(\omega) + 2\varepsilon_m|$is at minimum.

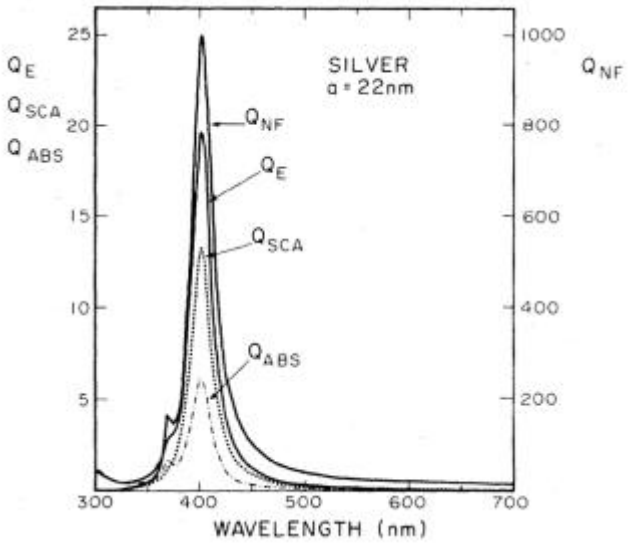

Figure 19: Scattering, absorption, extinction, and local field efficiencies (Q_{sca}, Q_{ABS}, Q_e, Q_{NF}, respectively) for a silver nanoparticle with radius a = 22 nm immersed in water. These quantities are proportional to the corresponding cross-sections ($Q = \sigma/\pi a^2$). [172]

This is known as the Fröhlich condition and it is met by metals as gold, silver, aluminum and copper: in fact, their real dielectric constant is negative for $\omega < \omega_p$, always true in visible frequencies, and moreover they have a low value of the imaginary one, leading to a high enhancement. When the Fröhlich condition is met it leads to an enhanced electromagnetic field both inside and outside the nanoparticle, but also to the maximum absorption and scattering cross-section of the nanoparticle itself. This allows to choose a suitable wavelength depending on the enhancing substrate, since the ones giving maximum absorption will also give maximum enhancement.

Different kinds of Enhanced Raman Spectroscopy have been developed using different nanometric metallic structures. SERS has been exploited with many different substrates, including self-assembled nanoparticle arrays. TERS (tip-enhanced Raman spectroscopy) uses the tip of a scanning probe microscopy instrument as a source of enhanced field, measuring Raman in the space between the tip and the sample. This can be done by metal coating an AFM (Atomic Force Microscopy) tip or electrochemically etching STM (Scanning Tunneling Microscopy) wire tips. In this way, a high spatial resolution, down to the single molecule, is obtained. A disadvantage is the reduced intensity due to the low amount of material investigated. The challenging experimental setup also represents a limit to the application of this technique. SHINERS (Shell Isolated Nanoparticle enhanced Raman spectroscopy) uses

core-shell nanoparticles with inert oxide shells, thin enough to allow for the molecules in the vicinity of them to feel the enhanced field from the metallic core, but thick enough to protect the surrounding environment from the catalytic action of the metal nanoparticle and prevent particle aggregation. However, enhancement in SHINERS is obtained just close to the nanoparticles, which distribution is inhomogeneous and cannot be individuated by the microscope. Moreover, reagent residues or impurities can contaminate the sample leading to anomalous features in the spectra.

5.1.2. APPLICATION IN INTERPHASE STUDY

In batteries research, Raman spectroscopy has been primarily applied to study electrode materials [173] also under *operando* conditions.[174] *Operando* studies of electrodes helped the development of suitable optical cell setups; nevertheless, for interphase investigation, the use of Enhanced Raman methods is necessary. In fact, interphase thickness ranges between few to hundreds of Å and the investigated species are present just in low amounts.[97] This means that peaks from the bulk electrode and electrolyte will be collected together with interphase species vibrations, which could present very weak or undetectable signals due to a small Raman cross-section and low quantity. The study of the SEI by Raman also complements attenuated total reflectance Fourier transform infrared (ATR-FTIR) studies, allowing to see vibration modes that are not IR active. In the literature, SERS, TERS and SHINERS have been applied for interphase investigation.

SERS was first applied for interphase investigation in 2000 by Li *et al.*.[175] Since silver is plasmonic active and has an alloying mechanism similar to lithium metal, a silver substrate was cycled in a lithium cell and then analyzed, showing Raman bands from LiOH, Li_2CO_3 and lithium alkyl carbonate ($ROCO_2Li$), typical SEI components, that proved the enhancing effect of the substrate.

Common SERS substrates, however, are not suitable for studies on relevant electrode materials. This is why several modified techniques were developed to insert enhancement sources at the surface of the electrode, such as electrodeposition of gold nanoparticles[180] or use of a roughened copper mesh with a 30 nm silicon coating to study Silicon anodes.[176] This second approach allowed in-situ investigation of the interphase. Interphase study on graphene electrodes was possible in Li-air batteries thanks to the production of Au nanorods via mask-sputtering.[177] For studies on Li-metal, Tang *et al*. prepared different lithium

nanostructures and demonstrated their SERS activity. Even if the enhancement was very weak, they could still assign the broad bands detected to SEI components, allowing for a study of the effect of trace water impurities on the SEI composition.[178] Schmitz *et al*. instead used copper SPR effect to study SEI on lithium electrodeposited on top of the metal.[179]

CEI on NMC111 was investigated under *operando* conditions using a monolayer of Au-cubes deposited via Langmuir−Blodgett deposition on the electrode, which showed no influence on the cathode (binder-free NMC111) electrochemistry. They found that the Raman bands could be assigned to polymeric species containing ether and ester links proposed to be formed at the anode. Moreover, they observed that band intensity fluctuated with voltage, being more intense at lower state of charge. Therefore, they suggested that the molecule is more strongly adsorbed at low voltages.[180]

TERS was applied just in one study from Nanda *et al.*, on an amorphous silicon anode with controlled roughness, studied after different numbers of cycles but not in *operando* conditions. Nevertheless, based on their results, they could propose a nano-mosaic multilayer model for SEI. (PEO)-like oligomer and lithium ethylene dicarbonate (LEDC) were found to be the main component after one cycle, mainly LEDC after five cycles and carboxylate compounds after twenty cycles.[181]

SHINERS is an attractive technique for *operando* study of SEI, that can theoretically be applied to any electrode material with easy sample preparation. The drop-casting of the nanoparticles though does not allow for uniform distribution of the enhancing structures, and finding an appropriate spot for an enhanced signal is not trivial.[182] An indication of plasmonic activity can be individuated in the appearance of a continuum background attributed to the effect of inelastic light scattering of electrons within metal nanostructures.[183] Galloway *et al.* were the first to apply SHINERS to study SEI. They investigated lithium-oxygen batteries, therefore, they performed ex situ SHINERS of SEI formed on lithium metal in standard carbonate electrolyte, ether-based electrolytes with or without oxygen saturated electrolytes. Furthermore, they carried on ex-situ and *operando* SHINERS of oxygen reduction upon cycling in the same ether-based electrolyte on different carbonaceous anodes. To enable the study of the lithium surface, they deposited SHIN on the glass window of the optical cell, which was demonstrated effective in obtaining signal enhancement.[184] Cabo Fernandez *et al.* were able to observe in *operando* the formation of polyethylene oxide species (PEO) and different lithium alkyl

carbonate compounds (i. e., $ROCO_2Li$, ROLi, RCOOLi) from the SEI formed on carbon-coated $ZnFe_2O_4$ in 1 M $LiPF_6$ in EC/DMC (1:1 w/w) electrolyte.[182] Gajan *et al.* observed the evolution of the electrode/electrolyte interface upon cycling in LIB coin-cells on tin and gold in 1.0 M $LiPF_6$, EC/DEC (50/50 v/v) electrolyte. By acquisition of reference spectra of common compounds suggested to be formed in SEI originating in carbonate solvents, they could more precisely assign the observed features. They reported lithium ethylene monocarbonate (LEMC) as a main SEI component and the formation and dissolution of 2,5-dioxahexane dicarboxylate (DEDOHC) on tin electrode.[185]

Hy *et al.* investigated in *operando* the SEI formed on silicon anodes in carbonate electrolyte with or without addition of VC. They observed the arising of new bands on the electrodes cycled in VC presence at a potential earlier than EC reduction, deducing that they must correspond to VC reduction products.[186]

6 MOTIVATION

Interphase modification by introduction of electrolyte additives has proven to be an effective method to increase battery performance.[65] In high voltage systems, this is particularly important to contrast capacity fade and sudden cell failure.[103] The study of additive concentration influence in commercially relevant cell systems is also of interest.[187, 188]

To gain a deeper understanding of modification of interphase composition, surface techniques are necessary. Nowadays, XPS is largely employed as a standard technique for interphase characterization. However, it presents some drawbacks intrinsic to the experimental set-up, such as the need for a vacuum that can evaporate interphase components and irreversible sample damage by the electron beam.[189] *In situ/operando* methods are preferred in the interphase investigation to avoid Interphase contamination, decomposition and mechanical damage.[8, 190, 191] Furthermore, *operando* methods allow to gain information on interphase dynamics, including formation and also ageing of the interphase. *Operando* Raman set-ups were already successfully developed for bulk studies of electrode materials.[174] However, the limited amount of material in the interphase and the intrinsic low efficiency of Raman scattering require signal enhancement by plasmonic field. SHINERS allow for the direct addition of plasmonic material at the electrode surface and interphase formation in its vicinity, constituting a highly surface-specific technique, with the additional advantage of reduction of gold surface activity and nanoparticle agglomeration inhibition by the silica shell[192]. The technique has already proved effective in investigating CEI formation on NMC111 with thiophene as electrolyte additive.[76]

This work aims to apply the method to investigate the interphase composition on graphite electrodes and the influence of electrolyte additives on it. The investigated additives are derivatives of EC, which decomposition products are responsible for forming an effective SEI in SOTA electrolyte. FEC and VC, which proved beneficial in reducing electrolyte decomposition and forming improved SEI, share a similar structure, so additional components of this family were investigated, such as ClEC and VEC, as well as BrEC, tmEC, and CF_3EC. The use of other techniques such as CV, galvanostatic charge/discharge cycling, SEM, EDX, EIS, and GC-MS allow further to assess the influence of additives in the cell.

7 MATERIALS AND METHODES

5.1 CHEMICALS AND MATERIALS

Table 1: Overview of the chemicals and materials used within the thesis comprising information about supplier and purity

Chemical / Material	**Supplier**	**Purity**
Ethylene carbonate (EC)	E-Lyte Innovations	battery grade
Ethyl methyl carbonate (EMC)	E-Lyte Innovations	battery grade
Lithium hexafluorophosphate (LiPF6)	E-Lyte Innovations	battery grade
4-fluoro-1,3-dioxolan-2-one (FEC)	abcr GmbH	98%
4-chloro-1,3-dioxolan-2-one (ClEC)	Tokyo chemical industry Co.	>95%
4-(trifluoromethyl)-1,3-dioxolan-2-one (CF3EC)	abcr GmbH	97%
4-bromo-1,3-dioxolan-2-one (BrEC)	Synthesized by collaborator	
1,3-dioxol-2-one (VC)	E-Lyte Innovations	battery grade
4-vinyl-1,3-dioxolan-2-one (VEC)	abcr GmbH	99%
4,4,5,5-tetramethyl-1,3-dioxolan-2-one (tmEC)	Synthesised	
Isopropanol	Sigma Aldrich	99.8%
Sodium Trisilicate	Sigma Aldrich	Reagent grade
Aucl3	Sigma Aldrich	99.995%,
Hydrochloric Acid (Hcl)	Sigma Aldrich	
Sodium Citrate ($NaCH_3COO$)	USP	Reference Standard
3-Aminopropyltrimethoxysilane Solution (APTMS)	Sigma Aldrich	97%
Milliq Water	Merck	18.2 Ω, TOC < 0.2
NMC622||graphite Pouch Cells	Li-FUN Technologies	
Lithium Metal Foil	Albemarle	
Whatman Separators	GE Healthcare	
Li-FUN Cell Holders	Bölling GmbH	
Dichloro Methane	Merck	99.8%
Ammonia	Westfalen, Germany	3.5%

5.2 ELECTROLYTE PREPARATION

All electrolytes were prepared in an argon-filled glovebox (MBraun, H_2O content below 5 ppm and O_2 content below 1 ppm) and stored in an argon-filled glovebox or a dry room (dew point: -50 °C), in aluminum vials. The reference electrolyte was 1.0 M $LiPF_6$ in EC:EMC 3:7 (w/w). Additive-containing electrolytes with concentrations of 0.05 M, 0.15 M, 0.5 M, and 0.75 M of VEC, ClEC, FEC and VC were prepared according to **Table 2**. For VEC, an additional concentration of 0.3 M was prepared. The conversion to weight percentage is reported for comparison with literature.

Table 2: Structure, name and abbreviation of the used additives. Weight and molar concentration of the additives in the prepared electrolytes

	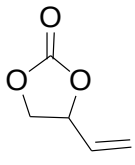	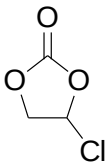	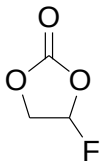	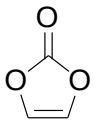
	VEC Vinyl ethylene carbonate	ClEC Chloroethylene carbonate	FEC Fluoroethylene carbonate	VC Vinylene carbonate
Additive	4-vinyl-1,3-dioxolan-2-one	4-chloro-1,3-dioxolan-2-one	4-fluoro-1,3-dioxolan-2-one	1,3-dioxol-2-one
M (mol/L)	**wt.%**	**wt.%**	**wt.%**	**wt.%**
0.05	0.48	0.51	0.44	0.36
0.15	1.43	1.53	1.33	1.08
0.5	4.75	5.10	4.42	3.59
0.75	7.13	7.66	6.63	5.38
0.3	2.85			

Electrolytes with 0.15 M and 0.5 M concentrations of bromoethylene carbonate (BrEC), and and tetramethyl ethylene carbonate (tmEC) were also prepared, and for trifluoromethyl ethylene carbonate (CF_3EC) all the previous concentrations were prepared.

5.3 CELL ASSEMBLY

5.3.1 ELECTRODE PREPARATION

NMC622 and graphite electrodes were punched out from the electrode layer of a Li-FUN cell, after removing the active material from one side. To do so, THF and isopropanol were respectively used as solvents.

5.3.2 SWAGELOK® CELL ASSEMBLY

Swagelok® type T-cells were used for potentiostatic investigation. A working electrode (WE) and a counter electrode (CE) with a diameter of 12 mm each and a reference electrode (RE) with a diameter of 5 mm were used. Li metal was chosen as RE in all prepared cells. Mylar foil was placed in the interior of the cell for electrical insulation. Gasket rings were placed between

all the metallic pieces to seal the cell from the external atmosphere containing oxygen and moisture. A metal spring was placed behind the CE to ensure constant pressure on the WE and CE. Whatman glass fiber separators were used to avoid electrical contact between the electrodes; between WE and CE, a 12 mm one was used, and a 10 mm one for the RE. The separators were soaked with 120 µL and 80 µL of electrolyte solution, respectively. Two cells were built for each investigated system to ensure reproducibility.

5.3.3 LI-FUN PREPARATION

LIB pouch cells with nominal capacities of 200 mAh were obtained from Li-FUN Technology. The small-scale cells are based on a wound cell stack (35 x 20 x 4 mm). The negative electrode was AG (artificial graphite). The positive electrode was NCM622. The cells were capacity-balanced to an operation cut-off voltage of 4.5 V. The cells were vacuum-sealed in a dry state (without electrolyte) and subsequently shipped. Prior to electrolyte filling, cells were opened and dried overnight at 80°C under reduced atmosphere. Then they were filled with 700 µL of electrolyte solution and vacuum sealed (5 sec, 85 mbar, 165 °C) in a dry room with a GELON GN-VPS200 vacuum sealer. For each investigated system, four cells were built to ensure reproducibility.

5.4 POTENTIOSTATIC INVESTIGATION

The electrochemical oxidation and reduction of the electrolyte were investigated by cyclic voltammetry (CV) using an Autolab Battery Tester (Metrohm) controlled by NOVA 2.1 (Autolab) software. Swagelock T-cells were built with reference electrolyte and with electrolytes each containing 0.5 M concentration of investigated additives. Before the CV measurement, the cells were rested for 10 h to ensure sufficient wetting and determine the cell's open circuit potential (OCP). Half cells Li-metal||graphite (WE) were cycled between 0.05 V and 2 V for 3 cycles at a scan rate of 150 µV/s. NMC622||graphite 3 electrodes cells with NMC622 as WE were cycled a scan rate of 150 µV/s in the voltage range 2.8 - 5 V.

5.5 GALVANOSTATIC CYCLING

Constant current (CC) charge/discharge cycling of the Li-FUN cells with different electrolytes was performed in a potential range of 2.8 to 4.5 V and a C-rate of 1 C (1C=200mAh, nominal capacity) until 50% SOH. For formation, after a 24 hours rest time, during which a potential of 1.5 V is applied for pre-polarization, two constant current constant voltage (CCCV) cycles at C-

rate of 0.1 were applied. The cycling was carried on on a Maccor 4000 series battery tester temperature-controlled chamber (BINDER) at 20 °C. After complete cell formation, the cells were transferred into a dry room to be re-opened and degassed by vacuum re-sealing as described above. Li-FUN cell holders were used in order to apply a constant pressure of around 2 bar. A schematic is shown in **Figure 20.**

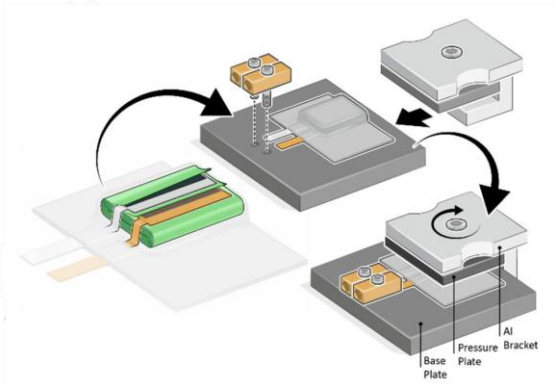

Figure 20: Li-FUN cell holder schematic. [187]

5.6 ELECTROCHEMICAL IMPEDANCE SPECTROSCOPY (EIS)

EIS data were obtained from full Li-FUN cell assembled and cycled as from paragraph 7. 5. FRA measurement was performed at 3.8 V (50% SOH) during charge and discharge for each cycle for 102 cycles. Frequency range was 0.01-10 000 Hz, with 15 frequency/decade. The experiment was performed on an Autolab Battery Tester (Metrohm) controlled by NOVA 2.1 (Autolab) software with incorporated a Frequency Response Analysis (FRA) module (Metrohm). Data manipulation was performed with RelaxIS3 3.0.16 (rhd instruments) software.

5.7 ANALYSIS OF AGED COMPONENTS

5.7.1 GAS CHROMATOGRAPHY - MASS SPECTROMETRY (GC-MS) AND HIGH RESOLUTION-ACCURATE MASS SPECTROMETRY (HRAM-MS)

To study electrolyte decomposition products, selected cycled cells after formation and after 100 cycles were opened in a glovebox under argon atmosphere by cutting the pouch foil and current collectors with a ceramic scalpel. The cell stack was taken, and positive and negative electrodes were separated. The negative electrodes, still surrounded by the separator were transferred into a centrifugation arrangement as introduced by Horsthemke *et al.*.[193] The

pure aged electrolyte was regained by centrifugation (MEGA STAR 600R (VWR), 8000 rpm, 20 °C, 30 min) and diluted 1/100 (v/v) in dichloromethane to precipitate the GC-harmful conducting salt. After precipitation overnight (5 °C, > 12 h), the supernatant was taken for GC-MS analysis.

GC-MS experiments were executed on a Shimadzu GCMS-QP2010 Ultra with assembled AOC-5000 Plus autosampler and a nonpolar Supelco SLB®-5ms (30 m×0.25 mm. 0.25 µm; Sigma Aldrich Chemie, Germany) column. Samples were injected with an injection volume of 1 µL and the GC injector was set at 250 °C. The oven program started at 40 °C, held for 1 min with two subsequent ramps of 3 K min^{-1} to 60 and 30 K min^{-1} to 260 °C which was finally held for 2 min. The ion source was operated in EI mode with 70 eV and the detector voltage was set according to a weekly auto tune. The quadrupole was operated in scan mode in m/z range from 20-350.

GC investigations with high resolution-accurate mass spectrometry (HRAM-MS) detection were performed on a Q Exactive GC Orbitrap GC-MS/MS system with a TRACE 1310 GC and a TriPlus RSH autosampler (all Thermo Fisher Scientific, USA). The MS resolution was set to 60,000 (full width at half maximum (FWHM) at m/z 200). Chromatographic separation was obtained with the same parameters as for the quadrupole-MS experiments. Chemical ionization was performed with ammonia. Detailed experimental parameters were applied according to Peschel *et al.*[194, 195] and non target analysis was performed based on extracted ion chromatograms (EICs) of measured accurate masses with a mass window of 5 ppm.
Measurements were performed by Christoph Peschel.

5.7.2 SCANNING ELECTRON MICROSCOPY (SEM) AND ENERGY DISPERSIVE X-RAY (EDX)

Scanning electron microscopy (SEM) was used to investigate the surface morphology of the SEI formed by the addition of the different electrolyte additives. Electrodes saved from the cells opened for electrolyte analysis were stored in an argon filled glovebox and rinsed with EMC (1000 µL), to remove electrolyte residues. The specimens were transported into the device without exposure to ambient air. The measurements were carried out on a Carl Zeiss AURIGA (Carl Zeiss Microscopy GmbH) coupled with energy-dispersive X-ray spectroscopy (EDX, XMax 80 mm^2 detector, Oxford Instruments) at an acceleration voltage of 3 kV for surface morphology and 15 kV for EDX studies. Measurements were performed by Friederike Reißig.

5.8 NANOPARTICLE SYNTHESIS

For the SHINERS measurements, SiO_2-coated 55 nm Au-NPs were synthesized via the method proposed by Li *et al*..[196] Briefly, 100 mL of 0.01 wt.% $AuCl^{3-}$ solution was added into a round bottom flask. The solution was brought to boil, and 0.7 mL of a 1 wt.% sodium citrate solution was quickly added. The mixture was stirred for 30 min under reflux to obtain Au-NPs with a size of 55 nm.

For coating, 30 mL of the 55 nm Au-NP solution was added into a round bottom flask. Under vigorous stirring, 0.4 mL of a 1.0 mM APTMS solution was added dropwise. The mixture was stirred for 15 minutes at room temperature. Afterward, 3.2 mL of a 0.54 wt.% sodium trisilicate solution (pH = 10; adjusted with HCl) was added. The mixture was heated to 90 °C and stirred for 60 min. Subsequently, the mixture was cooled in an ice bath. To wash the coated NPs, the mixture was centrifuged at 4500 rpm for 15 min at 10 °C. The supernatant was removed and replaced with water. The washing step was repeated twice.

All used glassware was cleaned with aqua regia beforehand and consequently in a base and then acid bath after each use. For the preparation of the solutions and washing of the NPs, only MilliQ-water (Merck, 18.2 MΩ · cm^{-1}) was used.

5.9 RAMAN-SAMPLE PREPARATION

To apply the coated NPs on the surface of the investigated electrode, NPs were transferred to isopropanol. Therefore, the aqueous NP solution was centrifuged for 15 min at 4500 rpm. The supernatant was decanted and replaced with isopropanol. 500 µL of the concentrated NP suspension were drop-casted on the investigated electrode. The electrode was dried at 80 °C overnight under reduced atmosphere.

An airtight optical cell (EL-CELL ECC-Opto-Std) with a glass window was used for the Raman measurement. For the operando SHINERS investigation, a NMC622||graphite two-electrode cell setup was built, with graphite as working and NMC622 as counter and reference electrode. The capacity was balance as for Li-FUN cells to obtain comparable potentials at cut-off voltage. Both electrodes have their active material facing the glass window and are

separated by one layer of Celgard 2500. A copper mesh was placed above the working electrode to ensure sufficient diffusion over the sides. Finally, approximately 200 µL of electrolyte were added to the cell. A schematic setup of the utilized cell is displayed in **Figure 21**.

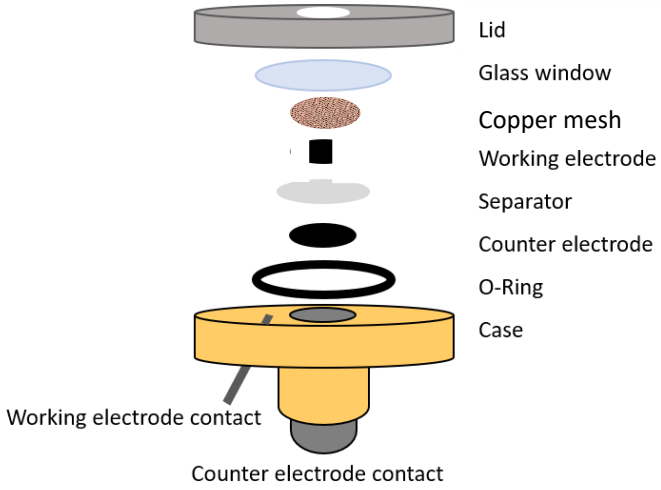

Figure 21: Schematic of the optical Raman cell (Adapted from [76])

5.10 RAMAN ANALYSIS

For interphase investigation, a Horiba Scientific confocal Raman microscope (LabRAM HR evolution, air-cooled CCD detector) was employed. The beam was focused using a 50X long-working distance objective (Zeiss, 9.2 mm, numerical aperture 0.5), leading to a laser spot diameter between 1-2 µm depending on the laser wavelenght. The sample was excited with a red or green laser with a wavelength of 633 nm or 532 nm, adjusted to obtain optimal signal intensity with minimum sample damage by different OD (optical density) filters, with a 600 line/mm grating. Specific parameters of acquisition are specified for each spectrum in figure description. Handling the Raman microscope, collecting the spectra, and evaluating the data were done using LabSpec6.6.2 (Horiba Scientific). Prior to the measurement, the system was calibrated on the silicon peak at a Raman shift of 520.7 cm^{-1}. For operando measurements potential was applied *via* an Autolab Battery Tester (Metrohm) controlled by NOVA 2.1 (Autolab) software.

8 RESULTS AND DISCUSSION

8.1 ELECTROCHEMICAL INVESTIGATION

During the initial additives´ screening, BrEC was excluded due to a degradation of the substance, showed by the NMR spectra in **Figure A1a**. The additive tmEC was also excluded on the basis of cycling data, not showing improved performance and moreover, from the fact that no reduction peak previous to EC reduction potential was detected in the CV (**Figure A1b**). Additionally, CVs performed with electrolytes after two weeks of storage in dry room atmosphere did not show the characteristic reduction peak for the compound (**Figure A1c**). For these two additives, it has to be noted that a different cycling procedure was adopted. In fact, the formation procedure was optimum from 3 cycles at 0.1 C plus 3 cycles at 0.3 C to just two cycles at 0.1 C, with an additional pre-charging at 1.5 V before the rest step, reducing the formation time with no impact on the cycling performance (see **Figure A1d**). Moreover, a degassing step was introduced to align with the common procedure followed in the literature with this kind of cell type. For CF_3EC, no additional peak was detected in the CV (**Figure A2a**). All investigated concentrations did not show improved cycling (**Figure A2b**). Therefore, no additional investigation was conducted for this additive, although polarization showed to be slightly reduced compared to reference (**Figure A1c**). In the following, cells containing electrolyte with an additive will be indicated just by the abbreviation for the additive, and 1 M $LiPF_6$ in EC:EMC 3:7 by weight will be indicated as *reference*. Where not differently indicated potential values are vs. $Li|Li^+$.

The electrolyte oxidative stability was investigated by CV. In **Figure 22,** the first two CVs cycles obtained in NMC622||graphite three-electrodes swagelock T-type cells with NMC622 as WE at a scan rate of 150 µV/s in the voltage range 2.8 - 5 V are reported, for reference and electrolytes with each additive in concentration 0.5 M. For the reference electrolyte in the first anodic scan, a current peak around 4 V is visible, and an additional current up to 5V, probably non-well-resolved peaks. In the first cathodic scan, two smaller peaks around 4.5 V, 4.2 V and a bigger one at 3.6 V are visible. In the second anodic scan, the peak is shifted to 3.8 V, and the peak area is slightly reduced. In the second cathodic scan, the first peak is slightly shifted to 4.4 V, while the second and third peaks undergo just a small change in area.

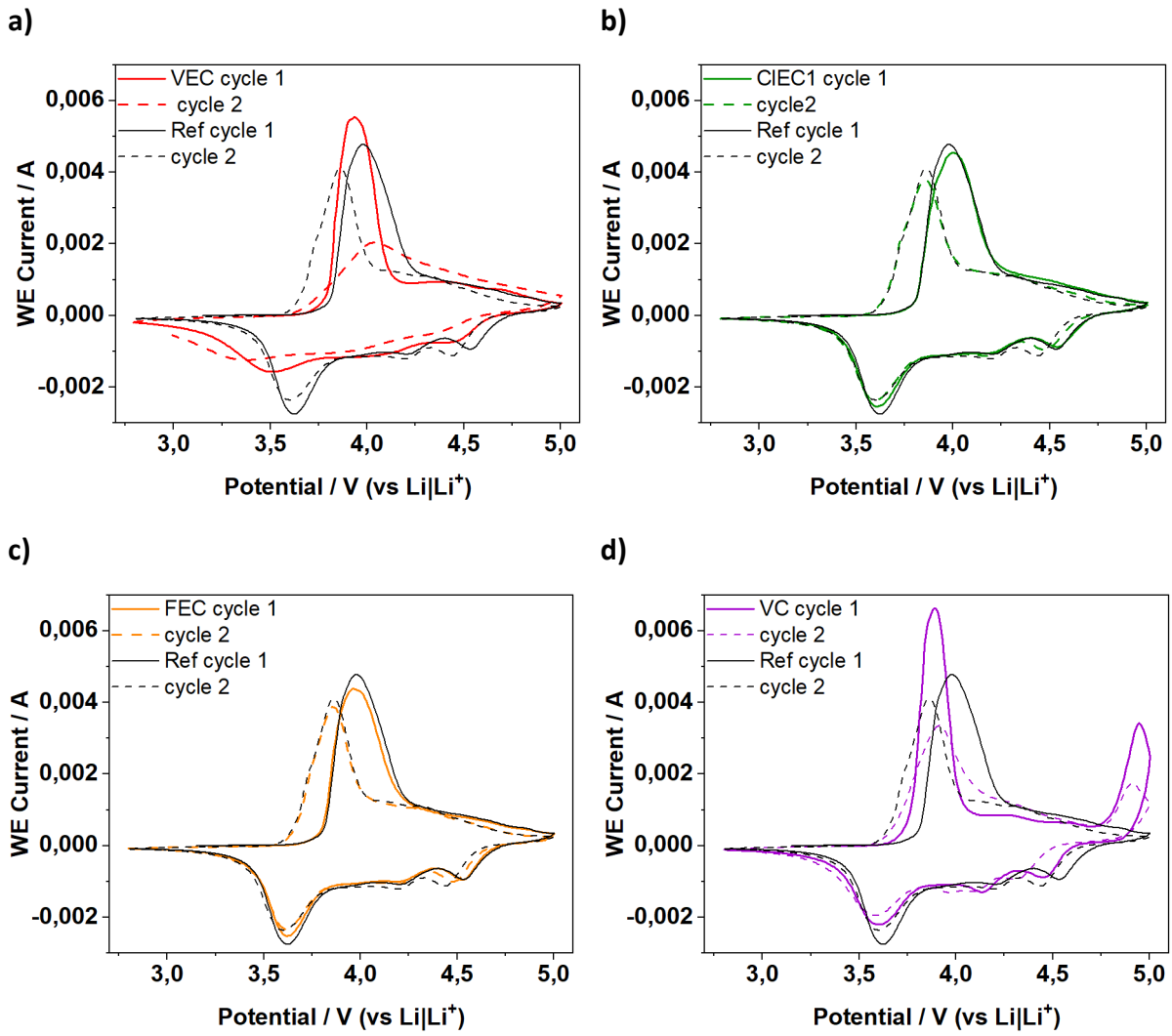

Figure 22: First and second cycle of CV in NMC622||graphite three electrode Swagelock T cell, with NMC as WE. For each electrolyte, additive concentration is 0.5 M and scan rate is 150 µV/s.

The more obvious peak around 4.0 V during the anodic scan and 3.6 V during the cathodic scan correspond to NMC phase transition from hexagonal to monoclinic. The others, well distinct just in the cathodic scan at 4.2 V and 4.5 V, to the multiphase transition between two different hexagonal structures, associated with lithium intercalation and deintercalation in the NMC structure.[197] The addition of ClEC and FEC to the electrolyte does not show particular changes in the CVs features (**Figure 22b** and **c**). For VEC (**Figure 22a**) instead, the anodic peak is less broad in the first cycle, while it is shifted to higher potential and flattened in the second cycle. All the cathodic peaks are flattened and shifted to lower potential, indicating an overvoltage for lithium insertion and de-insertion after the cut-off potential is reached. For VC (**Figure 22d**), the anodic peak is shifted to lower potential with respect to the reference, and no shift is observed in the second cycle. Moreover, an additional anodic current is visible in both cycles at 4.7 V, corresponding to VC oxidation at high potential, outside the voltage range

applied for galvanostatic cycling. [198] In the cathodic scan, a shift is visible, especially for the first and second peaks both compared to the reference and from the first to the second cycle, indicating an overvoltage for lithium insertion, more accentuated at higher voltage.

Cells containing different concentrations of each additive, as from **Table 2** in *section 7.2,* were cycled in order to find the optimal concentration for each investigated electrolyte system**.** The cells were cycled up to 50% SOH to be able to observe the additive influence on cell failure, which was observed for the reference. The sudden failure observed could be related to rollover failure due to TM dissolution and micro short-circuiting from lithium dendrites.[113] Improvements in discharge capacity for lower state of health values could be valuable from the perspective of second-life applications; the technical specifications needed for retired batteries to be used for a second life are often less rigorous than those required for their initial use. Second-life applications are for instance low-speed electric bicycles and motor cars, small-scale distributed energy storage systems (ESSs) for homes and street lighting, and large-scale stationary ESSs for buildings as backup power supplies and for renewable energy generation and grids.[199] The spikes that can be observed in the discharge capacity data and other related quantities are due to the stop and restart of the cell for instrument maintenance, but a few cycles after reconnection, the capacity recovered due to charge relaxation goes back to the previous behavior.

The specific discharge capacities over cycling of the investigated concentrations for each additive are shown in **Figure 23.** For VEC (**Figure 23a**), the highest concentration is detrimental, showing an immediate fall of the discharge capacity leading to 50% SOH after just 50±5 cycles. The 0.5 M concentration shows a stabilized capacity: there is a large capacity loss in the initial cycles leading to a low capacity value of 134.5±0.7 mAh/g in the first cycle after formation, but thanks to the absence of sudden failure, after around 360 cycles the discharge capacity is better than for the reference, which after 413±7 cycles has already reached 50% SOH, and eventually SOH higher than 50% is maintained up to 1100 cycles. The 0.05 M concentration has discharge capacity values close to reference but improved life-time of about 50 cycles, while the 0.15 M concentration improves discharge capacity at every state of health. The capacity fading is faster in the first 200 cycles, then it is slowed and sudden cell failure starts around 500 cycles leading to 50% SOH at 720±48 cycles.

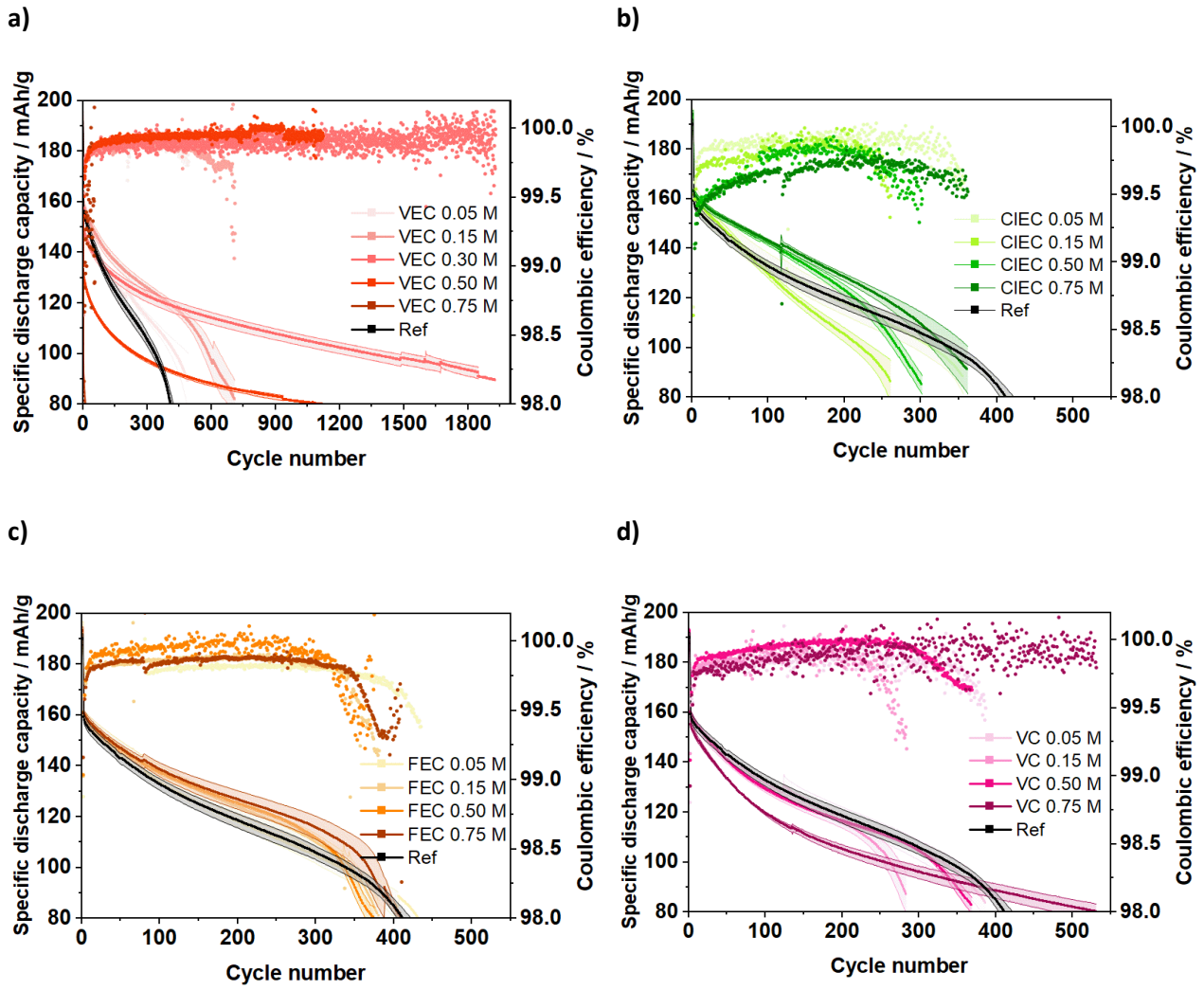

Figure 23: Specific discharge capacity and Coulombic efficiencies of the tested concentrations as reported in the legend in picture for **a)** VEC **b)** ClEC **c)** FEC and **d)** VC

After analyzing the first results, an additional concentration of 0.3 M was tested for this additive to possibly obtain both improved capacity and long cycle-life thanks to a less pronounced capacity fading, as it was shown by the 0.5 M concentration. This concentration shows, as VEC 0.5 M, an initial lowered discharge capacity of 150.7±1.3 mAh/g, but after 85 cycles, better values than the reference are obtained and after 420 cycles it also outperforms the 0.15 M concentration. After 1800 cycles the SOH is superior to 60% (see **Figure A3a**). This concentration was thus chosen as the best concentration.

For ClEC (**Figure 23b**) the lowest concentration (0.05 M) has discharge capacity values comparable to the reference, with values on average slightly higher in the first 70 cycles and failure occurs about 50 cycles earlier. The 0.15 M concentration shows sustained capacity fading and, despite the discharge capacity is initially higher than for reference, a sustained capacity fade leads to values lower than reference after just 100 cycles, and 50% SOH is

reached after just 280±33 cycles. Discharge capacity is instead improved compared to reference for 0.5 M and 0.75 M concentrations, with the higher concentration showing longer cycle life. Their behavior is in fact similar for the first 100 cycles. At 100 cycles, they show a discharge capacity of around 140 mAh/g, compared to 130 mAh/g for reference. However, after 200 cycles the 0.5 M concentration starts to fade in a more sustained way and reaches 50% SOH after 308±8 cycles. ClEC 0.75 M instead fades more slowly, but on average, it still reaches 50% SOH earlier than the reference (391±30 cycles).

For FEC (**Figure 23c**), the lowest concentration, 0.05 M, behaves similarly to the reference. All concentrations higher than 0.05 M result in a slight increase in capacity compared to the reference electrolyte, with 0.75 M concentration being, on average, the most beneficial. After 100 cycles, the capacity improvement is just about 5 mAh/g for all the concentrations compared to the reference, while with increasing cycle number, the capacity improvement is, on average, increasing with concentration. However, the 0.50 M and 0.15 M concentrations show earlier sudden capacity fade at around 320 cycles and reach 50% SOH after 373±11 cycles and 385±9 cycles, respectively. The 0.75 M concentration instead starts to fail at around 345 cycles on average and reaches 50% SOH as the reference at 402±12 cycles

For VC (**Figure 1d**), the lowest concentration (0.05 M) has a behavior very similar to the reference, except for a little anticipated start of sudden capacity fade, which leads it to 50% SOH at around 390 cycles on average. The 0.15 M concentration presents capacity values just slightly inferior to the reference, but after 200 cycles, it presents sudden capacity failure and reaches 50% SOH at 294±9 cycles. There is no correlation between the fading behavior with concentration since the higher concentration of 0.5 M behaves more similarly to 0.05 M, starting to fail after 300 cycles and reaching 50% SOH at 376±9 cycles. The concentration of 0.75 M was chosen to be further investigated due to its longer cycle life, over 500 cycles, and absence of sudden cell failure, even if the capacity is sensibly lowered. In fact, it already presents an initial lower capacity value of 154.9±1.3 mAh/g after formation, and after 100 cycles, a low value of 119.0±0.8 mAh/g is reached, already lower than 80% SOH.

As shown in **Figure 23,** VEC and ClEC show the most obvious improvement in discharge capacity compared to the reference, for optimal concentration. Looking at VC (**Figure 23d**), none of the tested concentrations outperforms the reference electrolyte. For FEC, just a slight increase in capacity was obtained throughout cycling, with no major influence on the fading.

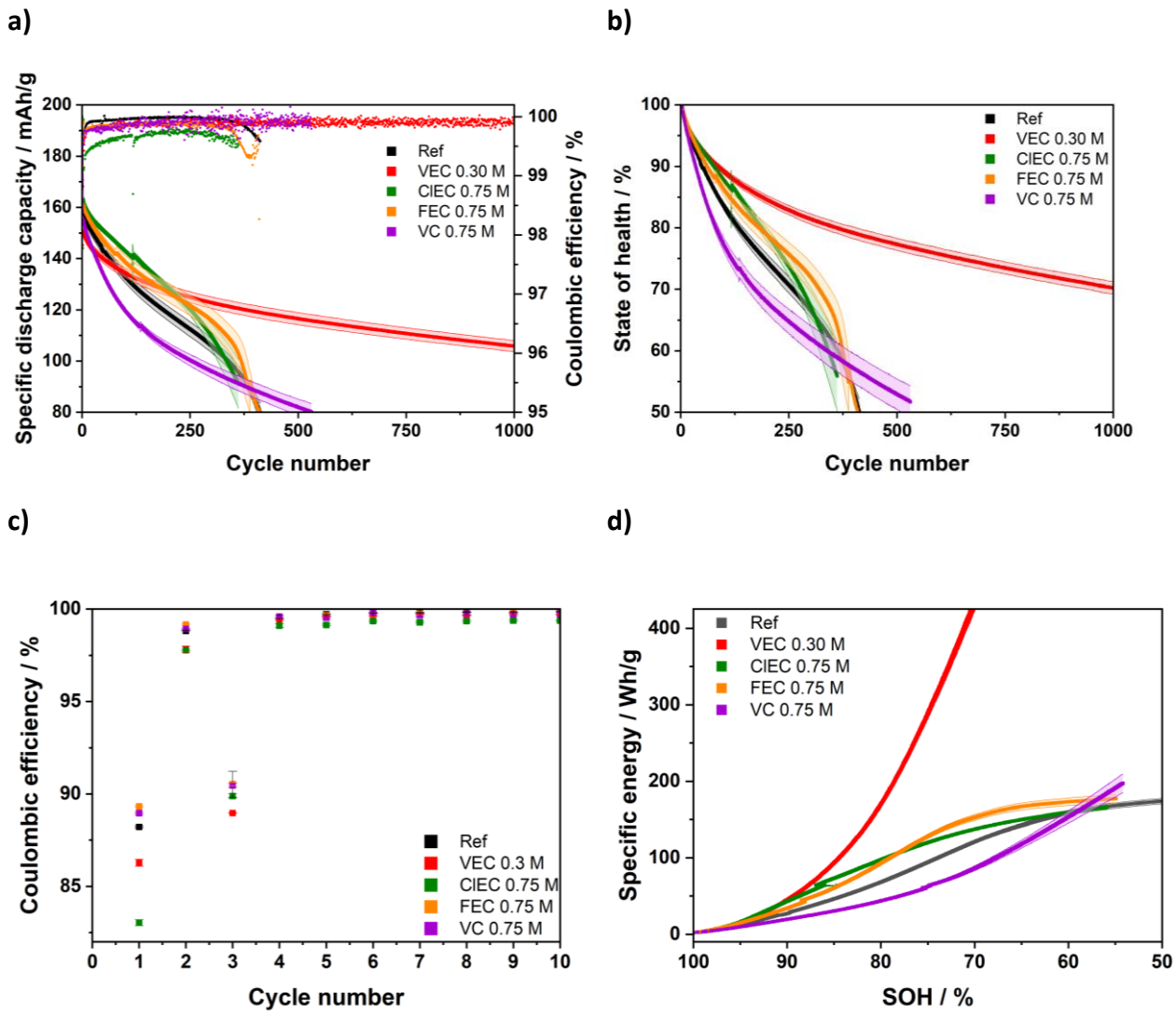

Figure 24: a) Discharge capacity, **b)** normalized capacity (state of health), **c)** initial Coulombic efficiency, **d)** accumulated energy for the optimum concentration of each additive.

The best concentration for each additive is further studied, and will be indicated as *optimum concentration*. Moreover, cycling data will be shown just up to cycle number 1000 for a better comparison; the complete range can be found in the Appendix (**Figure A 4**).

In **Figures 24a** and **b,** the discharge capacity and normalized capacity for the optimum concentration of each additive are directly compared. Iin **Figures 24b** and **c** Coulombic efficiencies relative to the initial cycles and the accumulated energy in function of the state of health are reported. Regarding the average Coulombic efficiencies during cycling, shown in **Figure 24a**, it can be noticed that for all the additives, the Coulombic efficiency is inferior to the one for the reference electrolyte. For ClEC, in particular, the lowest values (<99.8 %) are observed. This can be explained to be due to the presence of soluble reduction product LiCl that is shuttled and oxidized to Cl_2 on the cathode side. The Cl_2 gets reduced at the anode side,

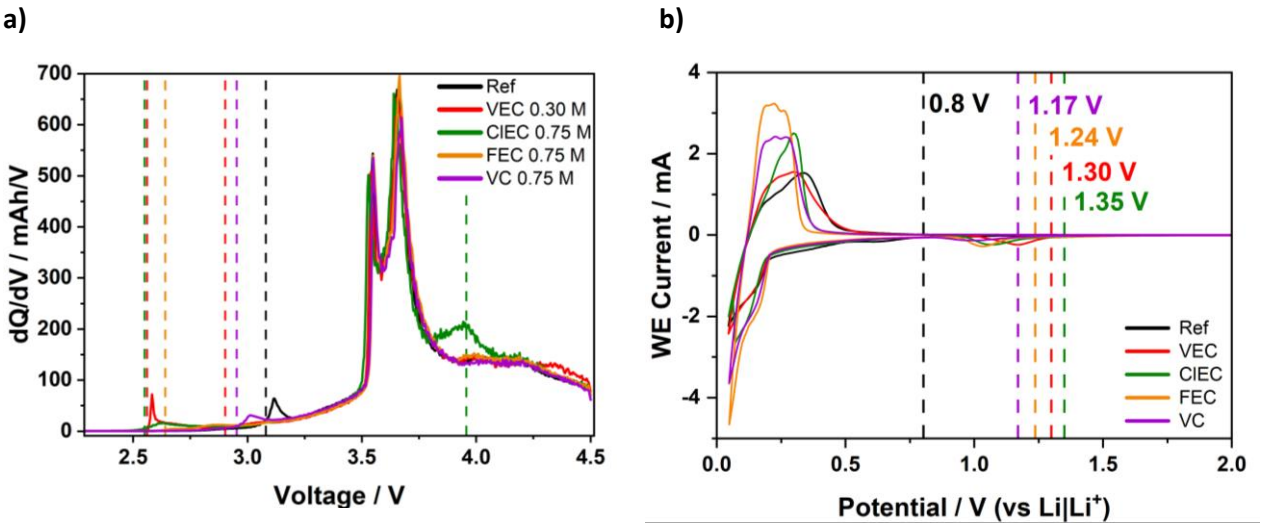

Figure 25: a) Differential capacity plot (dQ/dV) for the first charge of cells with optimum additive concentration. **b)** First cycle of CV in Li-metal||graphite three electrode Swagelock T cell, with graphite as WE. For each electrolyte, additive concentration is 0.5 M and scan rate is 150 µV/s. Dotted lines indicate the onset of the peak, defined as the potential where the current grows over - 0.05 mA

constituting a continuously charge consuming reaction, as reported by Shu *et al.*, which could also worsen the self-discharge behavior of the battery.[166] The reduced Coulombic efficiency for the other additives indicates that parasitic reactions are taking place, which indicates electrolyte reduction and interphase formation. Moreover, Coulombic efficiency shows a similar behavior in correlation with the sudden capacity decrease. As clearly noticeable from the accumulated energy plot (**Figure 24d**), the initially lower discharge capacity for VEC is compensated in the long run by its stability and absence of rollover failure, while ClEC, in the long run, tends to be outperformed by FEC. VC instead shows an advantage just towards 50% state of health due to the absence of sudden failure. Initial Coulombic efficiency (**Figure 24c**) is improved with respect to reference for FEC and VC, while for VEC and ClEC lower values are reached, indicating a high charge consumption during the initial formation.

Figure 25a reports the differential capacity (dQ/dV) plot of the first charge for each optimum concentration. **Figure 25b** shows the CVs obtained in Li-metal||graphite three electrode swagelock T-type cells, recorded for electrolytes containing each additive in concentration of 0.5 M. WE was Graphite, CE and RE were metallic lithium.

The dQ/dV plot allows better visualization of plateaus in the voltage-capacity curve, corresponding to charge-consuming processes, as peaks. Here it is possible to observe small peaks at low voltage, at different values for each additive, which onset potential is evidenced by dotted lines, indicating the additive reduction voltage in the full cell. These are located before the major peaks at 3.5 V and 3.6 V corresponding respectively to lithium intercalation

into the graphite anode and to the phase transition from a hexagonal to a monoclinic lattice symmetry of NMC due to nickel and cobalt oxidation associated to lithium deintercalation[200]. For all the additives, the reduction peak is at lower voltages than the one for the reference, corresponding to ethylene carbonate reduction, visible at 3.1 V. This peak is not present when additives are incorporated in the electrolyte, indicating that the surface is modified such to whether block EC reduction or to shift it to higher voltages. For VEC, a second small peak is visible with an onset around 3.0 V, as can be seen more clearly in **Figure A5**, where the difference in the reduction peak for different concentration is displayed. This graph shows that the first reduction peak is growing and shifting at lower voltage for increasing VEC concentration. The second peak is also slightly growing with concentration and a peak at the same voltage as EC reduction is visible for the concentrations of 0.75 M and 0.05 M, suggesting ineffective passivation of the surface for these concentrations. Moreover, an additional peak can be observed for ClEC, centered around 3.9 V, suggesting additional reactions are taking place. This is in accordance with what can be observed in the CVs in **Figure 25b**. Here a reduction peak is observed at higher potentials than for the reference, and no peak is present at EC reduction potential (0.8 V) for all the additive-containing electrolytes, in agreementwith previous reports[156],[160]. Respectively, the peak onset is positioned at 1.35 V for ClEC, 1.30 V for VEC, 1.24 V for FEC and 1.17 V for VC. It can be observed that even if a slow current appears early for ClEC, the peak is centered just slightly earlier than the FEC reduction peak, as it would be expected from the similar structure. Again, EC peak could be shifted to lower potentials due to surface modification from additive decomposition products and so being hidden under the intercalation peaks.

In **Figure 26a,** the Nyquist plots obtained for each electrolyte from EIS measured in the full NMC622||graphite Li-FUN cell, at 3.8 V (50% state of charge, SOC) during the first and 100th charge after formation and the relative fit are reported. The full impedance evolution along cycling can be seen in **Figure A2.** Data points at frequencies lower than 1.7 Hz have been excluded in the analysis, due to a large deviation from linearity, calculated from Kramers-Kronig relations. The resulting points have been fitted with an equivalent circuit model in **Figure A3**, with number of elements of the C block varying from 2 to 3 to obtain the best fit (three elements were used to fit ClEC and VC after 100 cycles).[201] Inductance is included in block B to take in account the effect of external circuitry and of the wound electrodes. Constant phase element (CPE) are introduced in parallel to the resistance to form so-called

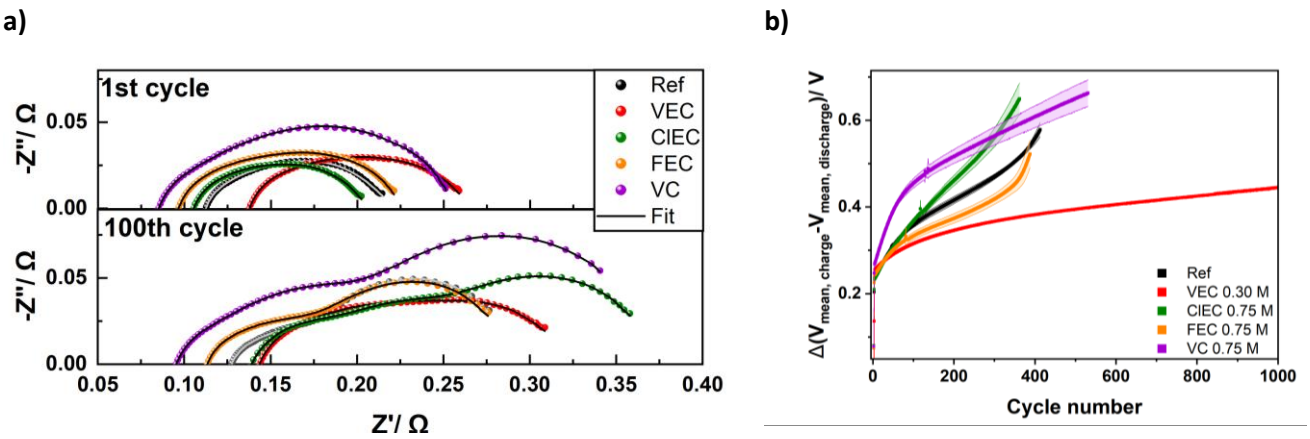

Figure 26: a) Nyquist plots of the full NMC622||graphite Li-FUN cell, at 3.8 V (50% SOC) during the first and 100th charge after formation for optimum additives concentration and reference and the obtained fit, as reported in the legend. **b)** Difference between average charge and discharge voltage *ΔV*, for optimum concentration of each additive and reference.

ZARC elements, that take in account the inhomogeneity of the surface through a distribution of relaxation times. The values obtained from fitting for cycles 1 and 100 are reported in **Table A1.** Although a good fit is obtained through ZARC elements, the very flattened semicircles, as indicated by low α values, do not allow to well separate the contributions from different frequency regions to physically interpret them. Moreover, the inductance contribution from wound electrodes, that cannot be removed, influences the mid frequency region (kHz) where the interphase semicircle is found, leading to artificially low SEI resisistance values.[202] However, what can be extracted from the collected data is the total cell resistance. While for VC and ClEC a large total cell resistance of 0.34 Ω and 0.36 Ω is observed after 100 cycles, for FEC and reference a lower resistance of 0.28 Ω is observed. For VEC an intermediate value of 0.31 Ω is registered, however for this cell a shift in the high frequency region that can arise from different contact resistance of the cell holder is visible, so the real value might be lower. Qualitatively it can be observed that throughout cycling for VEC, compared to reference and the other additives, there is a less pronounced growth of the semicircle in the frequency region around hundreds of Hz, corresponding to charge transfer. This might indicate that the formed interphase in presence of VEC can slow the electrode degradation at the origin of charge transfer resistance growth.

In **Figure 26b** the evolution of the difference between average charge and discharge voltage (*ΔV*) is shown. The change of *ΔV* with cycle number gives an indication of the internal resistance changes taking place during DC cycling, thus, small slopes are most desirable. As shown in **Figure A5b,** the increase in difference for all the cells is mostly due to a decrease in

the average discharge voltage**.** All the cells present a steeper *ΔV* growth in the first 50 cycles and then follow different behaviors. Initial values are between 0.23 and 0.28 V, with ClEC and reference presenting similar low values, while the value grows in the order for FEC, VEC and VC. After 30 cycles, the *ΔV* is lowered compared to the reference for FEC and VEC. ClEC grows with a steady steepness so that already before the 100th cycle, it surpasses the reference and keeps growing. After 100 cycles, *ΔV* is 0.358±0.006 V and 0.367±0.003 V for reference and ClEC, respectively, 0.3158±0.0018 V for VEC, 0.333±0.009 V for FEC, and 0.454±0.011 V for VC. After this point for VC the already high values keep growing at a pace comparable to FEC and reference, so that at the end of life *ΔV* is 0.66±0.03 V. For FEC there is a sudden increase when failure starts, as for the reference, leading to final values of 0.52±0.3 V and 0.578±0.016 V respectively. For VEC the *ΔV* increases constantly at a lower rate, so that at 1000 cycles it is 0.444±0.003 V. The steep growth of ClEC leads to a *ΔV* of 0.674±0.020 V at end of life.

8.2 SURFACE STUDY

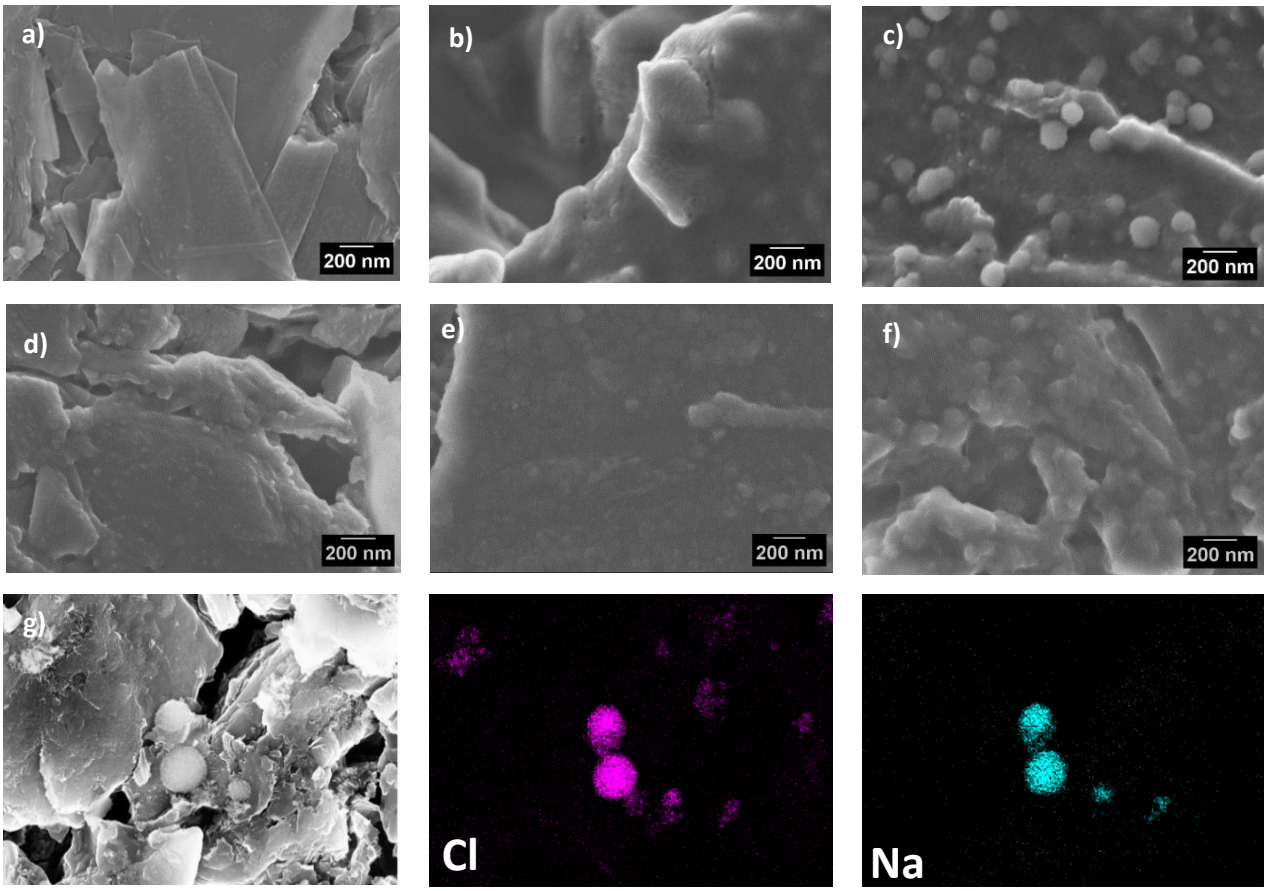

Figure 27: Scanning Electron Microscopy images of graphite anodes respectively **a)** pristine**,** or after 100 cycles in **b)** reference **c)** VEC **d)** ClEC **e)** FEC **f)** VC electrolytes with optimum additive concentration. **g)** Energy dispersive X-ray images of graphite anodes cycled in ClEC containing additive

Scanning electron microscopy images of graphite negative electrodes taken from Li-FUN cells after 100 galvanostatic charge/discharge cycles are shown in **Figure 27**. Images with lower magnification, showing the interphase distribution on the flakes, are reported in **Figure A6**. Here it is possible to observe the presence of SEI with different morphologies, depending on the electrolyte composition. For the reference, a uniform, smooth and dense film covers all the flakes. For VEC the coverage on the anode surface has a clearly different morphologhy: spherical patches are homogeneously distributed on top of a dense, uniform layer. For ClEC the surface looks covered by patches of surface layer. Moreover, here and there, big fluffy-like spheres and other deposited pieces of material with different morphology can be observed on electrodes cycled in ClEC (see **Figure A6d**). From EDX data (**Figure 27g**) it is possible to identify a high concentration of sodium and chlorine in correspondence with the spheres, indicating NaCl formation. Since the binder typically present in the anode is sodium containing Carboxymethylcellulose (CMC-Na), this indicates that the additive decomposition leads to chloride formation, which reacts with the binder. For FEC, different textures are visible: some graphite flakes are covered by a smooth interphase as the one in **Figure 27e,** while a more inhomogeneous morphology is observable in the lower part of **Figure A6e**. For VC the surface is completely covered by a rough, cauliflower-like film.

8.3 ELECTROLYTE DECOMPOSITION INVESTIGATION

Figure 28a shows the GC results obtained from electrolytes recovered from Li-FUN cells after 100 galvanostatic charge/discharge cycles. Remarkably, peaks at retention times of around 2.3, 5, 12 and between 14 and 15 minutes are present just for reference and VEC. For the other additives, just peaks corresponding to electrolyte components are detected, including the additive. ClEC additionally presents some peaks between 6 and 10 minutes, which will be discussed later. The additive peaks, detected at 4 minutes for VC, 6.8 minutes for FEC, 10.2 for ClEC and 10.5 for VEC have been assigned through measurement of each pristine electrolyte, allowing to match the mass spectra for the additive fragments pattern. The peaks at retention times of 2.3 and 5 minutes, respectively can be clearly assigned to DMC and DEC. DEC and DMC are reported in literature as transesterification products of EMC under electrochemical aging, proposed to be activated by lithium alkoxyde.[203] Peaks at higher retention times (11.5, 11.9, 12.3, 13 minutes and 14.3, 14.6 minutes) can instead be assigned to di- and tri-carbonates with increasing alkyl chain lengths. These products result from multiple formation

pathways involving EC decomposition to give lithium ethyl monocarbonate (LEMC) as reactive species.[6] The absence of these species in cycled VC, FEC and ClEC electrolytes indicates the ability of these additives to prevent EC decomposition. The presence of these peaks for VEC instead can indicate EC decomposition, in contrast to what was seen from dQ/dV and CV results. It can be excluded that these products come from VEC reduction, in fact, from theoretical calculations of VEC reduction pathways, no carbonate oligomers are contemplated as possible products.[157] Moreover, a similar result was obtained by Petibon *et al.* in which they performed the same measurement in cells charged up to increasing voltage, proving that after VEC reduction peak, the additive is consumed, but no additional soluble products are detected, while the products are detected after the voltage corresponding to EC reduction, in a NMC111||graphite pouch cell with reference electrolyte plus 3% VEC.[161] Nevertheless, they reported that VEC is completely consumed after formation, which is not the case here, as shown in **Figure 28b**, where the additive peaks are compared after formation and after 100 cycles. This could be due to a lower electrolyte amount to electrode surface area ratio. They also reported no major improvement by VEC addition in a previous work in LCO||graphite pouch cells, even when varying VEC content.[162]

The main difference in this study is the use of NMC622 as cathode material, and the cut-off cell voltage is increased to 4.5 V. It can be speculated that the difference in performance is mainly ascribed to the modification of the cathode surface by the additive. Moreover, concerning SEI, SEM on the graphite surface shows the formation of a quite different SEI when VEC is added, which also can play a beneficial role on the performance (Section 8.2). A plausible explanation could be that since EC is still reduced, VEC reduction may form unsoluble products that modify the interphase but cannot completely passivate it. Then a good SEI can be formed from a reaction of VEC and EC reduction products, which resulting products are not detected in GC-MS because unsoluble (or not volatile). It could also be that VEC and EC reduction products coexist on the surface and have a synergic effect. Since from SHINERS results (Section 8.4), a change in the surface products is seen between -4.0 and -4.5 V, another hypothesis is that decomposition takes place at higher potentials, with cross-talk of products to the anode. Then the difference in cut-off voltage would also explain the difference in performance improvement compared with Petibon *et al.*[162]

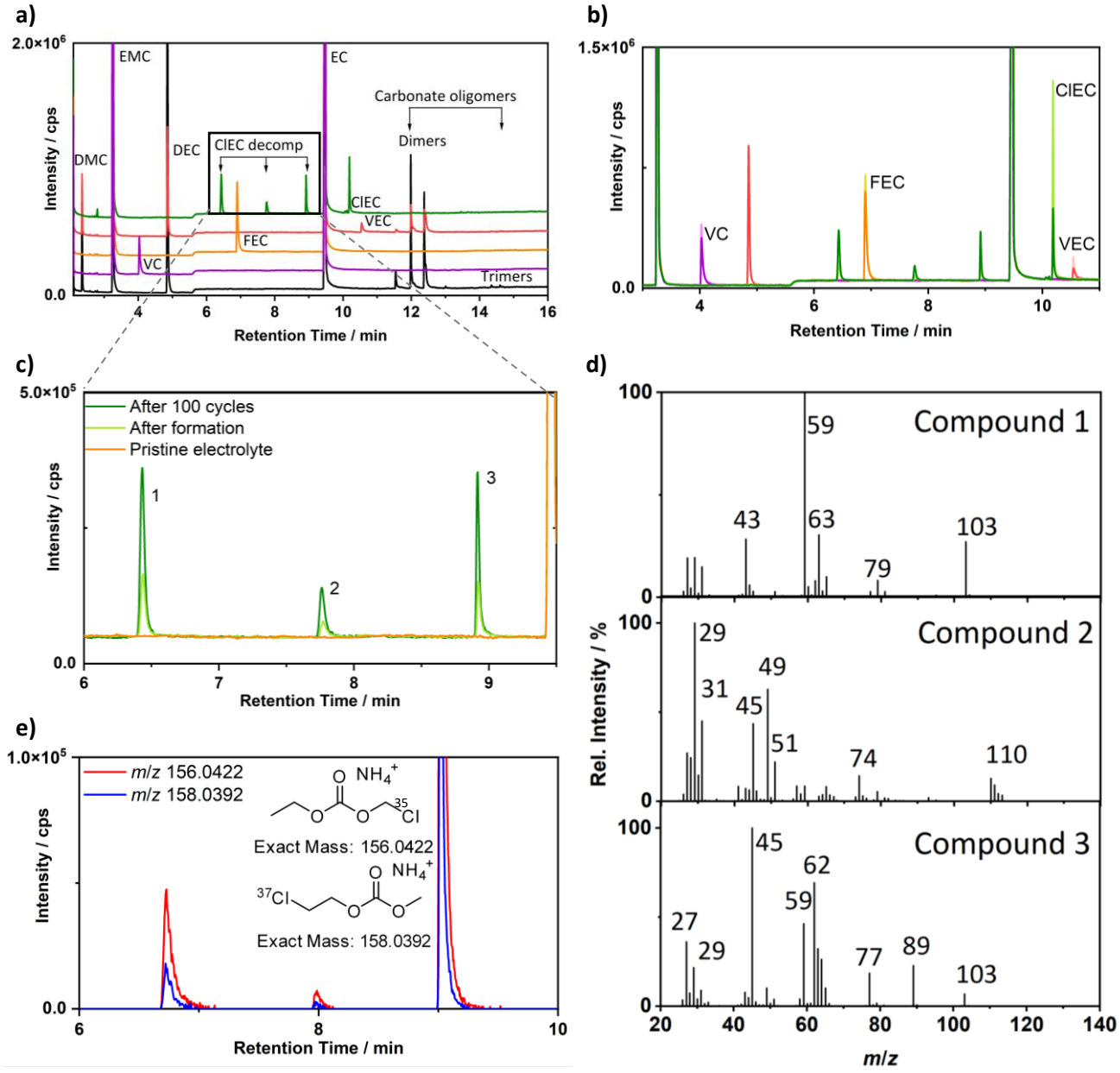

Figure 28: Comparison of GC-MS chromatograms of the electrolytes recovered from galvanostatically charged/discarged NMC622||graphite Li-FUN cells: **a)** for optimum concentrations of each additive and reference after 100 cycles; **b)** for each additive and reference after formation (light colors) and after 100 cycles (saturated colors),focusing on the retention times of the investigated additives; **c)** for ClEC, after 100 cycles, after formation and the pristine electrolyte, limited to retention times of ClEC's decompositions products. **d)** Mass spectra of the fragment pattern obtained by electron ionization at the retention times corresponding to peaks 1, 2 and 3 in the chromatogram in c. **e)** Extracted ion chromatograms of the characteristic chlorine containing $[M+NH_4]^+$adducts formed by chemical ionization using ammonia as reagent gas, selected m/z of 156.0422 and 158.0392 were extracted with a mass window of 5 ppm. **f)** Proposed structures of the three individuated compounds.

Interestingly, for ClEC additional decomposition products were detected. In **Figure 28c**, by the comparison between the chromatogram after formation, after 100 cycles and for the pristine electrolyte, it is possible to see that these compounds are not detected in the pristine electrolyte, while after 100 cycles, the peak area is increased compared to after formation. Therefore, it is possible to conclude that they are formed from electrochemical aging.

In **Figure 28d,** the electron ionization mass spectra of peaks **1**, **2**, and **3** in the chromatogram in **Figure 28c** are displayed. Since NIST database comparison gave no reasonable hit, chemical ionization *via* ammonia was performed. As shown in **Figure 28e,** gas chromatography with chemical ionization and OrbitrapMS detection resulted in three peaks at similar retention times for the m/z ratios of 156.0422 and 158.0392. Slight differences in the retention times are due to the different system and ionization mode.

To elucidate the chemical structure, fragment patterns from electron impact ionization in **Figure 28d** were used. **Compounds 1** and **3** show the characteristic mass 103 (exact mass 103.0390 measured by GC-HRMS), corresponding to $C_4H_7O_3$, that can be obtained by the loss of Cl in two different positions, leading to the **Structures 1** and **3** in **Figure 28f**. **Structure 3** also fits well to the HRMS fragment pattern, reported in **Figure A8** for compound 3, since mass 63 and 65 correspond to C_2H_4Cl fragment for the two isotopes, that can be obtained just from this isomer. For **Compound 1** instead, mass 62 and 64 corresponding to C_2H_3Cl fragment are detected. To assign which one of these structures corresponds to the peak 1 and which to the peak 3 in **Figure 27c** it is necessary to look at the fragment of m/z 89, that corresponds the loss of CH_2Cl, which is more likely for **Structure 1**. For **Compound 2** the m/z of 110 can be obtained by loss of a C_2H_5 from the original mass formula $C_4H_7ClO_3$, which is possible in a structure where Cl is connected to the methyl side of the carbonate, as for **Structure 2** in **Figure 27f**, further confirmed by mass 49, and 51 in case of ^{37}Cl, that corresponds instead to the loss of CH_2Cl. An additional confirmation of the proposed assignment comes from the fact that increasing boiling points are in line with the observed increasing retention time for the three compounds on the applied non polar column. In fact, calculated boiling points at 1 atm for compounds 1, 2, and 3 are respectively 127.3 ± 23 °C, 135.123 ± 23 °C and 157.0 ± 13 °C.[205–207] These reduction products could be formed from ClEC ring opening in different position, with relative amounts corresponding to the ease of the bond breakage. Then oxoalkyl anions in solution (OEt^- and OMe^-) could lead to change of the ester chain. However,

SEM and EDX results (Section 8.2) that showed NaCl formation, suggest that ClEC can also undergo dechlorination to form Cl^- that can react with Na^+ at the graphite surface. The oxoalkyl anions could then also substitute the chlorine and form PEO-like ring opening products. Looking at further characteristic peaks and extracted ion chromatograms with GC-OrbitrapMS, further chlorinated carbonate structures were detectable at higher retention times, not elucidated in detail, yet.

Semi-quantitative comparison of the additive peaks after formation and 100 cycles in **Figure 28b,** indicates that ClEC is more consumed during cycling with respect to other additives, which could explain the earlier failure by the fact that ClEC is completely consumed earlier. Nevertheless, ClEC might also lead to early failure due to adverse effects of some among the plethora of reduction products formed.

8.4 *OPERANDO* SHINERS

Figure 29 shows the SHINERS spectra acquired at OCP and -4.5 V vs. NMC (cut-off voltage) and after holding the potential for 30 minutes on graphite anode. In all the spectra, it is possible to observe the graphite D and G band around 1300 and 1580 cm^{-1}, respectively. However, it was observed that these bands disappear at cut-off voltage due to graphite lithiation, as it can also be observed from the goldish color in **Figure A10f**.[208] This is an indication of the fact that the electrochemistry in the system is working properly.

For the reference electrolyte (**Figure 29a**) a new band around 570 cm^{-1} was observed at -4.5 V that can be assigned to lithium alkyl carbonates.[97] A band around 1850 cm^{-1} can also be assigned to lithium carbide (Li_2C_2), reported in the literature as a laser-induced decomposition product of organic lithium carbonates.[186, 209, 210] Some other bands were identified during charging. At -2.4 V bands around 577 cm^{-1}, 1040 cm^{-1} (ν C-O) are visible that can be assigned to lithium alkyl carbonate species,[97, 196] around 1089 cm^{-1} (ν C-O) that can be assigned to organic or inorganic carbonate species[178, 184] and around 1540 cm^{-1} that can be assigned to $RCOO^-$ vibrations.[211] The band around 1089 cm^{-1} is also visible at -3 V.

For VC (**Figure 29b**) at -4.5 V, bands around 556 cm^{-1}, 842 cm^{-1} (δ CO_3^{2-}) can be assigned to lithium alkyl carbonates.[97, 212] The band around 780 cm^{-1} can be assigned to CO_2^- bending of lithium formate that can be formed in the presence of CO_2, known to be formed in presence of VC.[97, 213] A band around 1030 cm^{-1} can be assigned to semi-carbonates like DEDOHC.[185]

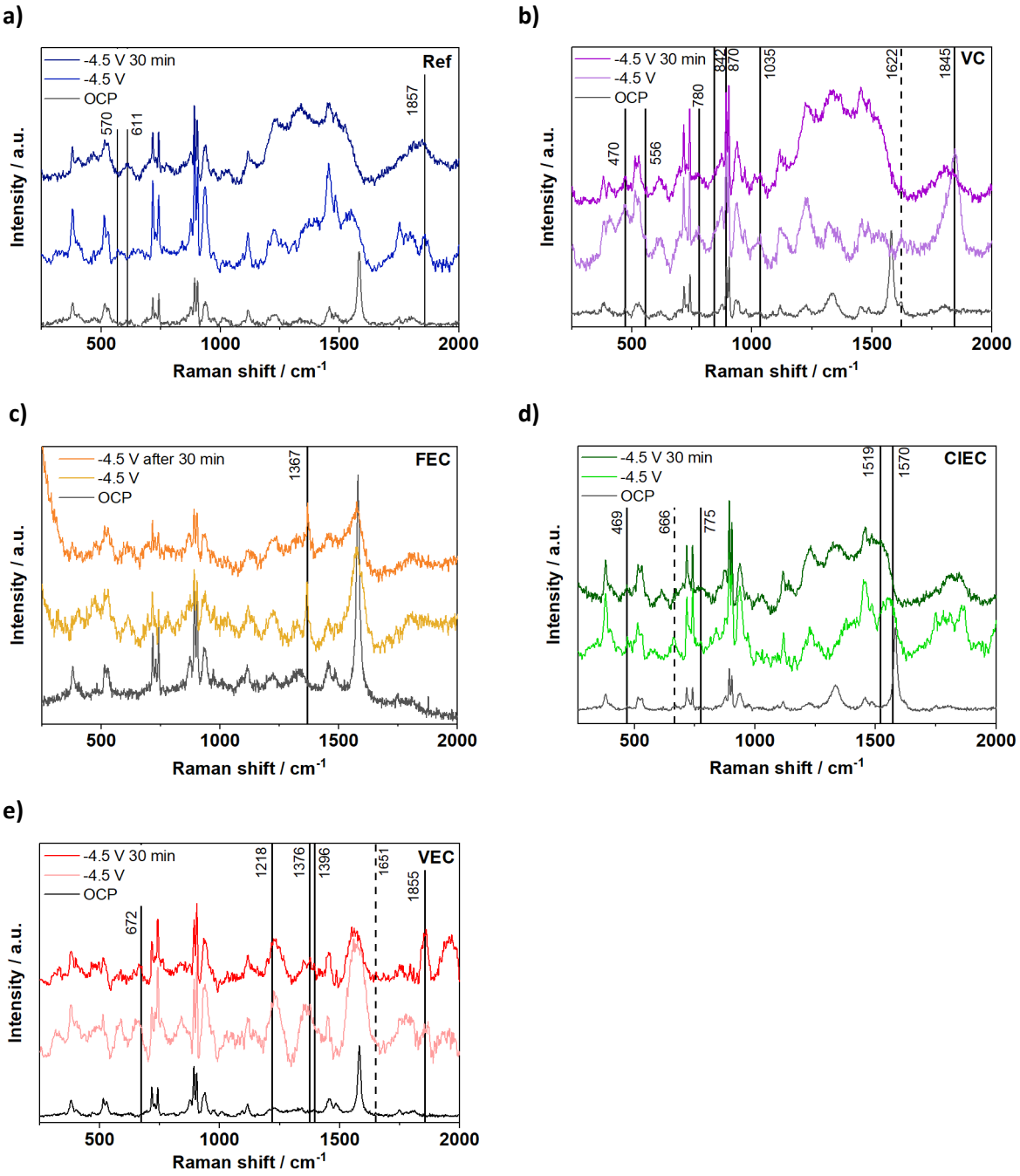

Figure 29: SHINERS spectra at OCP and -4.5 V for **a)** reference, **b)** VC, **c)** FEC, **d)** ClEC, **e)** VEC acquired with 10% laser power (wavelength reported in Fig.A10), 30 s and 5 acc., baseline subtracted and smoothed with LabSpec6.

A band around 1207 cm^{-1} can be assigned to LMC-like structures.[185] After holding the potential, an additional band around 571 cm^{-1} appears that can be assigned as well to organic carbonate species.[97] At lower potentials, a band around 565 cm^{-1} is visible at - 2.4 V that can be assigned to organic carbonates.[212] The band around 1622 cm^{-1}, already visible in the OCP spectra, can be assigned to VC double bond by comparison with the pure additive spectra, which presents an intense band in the region corresponding to double bond stretching.

For FEC (**Figure 29c**) at -4.5 V one new sharp band is visible around 1367 cm^{-1}, also after potential hold, indicating the decomposition product of FEC that could be an organic carbonate, which however, could not be further specified. At lower potential, a band around 628 cm^{-1} can be assigned to LiOH O-H stretching.[209] At -3 V additional bands around 1021 and 1400 cm^{-1}(ν C-O) can be assigned to Li_2CO_3.[97, 178]

For ClEC (**Figure 29d**) at -4.5 V bands around 1519 and 1570 cm^{-1} were observed. The first can be assigned to organic carbonates, while the second can be assigned to a decomposition product of ClEC that could not be further specified.[212] After holding the potential, bands are identified around 570, 616, 1010, 1030 and 1852 cm^{-1}. The bands around 570 and 1010 cm^{-1} were already visible at -3 V (the second already at -2.4 V) and can be assigned to lithium alkyl carbonates.[97, 212] The band around 616 cm^{-1} can be assigned to LEMC-like species[185], the band around 1030 cm^{-1} to semi-carbonate-like species (DEDOHC 2,5-dioxahexanedioic acid diethyl ester)[185] and the band around 1852 cm^{-1} to lithium carbide (Li_2C_2).[186, 209, 210] Additionally, at lower potentials a band around 630 cm^{-1} indicates the presence of LiOH.[178] Additional bands at -3 V are visible around 795 cm^{-1} , assigned to CO_2^- bending of lithium formate that can be formed in presence of CO_2, known to be formed in presence of ClEC[97,168], and around 1160 cm^{-1} that can be assigned to lithium organic carbonates.[178] A band around 666 cm^{-1} is visible in all spectra already from OCP and, comparing the spectra with the one of the pure additive (**Figure A11**), it can be assigned to the additive, probably to the C-Cl stretching.[211]

For VEC (**Figure 29e**) at -4.5 V a band around 1218 cm^{-1} that was already visible at -3 V, can be assigned to C-C stretching of alkyl carbonate species. [208] The band around 1852 cm^{-1}, visible also after potential hold, can be assigned to lithium carbide (Li_2C_2).[186, 209, 210] After potential hold, a band around 672 cm^{-1} is visible, which could indicate the presence of LiF.[178]

Bands around 1376 and 1396 cm^{-1}, already visible at -3 V can be assigned to CO_2^- bending of lithium formate and CH_2 bending of lithium alkyl carbonates.[97] At -3 V bands around 786 and 1376 cm^{-1} can be assigned to CO_2^- bending and probably asymmetric stretching of compounds as lithium formate.[97, 214] Bands around 808 (δCO_3^{2-}), 1299 (νC=O) cm^{-1} can be assigned to lithium alkyl carbonates, while bands at 1028 and 1396 (δCH_2) can be assigned to semi-carbonates.[97, 185] A broad band that can be assigned to lithium carbide is also visible, but around lower shifts (1845 cm^{-1}). A band around 1003 cm^{-1} that can be assigned to C-O bending

of alkyl carbonates is visible at -2.4 V.[97] Moreover, it was observed that the band around 1651 cm^{-1} assigned to VEC double bond stretching is shifted upon charging to 1638 cm^{-1} and increases in intensity with potential, suggesting that VEC is adsorbed on the surface. However, at -4.5 V, the band is no longer visible, indicating that VEC is no longer on the surface. Some plausible explanations are that at this potential VEC is consumed by oxidative reactions, or is no longer on the graphite surface due to the presence of EC decomposition products. For *operando* measurements, additional vibrations may be covered by electrolyte and graphite bands. Moreover, at cut-off voltage too thick SEI may be covering the nanoparticles, not allowing for enhancement of surface species from the plasmonic field.

9 CONCLUSION AND OUTLOOK

This thesis aimed to investigate ethylene derivativesas additives for NMC622||graphite cells charged to a high cut-off voltage of 4.5 V and to study their effect on the SEI. All the additives exhibited reduction potentials higher than EC, as seen from CVs and differential capacity analysis. From galvanostatic cycling, it was determined that common electrolyte additives such as FEC and VC cannot significantly improve cell performance in this cell system. ClEC can improve discharge capacity, in a compromise with cycle life and Coulombic efficiency, increasingly with higher additive concentrations. VEC has proven to be the best-performing additive in the system, with an optimum concentration of 0.3 M leading to stable long-term cycling (80% SOH at 360 cycles, 60% SOH at 1914 cycles) at 20°C and 1C. From *ΔV* analysis, VEC showed a lower resistance growth compared to the other additives. SEM images revealed a strongly modified morphology for SEI formed in the presence of VEC. However, EDX results could not give any additional information due to the similar atomic composition of the additives. Just in the case of ClEC, EDX results allowed to spot the formation of NaCl on the anode surface, indicating an interaction of the additive with the anode binder. From GC-MS and HRAM-MS, novel insights were gained on ClEC decomposition products, probably at the root of its detrimental effect on cycle-life. GC-MS also pointed out the ineffectiveness of VEC in passivating the anode during formation. From *operando* SHINERS it was possible to observe the formation of typical SEI products on the anode surface; however, still very low intensities were detected in most cases and few vibrations could be assigned for each compound. Under voltage application an blue shift of the band of VEC C=C bond was observed, and disappeared at cut-off voltage, indicating decomposition or desorption of VEC at higher voltages.

Further studies can be directed to gain a deeper understanding of the degradation products of VEC for a better comprehension of its reaction mechanism. Reductive and oxidative decomposition products can be investigated on a model SERS surface as roughened gold, to have a clearer assignment of the resulting compounds. Investigation of the CEI formation would also be important to gain additional information on the origin of performance improvement. Combination of VEC with other promising interphase modifying additives could enable even better capacity performances. Moreover, it would be interesting to investigate if VEC has any positive effect on silicon/graphite next-generation anodes.

10 BIBLIOGRAPHY

[1] Delivering the European Green Deal https://commission.europa.eu/strategy-and-policy/priorities-2019-2024/european-green-deal/delivering-european-green-deal_en (accessed Jan 11, 2023).

[2] Koohi-Fayegh, S.; Rosen, M. A. A Review of Energy Storage Types, Applications and Recent Developments. *J. Energy Storage*, **2020**, *27* (July 2019), 101047. https://doi.org/10.1016/j.est.2019.101047.

[3] Winter, M.; Brodd, R. J. What Are Batteries, Fuel Cells, and Supercapacitors? *Chem. Rev.*, **2004**, *104* (10), 4245–4269. https://doi.org/10.1021/cr020730k.

[4] Cano, Z. P.; Banham, D.; Ye, S.; Hintennach, A.; Lu, J.; Fowler, M.; Chen, Z. Batteries and Fuel Cells for Emerging Electric Vehicle Markets. *Nat. Energy*, **2018**, *3* (4), 279–289. https://doi.org/10.1038/s41560-018-0108-1.

[5] Li, M.; Lu, J.; Chen, Z.; Amine, K. 30 Years of Lithium-Ion Batteries. *Adv. Mater.*, **2018**, *30* (33), 1–24. https://doi.org/10.1002/adma.201800561.

[6] Ding, Y.; Cano, Z. P.; Yu, A.; Lu, J.; Chen, Z. Automotive Li-Ion Batteries: Current Status and Future Perspectives. *Electrochem. Energy Rev.*, **2019**, *2* (1), 1–28. https://doi.org/10.1007/s41918-018-0022-z.

[7] Atkins, D.; Capria, E.; Edström, K.; Famprikis, T.; Grimaud, A.; Jacquet, Q.; Johnson, M.; Matic, A.; Norby, P.; Reichert, H.; et al. Accelerating Battery Characterization Using Neutron and Synchrotron Techniques: Toward a Multi-Modal and Multi-Scale Standardized Experimental Workflow. *Adv. Energy Mater.*, **2022**, *12* (17). https://doi.org/10.1002/aenm.202102694.

[8] Weiling, M.; Pfeiffer, F.; Baghernejad, M. Vibrational Spectroscopy Insight into the Electrode|electrolyte Interface/Interphase in Lithium Batteries. *Adv. Energy Mater.*, **2022**, *2202504*. https://doi.org/10.1002/aenm.202202504.

[9] Jeyaseelan, C.; Jain, A.; Khurana, P.; Kumar, D. Ni-Cd Batteries. In *Recheargable batteries*; Boddula, R., Inamuddin, Pothu, R., Asiri, A. M., Eds.; 2020.

[10] Tarascon, J. M.; Armand, M. Issues and Challenges Facing Rechargeable Lithium Batteries. *Nature*, **2001**, *414*, 359–367. https://doi.org/10.1088/1751-8113/44/8/085201.

[11] Ma, J.; Li, Y.; Grundish, N. S.; Goodenough, J. B.; Chen, Y.; Guo, L.; Peng, Z.; Qi, X.; Yang, F.; Qie, L.; et al. The 2021 Battery Technology Roadmap. *J. Phys. D. Appl. Phys.*, **2021**, *54* (18). https://doi.org/10.1088/1361-6463/abd353.

[12] Xu, K. Nonaqueous Liquid Electrolytes for Lithium-Based Rechargeable Batteries. *Chem. Rev.*, **2004**, *104* (10), 4303–4417. https://doi.org/10.1021/cr030203g.

[13] Choi, J. W.; Aurbach, D. Promise and Reality of Post-Lithium-Ion Batteries with High Energy Densities. *Nat. Rev. Mater.*, **2016**, *1*. https://doi.org/10.1038/natrevmats.2016.13.

[14] Liu, B.; Zhang, J. G.; Xu, W. Advancing Lithium Metal Batteries. *Joule*, **2018**, *2* (5), 833–845. https://doi.org/10.1016/j.joule.2018.03.008.

[15] Lin, D.; Liu, Y.; Cui, Y. Reviving the Lithium Metal Anode for High-Energy Batteries. *Nat. Nanotechnol.*, **2017**, *12* (3), 194–206. https://doi.org/10.1038/nnano.2017.16.

[16] Nitta, N.; Wu, F.; Lee, J. T.; Yushin, G. Li-Ion Battery Materials: Present and Future. *Mater. Today*, **2015**, *18* (5), 252–264. https://doi.org/10.1016/j.mattod.2014.10.040.

[17] Winter, M.; Besenhard, J. O. Insertion Electrode Materials for Rechargeable Lithium Batteries. *Adv. Mater.*, **1998**, *10* (10), 725–763.

[18] Xie, L.; Tang, C.; Bi, Z.; Song, M.; Fan, Y.; Yan, C.; Li, X.; Su, F.; Zhang, Q.; Chen, C. Hard Carbon Anodes for Next-Generation Li-Ion Batteries: Review and Perspective. *Adv. Energy Mater.*, **2021**, *11* (38), 1–22. https://doi.org/10.1002/aenm.202101650.

[19] Guyomard, D.; Tarascon, J. M. Rechargeable Li1 + x Mn2 O 4 / Carbon Cells with a New Electrolyte Composition: Potentiostatic Studies and Application to Practical Cells. *J. Electrochem. Soc.*, **1993**, *140* (11), 3071–3081. https://doi.org/10.1149/1.2220987.

[20] Korthauer, R. *Lithium-Ion Batteries: Basics and Applications*; 2018. https://doi.org/10.1007/978-3-662-53071-9.

[21] Chung, D. D. L. Review: Graphite. *J. Mater. Sci.*, **2002**, *37* (8), 1475–1489. https://doi.org/10.1023/A:1014915307738.

[22] Besenhard, J. O. *Handbook of Battery Materials*; 1990.

[23] Asenbauer, J.; Eisenmann, T.; Kuenzel, M.; Kazzazi, A.; Chen, Z.; Bresser, D. The Success Story of Graphite as a Lithium-Ion Anode Material-Fundamentals, Remaining Challenges, and Recent Developments Including Silicon (Oxide) Composites. *Sustain. Energy Fuels*, **2020**, *4* (11), 5387–5416. https://doi.org/10.1039/d0se00175a.

[24] Song, X. Y.; Kinoshita, K. Microstructural Characterization of Lithiated Graphite. *J. Electrochem. Soc.*, **1996**, *143* (6), L120–L126.

[25] Uhlmann, C.; Illig, J.; Ender, M.; Schuster, R.; Ivers-Tiffée, E. In Situ Detection of Lithium Metal Plating on Graphite in Experimental Cells. *J. Power Sources*, **2015**, *279*, 428–438. https://doi.org/10.1016/j.jpowsour.2015.01.046.

[26] Ma, J.; Wang, C.; Wroblewski, S. Kinetic Characteristics of Mixed Conductive Electrodes for Lithium Ion Batteries. *J. Power Sources*, **2007**, *164* (2), 849–856. https://doi.org/10.1016/j.jpowsour.2006.11.024.

[27] Hao, Y. J.; Lai, Q. Y.; Lu, J. Z.; Wang, H. L.; Chen, Y. D.; Ji, X. Y. Synthesis and Characterization of Spinel Li4Ti5O12 Anode Material by Oxalic Acid-Assisted Sol-Gel Method. *J. Power Sources*, **2006**, *158* (2 SPEC. ISS.), 1358–1364. https://doi.org/10.1016/j.jpowsour.2005.09.063.

[28] Kanamura, K.; Umegaki, T.; Naito, H.; Takehara, Z.; Yao, T. Structural and Electrochemical Characteristics of Li4/3Ti5/3O4 as an Anode Material for Rechargeable Lithium Batteries. *J. Appl. Electrochem.*, **2001**, *31* (1), 73–78. https://doi.org/10.1023/A:1004170009354.

[29] Ohzuku, T.; Ueda, A.; Yamamoto, N. Zero-Strain Insertion Material of Li [Li1 / 3Ti5 / 3]

O 4 for Rechargeable Lithium Cells. *J. Electrochem. Soc.*, **1995**, *142* (5), 1431–1435. https://doi.org/10.1149/1.2048592.

[30] Obrovac, M. N.; Christensen, L. Structural Changes in Silicon Anodes during Lithium Insertion/Extraction. *Electrochem. Solid-State Lett.*, **2004**, *7* (5), 93–96. https://doi.org/10.1149/1.1652421.

[31] Maranchi, J. P. High Capacity, Reversible Silicon Thin Film Anodes for Lithium-Ion Batteries. *Electrochem. Solid-State Lett.*, **2003**, *6* (A198), 2004.

[32] Chevrier, V. L.; Dahn, J. R. First Principles Model of Amorphous Silicon Lithiation. *J. Electrochem. Soc.*, **2009**, *156* (6), A454. https://doi.org/10.1149/1.3111037.

[33] Lee, S. J.; Lee, J. K.; Chung, S. H.; Lee, H. Y.; Lee, S. M.; Baik, H. K. Stress Effect on Cycle Properties of the Silicon Thin-Film Anode. *J. Power Sources*, **2001**, *97–98*, 191–193. https://doi.org/10.1016/S0378-7753(01)00761-3.

[34] Luo, W.; Chen, X.; Xia, Y.; Chen, M.; Wang, L.; Wang, Q.; Li, W.; Yang, J. Surface and Interface Engineering of Silicon-Based Anode Materials for Lithium-Ion Batteries. *Adv. Energy Mater.*, **2017**, *7* (24), 1–28. https://doi.org/10.1002/aenm.201701083.

[35] Yao, Y.; McDowell, M. T.; Ryu, I.; Wu, H.; Liu, N.; Hu, L.; Nix, W. D.; Cui, Y. Interconnected Silicon Hollow Nanospheres for Lithium-Ion Battery Anodes with Long Cycle Life. *Nano Lett.*, **2011**, *11* (7), 2949–2954. https://doi.org/10.1021/nl201470j.

[36] Chan, C. K.; Peng, H.; Liu, G.; McIlwrath, K.; Zhang, X. F.; Huggins, R. A.; Cui, Y. High-Performance Lithium Battery Anodes Using Silicon Nanowires. *Nat. Nanotechnol.*, **2008**, *3* (1), 31–35. https://doi.org/10.1038/nnano.2007.411.

[37] Wu, H.; Chan, G.; Choi, J. W.; Ryu, I.; Yao, Y.; Mcdowell, M. T.; Lee, S. W.; Jackson, A.; Yang, Y.; Hu, L.; et al. Stable Cycling of Double-Walled Silicon Nanotube Battery Anodes through Solid-Electrolyte Interphase Control. *Nat. Nanotechnol.*, **2012**, *7* (5), 310–315. https://doi.org/10.1038/nnano.2012.35.

[38] Luo, F.; Liu, B.; Zheng, J.; Chu, G.; Zhong, K.; Li, H.; Huang, X.; Chen, L. Review—Nano-Silicon/Carbon Composite Anode Materials Towards Practical Application for Next Generation Li-Ion Batteries. *J. Electrochem. Soc.*, **2015**, *162* (14), A2509–A2528. https://doi.org/10.1149/2.0131514jes.

[39] He, S.; Huang, S.; Wang, S.; Mizota, I.; Liu, X.; Hou, X. Considering Critical Factors of Silicon/Graphite Anode Materials for Practical High-Energy Lithium-Ion Battery Applications. *Energy and Fuels*, **2021**, *35* (2), 944–964. https://doi.org/10.1021/acs.energyfuels.0c02948.

[40] Dalavi, S.; Guduru, P.; Lucht, B. L. Performance Enhancing Electrolyte Additives for Lithium Ion Batteries with Silicon Anodes. *J. Electrochem. Soc.*, **2012**, *159* (5), A642–A646. https://doi.org/10.1149/2.076205jes.

[41] Jin, Y.; Kneusels, N. J. H.; Marbella, L. E.; Castillo-Martínez, E.; Magusin, P. C. M. M.; Weatherup, R. S.; Jónsson, E.; Liu, T.; Paul, S.; Grey, C. P. Understanding Fluoroethylene Carbonate and Vinylene Carbonate Based Electrolytes for Si Anodes in Lithium Ion Batteries with NMR Spectroscopy. *J. Am. Chem. Soc.*, **2018**, *140* (31), 9854–9867. https://doi.org/10.1021/jacs.8b03408.

[42] Whittingham, M. S. Lithium Batteries and Cathode Materials. *Chem. Rev.*, **2004**, *104* (10), 4271–4301. https://doi.org/10.1021/cr020731c.

[43] Liu, W.; Oh, P.; Liu, X.; Lee, M. J.; Cho, W.; Chae, S.; Kim, Y.; Cho, J. Nickel-Rich Layered Lithium Transition-Metal Oxide for High-Energy Lithium-Ion Batteries. *Angew. Chemie - Int. Ed.*, **2015**, *54* (15), 4440–4457. https://doi.org/10.1002/anie.201409262.

[44] Zaghib, K.; Guerfi, A.; Hovington, P.; Vijh, A.; Trudeau, M.; Mauger, A.; Goodenough, J. B.; Julien, C. M. Review and Analysis of Nanostructured Olivine-Based Lithium Recheargeable Batteries: Status and Trends. *J. Power Sources*, **2013**, *232*, 357–369. https://doi.org/10.1016/j.jpowsour.2012.12.095.

[45] Piana, M.; Arrabito, M.; Bodoardo, S.; D'Epifanio, A.; Satolli, D.; Croce, F.; Scrosati, B. Characterization of Phospho-Olivines as Materials for Li-Ion Cell Cathodes. *Ionics (Kiel).*, **2002**, *8* (1–2), 17–26. https://doi.org/10.1007/BF02377749.

[46] Wang, Y.; Liu, Z.; Zhou, S. An Effective Method for Preparing Uniform Carbon Coated Nano-Sized LiFePO4 Particles. *Electrochim. Acta*, **2011**, *58* (1), 359–363. https://doi.org/10.1016/j.electacta.2011.09.053.

[47] Örnek, A.; Bulut, E.; Can, M. Influence of Gradual Cobalt Substitution on Lithium Nickel Phosphate Nano-Scale Composites for High Voltage Applications. *Mater. Charact.*, **2015**, *106*, 152–162. https://doi.org/10.1016/j.matchar.2015.05.029.

[48] Guo, H.; Wu, C.; Liao, L.; Xie, J.; Zhang, S.; Zhu, P.; Cao, G.; Zhao, X. Performance Improvement of Lithium Manganese Phosphate by Controllable Morphology Tailoring with Acid-Engaged Nano Engineering. *Inorg. Chem.*, **2015**, *54* (2), 667–674. https://doi.org/10.1021/ic5026075.

[49] Lee, S.; Manthiram, A. Can Cobalt Be Eliminated from Lithium-Ion Batteries? *ACS Energy Lett.*, **2022**, *7* (9), 3058–3063. https://doi.org/10.1021/acsenergylett.2c01553.

[50] Lim, B. B.; Myung, S. T.; Yoon, C. S.; Sun, Y. K. Comparative Study of Ni-Rich Layered Cathodes for Rechargeable Lithium Batteries: Li[Ni0.85Co0.11Al0.04]O2 and Li[Ni0.84Co0.06Mn0.09Al0.01]O2 with Two-Step Full Concentration Gradients. *ACS Energy Lett.*, **2016**, *1* (1), 283–289. https://doi.org/10.1021/ACSENERGYLETT.6B00150/SUPPL_FILE/NZ6B00150_SI_001.PDF.

[51] Xu, J.; Hu, E.; Nordlund, D.; Mehta, A.; Ehrlich, S. N.; Yang, X. Q.; Tong, W. Understanding the Degradation Mechanism of Lithium Nickel Oxide Cathodes for Li-Ion Batteries. *ACS Appl. Mater. Interfaces*, **2016**, *8* (46), 31677–31683. https://doi.org/10.1021/acsami.6b11111.

[52] T. Ohzuku, A. Ueda, M. Nagayama, Y. Iwahoshi, H. K. Comparative Study of LiCoO2 , LiNi1/2Co1/2O2 AND LiNiO2 for 4 Volt Secondary Lithium Cells. *Electrochim. Acta*, **1993**, *38* (9), 1159–1167.

[53] Chen, H.; Dawson, J. A.; Harding, J. H. Effects of Cationic Substitution on Structural Defects in Layered Cathode Materials LiNiO2. *J. Mater. Chem. A*, **2014**, *2* (21), 7988–7996. https://doi.org/10.1039/c4ta00637b.

[54] Liang, G.; Peterson, V. K.; See, K. W.; Guo, Z.; Pang, W. K. Developing High-Voltage

Spinel LiNi0.5Mn1.5O4cathodes for High-Energy-Density Lithium-Ion Batteries: Current Achievements and Future Prospects. *J. Mater. Chem. A*, **2020**, *8* (31), 15373–15398. https://doi.org/10.1039/d0ta02812f.

[55] Thackeray, M. M. Spinel Electrodes for Lithium Batteries. *J. Am. Ceram. Soc.*, **1999**, *82* (12), 3347–3354. https://doi.org/10.1111/j.1151-2916.1999.tb02250.x.

[56] Jang, D. H.; Shin, Y. J.; Oh, S. M. Dissolution of Spinel Oxides and Capacity Losses in 4 V Li / Li x Mn2 O 4 Cells. *J. Electrochem. Soc.*, **1996**, *143* (7), 2204–2211. https://doi.org/10.1149/1.1836981.

[57] Xu, K. Electrolytes and Interphases in Li-Ion Batteries and Beyond. *Chem. Rev.*, **2014**, *114* (23), 11503–11618. https://doi.org/10.1021/cr500003w.

[58] Xu, K.; Von Cresce, A. Interfacing Electrolytes with Electrodes in Li Ion Batteries. *J. Mater. Chem.*, **2011**, *21* (27), 9849–9864. https://doi.org/10.1039/c0jm04309e.

[59] Fong, R.; Von Sacken, U.; Dahn, J. R. Studies of Lithium Intercalation into Carbons Using Nonaqueous Electrochemical Cells. *J. Electrochem. Soc.*, **1990**, *137* (7), 2009–2013.

[60] Kalhoff, J.; Eshetu, G. G.; Bresser, D.; Passerini, S. Safer Electrolytes for Lithium-Ion Batteries: State of the Art and Perspectives. *ChemSusChem*, **2015**, *8* (13), 2154–2175. https://doi.org/10.1002/cssc.201500284.

[61] Xu, K.; Ding, M. S.; Zhang, S.; Allen, J. L.; Jow, T. R. Evaluation of Fluorinated Alkyl Phosphates as Flame Retardants in Electrolytes for Li-Ion Batteries: I. Physical and Electrochemical Properties. *J. Electrochem. Soc.*, **2003**, *150* (2), A161. https://doi.org/10.1149/1.1533040.

[62] Chen, J.; Buhrmester, C.; Dahn, J. R. Chemical Overcharge and Overdischarge Protection for Lithium-Ion Batteries. *Electrochem. Solid-State Lett.*, **2005**, *8* (1), 2–6. https://doi.org/10.1149/1.1836119.

[63] Shima, K.; Shizuka, K.; Ue, M.; Ota, H.; Hatozaki, T.; Yamaki, J. I. Reaction Mechanisms of Aromatic Compounds as an Overcharge Protection Agent for 4 V Class Lithium-Ion Cells. *J. Power Sources*, **2006**, *161* (2), 1264–1274. https://doi.org/10.1016/j.jpowsour.2006.05.029.

[64] Zhang, S. S. A Review on Electrolyte Additives for Lithium-Ion Batteries. *J. Power Sources*, **2006**, *162* (2 SPEC. ISS.), 1379–1394. https://doi.org/10.1016/j.jpowsour.2006.07.074.

[65] Zheng, J.; Xiao, J.; Gu, M.; Zuo, P.; Wang, C.; Zhang, J. G. Interface Modifications by Anion Receptors for High Energy Lithium Ion Batteries. *J. Power Sources*, **2014**, *250*, 313–318. https://doi.org/10.1016/j.jpowsour.2013.10.071.

[66] Shin, J. S.; Han, C. H.; Jung, U. H.; Lee, S. I.; Kim, H. J.; Kim, K. Effect of Li2CO3 Additive on Gas Generation in Lithium-Ion Batteries. *J. Power Sources*, **2002**, *109* (1), 47–52. https://doi.org/10.1016/S0378-7753(02)00039-3.

[67] Choi, Y. K.; Chung, K. Il; Kim, W. S.; Sung, Y. E.; Park, S. M. Suppressive Effect of Li2CO3 on Initial Irreversibility at Carbon Anode in Li-Ion Batteries. *J. Power Sources*, **2002**, *104* (1), 132–139. https://doi.org/10.1016/S0378-7753(01)00911-9.

[68] Aurbach, D.; Ein-Eli, Y.; Chusid (Youngman), O.; Carmeli, Y.; Babai, M.; Yamin, H. The Correlation Between the Surface Chemistry and the Performance of Li-Carbon Intercalation Anodes for Rechargeable 'Rocking-Chair' Type Batteries. *J. Electrochem. Soc.*, **1994**, *141* (3), 603–611. https://doi.org/10.1149/1.2054777.

[69] Hopkins, E. J.; Frisco, S.; Pekarek, R. T.; Stetson, C.; Huey, Z.; Harvey, S.; Li, X.; Key, B.; Fang, C.; Liu, G.; et al. Examining CO 2 as an Additive for Solid Electrolyte Interphase Formation on Silicon Anodes . *J. Electrochem. Soc.*, **2021**, *168* (3), 030534. https://doi.org/10.1149/1945-7111/abec66.

[70] Lee, J.-T.; Wu, M.-S.; Wang, F.-M.; Lin, Y.-W.; Bai, M.-Y.; Chiang, P.-C. J. Effects of Aromatic Esters as Propylene Carbonate-Based Electrolyte Additives in Lithium-Ion Batteries. *J. Electrochem. Soc.*, **2005**, *152* (9), A1837. https://doi.org/10.1149/1.1993407.

[71] Schroeder, G.; Gierczyk, B.; Waszak, D.; Walkowiak, M. Impact of Ethyl Tris-2-Methoxyethoxy Silane on the Passivation of Graphite Electrode in Li-Ion Cells with PC-Based Electrolyte. *Electrochem. commun.*, **2006**, *8* (10), 1583–1587. https://doi.org/10.1016/j.elecom.2006.07.030.

[72] Zhao, H.; Yu, X.; Li, J.; Li, B.; Shao, H.; Li, L.; Deng, Y. Film-Forming Electrolyte Additives for Rechargeable Lithium-Ion Batteries: Progress and Outlook. *J. Mater. Chem. A*, **2019**, *7* (15), 8700–8722. https://doi.org/10.1039/c9ta00126c.

[73] Korepp, C.; Kern, W.; Lanzer, E. A.; Raimann, P. R.; Besenhard, J. O.; Yang, M. H.; Möller, K. C.; Shieh, D. T.; Winter, M. Isocyanate Compounds as Electrolyte Additives for Lithium-Ion Batteries. *J. Power Sources*, **2007**, *174* (2), 387–393. https://doi.org/10.1016/j.jpowsour.2007.06.141.

[74] Sano, A.; Maruyama, S. Decreasing the Initial Irreversible Capacity Loss by Addition of Cyclic Sulfate as Electrolyte Additives. *J. Power Sources*, **2009**, *192* (2), 714–718. https://doi.org/10.1016/j.jpowsour.2009.02.075.

[75] Ota, H.; Sakata, Y.; Inoue, A.; Yamaguchi, S. Analysis of Vinylene Carbonate Derived SEI Layers on Graphite Anode. *J. Electrochem. Soc.*, **2004**, *151* (10), A1659. https://doi.org/10.1149/1.1785795.

[76] Pfeiffer, F.; Diddens, D.; Weiling, M.; Baghernejad, M. Study of a High-Voltage NMC Interphase in the Presence of a Thiophene Additive Realized by Operando SHINERS. *ACS Appl. Mater. Interfaces*, **2023**. https://doi.org/10.1021/acsami.2c17958.

[77] Ferrara, C.; Ruffo, R.; Mustarelli, P. The Importance of Interphases in Energy Storage Devices: Methods and Strategies to Investigate and Control Interfacial Processes. *Physchem*, **2021**, *1* (1), 26–44. https://doi.org/10.3390/physchem1010003.

[78] Edström, K.; Gustafsson, T.; Thomas, J. O. The Cathode-Electrolyte Interface in the Li-Ion Battery. *Electrochim. Acta*, **2004**, *50* (2-3 SPEC. ISS.), 397–403. https://doi.org/10.1016/j.electacta.2004.03.049.

[79] Peled, E. The Electrochemical Behavior of Alkali and Alkaline Earth Metals in Nonaqueous Battery Systems—The Solid Electrolyte Interphase Model. *J. Electrochem. Soc.*, **1979**, *126* (12), 2047–2051. https://doi.org/10.1149/1.2128859.

[80] Fong, R.; von Sacken, U.; Dahn, J. R. Studies of Lithium Intercalation into Carbons Using Nonaqueous Electrochemical Cells. *J. Electrochem. Soc.*, **1990**, *137* (7), 2009–2013. https://doi.org/10.1149/1.2086855.

[81] Wang, C.; Appleby, A. J.; Little, F. E. Charge-Discharge Stability of Graphite Anodes for Lithium-Ion Batteries. *J. Electroanal. Chem.*, **2001**, *497* (1–2), 33–46. https://doi.org/10.1016/S0022-0728(00)00447-2.

[82] Li, J.; Murphy, E.; Winnick, J.; Kohl, P. A. Studies on the Cycle Life of Commercial Lithium Ion Batteries during Rapid Charge-Discharge Cycling. *J. Power Sources*, **2001**, *102* (1–2), 294–301. https://doi.org/10.1016/S0378-7753(01)00821-7.

[83] Wang, C.; Zhang, X. W.; Appleby, A. J.; Chen, X.; Little, F. E. Self-Discharge of Secondary Lithium-Ion Graphite Anodes. *J. Power Sources*, **2002**, *112* (1), 98–104. https://doi.org/10.1016/S0378-7753(02)00359-2.

[84] Peled, E.; Menkin, S. Review—SEI: Past, Present and Future. *J. Electrochem. Soc.*, **2017**, *164* (7), A1703–A1719. https://doi.org/10.1149/2.1441707jes.

[85] Winter, M. The Solid Electrolyte Interphase - The Most Important and the Least Understood Solid Electrolyte in Rechargeable Li Batteries. *Zeitschrift fur Phys. Chemie*, **2009**, *223* (10–11), 1395–1406. https://doi.org/10.1524/zpch.2009.6086.

[86] Heiskanen, S. K.; Kim, J.; Lucht, B. L. Generation and Evolution of the Solid Electrolyte Interphase of Lithium-Ion Batteries. *Joule*, **2019**, *3* (10), 2322–2333. https://doi.org/10.1016/j.joule.2019.08.018.

[87] Gauthier, M.; Carney, T. J.; Grimaud, A.; Giordano, L.; Pour, N.; Chang, H. H.; Fenning, D. P.; Lux, S. F.; Paschos, O.; Bauer, C.; et al. Electrode-Electrolyte Interface in Li-Ion Batteries: Current Understanding and New Insights. *J. Phys. Chem. Lett.*, **2015**, *6* (22), 4653–4672. https://doi.org/10.1021/acs.jpclett.5b01727.

[88] Peled, E. Film Forming Reaction at the Lithium/Electrolyte Interface. *J. Power Sources*, **1983**, *9* (3), 253–266. https://doi.org/10.1016/0378-7753(83)87026-8.

[89] Besenhard, J. O.; Winter, M.; Yang, J.; Biberacher, W. Filming Mechanism of Lithium-Carbon Anodes in Organic and Inorganic Electrolytes. *J. Power Sources*, **1995**, *54* (2), 228–231. https://doi.org/10.1016/0378-7753(94)02073-C.

[90] Ein-Eli, Y. New Perspective on the Foundation and Structure of the Solid Electrolyte Interface at the Graphite Anode of Li-Ion Cells. *Electrochem. Solid-State Lett.*, **1999**, *2* (5), 212–214. https://doi.org/10.1149/1.1390787.

[91] Peled, E.; Golodnitsky, D.; Ardel, G. Advanced Model for Solid Electrolyte Interphase Electrodes in Liquid and Polymer Electrolytes. *J. Electrochem. Soc.*, **1997**, *144* (8), L208–L210. https://doi.org/10.1149/1.1837858.

[92] Shi, S.; Lu, P.; Liu, Z.; Qi, Y.; Hector, L. G.; Li, H.; Harris, S. J. Direct Calculation of Li-Ion Transport in the Solid Electrolyte Interphase. *J. Am. Chem. Soc.*, **2012**, *134* (37), 15476–15487. https://doi.org/10.1021/ja305366r.

[93] Kranz, T.; Kranz, S.; Miß, V.; Schepp, J.; Roling, B. Interrelation between Redox Molecule Transport and Li + Ion Transport across a Model Solid Electrolyte Interphase Grown on a Glassy Carbon Electrode . *J. Electrochem. Soc.*, **2017**, *164* (14), A3777–

A3784. https://doi.org/10.1149/2.1171714jes.

[94] Bar-Tow, D.; Peled, E.; Burstein, L. A Study of Highly Oriented Pyrolytic Graphite as a Model for the Graphite Anode in Li-Ion Batteries. *J. Electrochem. Soc.*, **1999**, *146* (3), 824–832. https://doi.org/10.1149/1.1391688.

[95] Peled, E.; Bar Tow, D.; Merson, A.; Gladkich, A.; Burstein, L.; Golodnitsky, D. Composition, Depth Profiles and Lateral Distribution of Materials in the SEI Built on HOPG-TOF SIMS and XPS Studies. *J. Power Sources*, **2001**, *97–98*, 52–57. https://doi.org/10.1016/S0378-7753(01)00505-5.

[96] Peled, E.; Tow, D. B.; Merson, A.; Burstein, L. Microphase Structure of SEI on HOPG. *J. New Mater. Electrochem. Syst.*, **2000**, *3* (4), 319–326.

[97] Verma, P.; Maire, P.; Novák, P. A Review of the Features and Analyses of the Solid Electrolyte Interphase in Li-Ion Batteries. *Electrochim. Acta*, **2010**, *55* (22), 6332–6341. https://doi.org/10.1016/j.electacta.2010.05.072.

[98] Shkrob, I. A.; Zhu, Y.; Marin, T. W.; Abraham, D. Reduction of Carbonate Electrolytes and the Formation of Solid-Electrolyte Interface (SEI) in Lithium-Ion Batteries. 1. Spectroscopic Observations of Radical Intermediates Generated in One-Electron Reduction of Carbonates. *J. Phys. Chem. C*, **2013**, *117* (38), 19255–19269. https://doi.org/10.1021/jp406274e.

[99] Shkrob, I. A.; Zhu, Y.; Marin, T. W.; Abraham, D. Reduction of Carbonate Electrolytes and the Formation of Solid-Electrolyte Interface (SEI) in Lithium-Ion Batteries. 2. Radiolytically Induced Polymerization of Ethylene Carbonate. *J. Phys. Chem. C*, **2013**, *117* (38), 19270–19279. https://doi.org/10.1021/jp406274e.

[100] Onuki, M.; Sakata, Y.; Yanagidate, M.; Otake, Y.; Kinoshita, S.; Ue, M.; Deguchi, M. Identification of the Source of Evolved Gas in Li-Ion Batteries by Using 13C-Labeled Solvents. *ECS Meet. Abstr.*, **2007**, *MA2007-02* (4), 219–219. https://doi.org/10.1149/ma2007-02/4/219.

[101] Parimalam, B. S.; Lucht, B. L. Reduction Reactions of Electrolyte Salts for Lithium Ion Batteries: LiPF 6 , LiBF 4 , LiDFOB, LiBOB, and LiTFSI . *J. Electrochem. Soc.*, **2018**, *165* (2), A251–A255. https://doi.org/10.1149/2.0901802jes.

[102] Parimalam, B. S.; MacIntosh, A. D.; Kadam, R.; Lucht, B. L. Decomposition Reactions of Anode Solid Electrolyte Interphase (SEI) Components with LiPF6. *J. Phys. Chem. C*, **2017**, *121* (41), 22733–22738. https://doi.org/10.1021/acs.jpcc.7b08433.

[103] Kim, K.; Ma, H.; Park, S.; Choi, N. S. Electrolyte-Additive-Driven Interfacial Engineering for High-Capacity Electrodes in Lithium-Ion Batteries: Promise and Challenges. *ACS Energy Lett.*, **2020**, *5* (5), 1537–1553. https://doi.org/10.1021/acsenergylett.0c00468.

[104] Freiberg, A. T. S.; Sicklinger, J.; Solchenbach, S.; Gasteiger, H. A. Li2CO3 Decomposition in Li-Ion Batteries Induced by the Electrochemical Oxidation of the Electrolyte and of Electrolyte Impurities. *Electrochim. Acta*, **2020**, *346*, 136271. https://doi.org/10.1016/j.electacta.2020.136271.

[105] Andersson, A. M.; Abraham, D. P.; Haasch, R.; MacLaren, S.; Liu, J.; Amine, K. Surface Characterization of Electrodes from High Power Lithium-Ion Batteries. *J. Electrochem.*

Soc., **2002**, *149* (10), A1358. https://doi.org/10.1149/1.1505636.

[106] Jung, R.; Metzger, M.; Maglia, F.; Stinner, C.; Gasteiger, H. A. Chemical versus Electrochemical Electrolyte Oxidation on NMC111, NMC622, NMC811, LNMO, and Conductive Carbon. *J. Phys. Chem. Lett.*, **2017**, *8* (19), 4820–4825. https://doi.org/10.1021/acs.jpclett.7b01927.

[107] Malmgren, S.; Ciosek, K.; Hahlin, M.; Gustafsson, T.; Gorgoi, M.; Rensmo, H.; Edström, K. Comparing Anode and Cathode Electrode/Electrolyte Interface Composition and Morphology Using Soft and Hard X-Ray Photoelectron Spectroscopy. *Electrochim. Acta*, **2013**, *97*, 23–32. https://doi.org/10.1016/j.electacta.2013.03.010.

[108] Fang, S.; Jackson, D.; Dreibelbis, M. L.; Kuech, T. F.; Hamers, R. J. Anode-Originated SEI Migration Contributes to Formation of Cathode-Electrolyte Interphase Layer. *J. Power Sources*, **2018**, *373*, 184–192. https://doi.org/10.1016/j.jpowsour.2017.09.050.

[109] Kim, J. H.; Pieczonka, N. P. W.; Yang, L. Challenges and Approaches for High-Voltage Spinel Lithium-Ion Batteries. *ChemPhysChem*, **2014**, *15* (10), 1940–1954. https://doi.org/10.1002/cphc.201400052.

[110] Armand, M.; Axmann, P.; Bresser, D.; Copley, M.; Edström, K.; Ekberg, C.; Guyomard, D.; Lestriez, B.; Novák, P.; Petranikova, M.; et al. Lithium-Ion Batteries – Current State of the Art and Anticipated Developments. *J. Power Sources*, **2020**, *479* (July). https://doi.org/10.1016/j.jpowsour.2020.228708.

[111] Petibon, R.; Xia, J.; Ma, L.; Bauer, M. K. G.; Nelson, K. J.; Dahn, J. R. Electrolyte System for High Voltage Li-Ion Cells. *J. Electrochem. Soc.*, **2016**, *163* (13), A2571–A2578. https://doi.org/10.1149/2.0321613jes.

[112] Laszczynski, N.; Solchenbach, S.; Gasteiger, H. A.; Lucht, B. L. Understanding Electrolyte Decomposition of Graphite/NCM811 Cells at Elevated Operating Voltage. *J. Electrochem. Soc.*, **2019**, *166* (10), A1853–A1859. https://doi.org/10.1149/2.0571910jes.

[113] Klein, S.; Bärmann, P.; Beuse, T.; Borzutzki, K.; Frerichs, J. E.; Kasnatscheew, J.; Winter, M.; Placke, T. Exploiting the Degradation Mechanism of NCM523‖ Graphite Lithium-Ion Full Cells Operated at High Voltage. *ChemSusChem*, **2021**, *14* (2), 595–613. https://doi.org/10.1002/cssc.202002113.

[114] Zhang, S.; Ma, J.; Hu, Z.; Cui, G.; Chen, L. Identifying and Addressing Critical Challenges of High-Voltage Layered Ternary Oxide Cathode Materials. *Chem. Mater.*, **2019**, *31* (16), 6033–6065. https://doi.org/10.1021/acs.chemmater.9b01557.

[115] De Biasi, L.; Kondrakov, A. O.; Geßwein, H.; Brezesinski, T.; Hartmann, P.; Janek, J. Between Scylla and Charybdis: Balancing among Structural Stability and Energy Density of Layered NCM Cathode Materials for Advanced Lithium-Ion Batteries. *J. Phys. Chem. C*, **2017**, *121* (47), 26163–26171. https://doi.org/10.1021/acs.jpcc.7b06363.

[116] Jung, R.; Soc, J. E.; Jung, R.; Metzger, M.; Maglia, F.; Stinner, C. Oxygen Release and Its Effect on the Cycling Stability of LiNi x Mn y Co z O 2 (NMC) Cathode Materials for Li-Ion Batteries Oxygen Release and Its Effect on the Cycling Stability of LiNi x Mn y Co z O 2 (NMC) Cathode Materials for Li-Ion Batteries. **2017**, *2*.

https://doi.org/10.1149/2.0021707jes.

[117] Kim, N. Y.; Yim, T.; Song, J. H.; Yu, J. S.; Lee, Z. Microstructural Study on Degradation Mechanism of Layered LiNi0.6Co0.2Mn0.2O2 Cathode Materials by Analytical Transmission Electron Microscopy. *J. Power Sources*, **2016**, *307*, 641–648. https://doi.org/10.1016/j.jpowsour.2016.01.023.

[118] Jung, S. K.; Gwon, H.; Hong, J.; Park, K. Y.; Seo, D. H.; Kim, H.; Hyun, J.; Yang, W.; Kang, K. Understanding the Degradation Mechanisms of LiNi0.5Co 0.2Mn0.3O2 Cathode Material in Lithium Ion Batteries. *Adv. Energy Mater.*, **2014**, *4* (1), 1–7. https://doi.org/10.1002/aenm.201300787.

[119] Hatsukade, T.; Schiele, A.; Hartmann, P.; Brezesinski, T.; Janek, J. Origin of Carbon Dioxide Evolved during Cycling of Nickel-Rich Layered NCM Cathodes. *ACS Appl. Mater. Interfaces*, **2018**, *10* (45), 38892–38899. https://doi.org/10.1021/acsami.8b13158.

[120] Jung, R.; Linsenmann, F.; Thomas, R.; Wandt, J.; Solchenbach, S.; Maglia, F.; Stinner, C.; Tromp, M.; Gasteiger, H. A. Nickel, Manganese, and Cobalt Dissolution from Ni-Rich NMC and Their Effects on NMC622-Graphite Cells. *J. Electrochem. Soc.*, **2019**, *166* (2), A378–A389. https://doi.org/10.1149/2.1151902jes.

[121] Sahore, R.; O'Hanlon, D. C.; Tornheim, A.; Lee, C.-W.; Garcia, J. C.; Iddir, H.; Balasubramanian, M.; Bloom, I. Revisiting the Mechanism Behind Transition-Metal Dissolution from Delithiated LiNi x Mn y Co z O 2 (NMC) Cathodes . *J. Electrochem. Soc.*, **2020**, *167* (2), 020513. https://doi.org/10.1149/1945-7111/ab6826.

[122] Börner, M.; Horsthemke, F.; Kollmer, F.; Haseloff, S.; Friesen, A.; Niehoff, P.; Nowak, S.; Winter, M.; Schappacher, F. M. Degradation Effects on the Surface of Commercial LiNi0.5Co0.2Mn0.3O2 Electrodes. *J. Power Sources*, **2016**, *335*, 45–55. https://doi.org/10.1016/j.jpowsour.2016.09.071.

[123] Evertz, M.; Horsthemke, F.; Kasnatscheew, J.; Börner, M.; Winter, M.; Nowak, S. Unraveling Transition Metal Dissolution of Li1.04Ni1/3Co1/3Mn1/3O2 (NCM 111) in Lithium Ion Full Cells by Using the Total Reflection X-Ray Fluorescence Technique. *J. Power Sources*, **2016**, *329*, 364–371. https://doi.org/10.1016/j.jpowsour.2016.08.099.

[124] Amine, K.; Liu, J.; Kang, S.; Belharouak, I.; Hyung, Y.; Vissers, D.; Henriksen, G. Improved Lithium Manganese Oxide Spinel/Graphite Li-Ion Cells for High-Power Applications. *J. Power Sources*, **2004**, *129* (1 SPEC. ISS.), 14–19. https://doi.org/10.1016/j.jpowsour.2003.11.007.

[125] Zhan, C.; Lu, J.; Jeremy Kropf, A.; Wu, T.; Jansen, A. N.; Sun, Y. K.; Qiu, X.; Amine, K. Mn(II) Deposition on Anodes and Its Effects on Capacity Fade in Spinel Lithium Manganate-Carbon Systems. *Nat. Commun.*, **2013**, *4* (Ii), 1–8. https://doi.org/10.1038/ncomms3437.

[126] Gilbert, J. A.; Shkrob, I. A.; Abraham, D. P. Transition Metal Dissolution, Ion Migration, Electrocatalytic Reduction and Capacity Loss in Lithium-Ion Full Cells. *J. Electrochem. Soc.*, **2017**, *164* (2), A389–A399. https://doi.org/10.1149/2.1111702jes.

[127] Yan, P.; Zheng, J.; Gu, M.; Xiao, J.; Zhang, J. G.; Wang, C. M. Intragranular Cracking as a Critical Barrier for High-Voltage Usage of Layer-Structured Cathode for Lithium-Ion

Batteries. *Nat. Commun.*, **2017**, *8*, 1–9. https://doi.org/10.1038/ncomms14101.

[128] Klein, S.; Bärmann, P.; Fromm, O.; Borzutzki, K.; Reiter, J.; Fan, Q.; Winter, M.; Placke, T.; Kasnatscheew, J. Prospects and Limitations of Single-Crystal Cathode Materials to Overcome Cross-Talk Phenomena in High-Voltage Lithium Ion Cells. *J. Mater. Chem. A*, **2021**, *9* (12), 7546–7555. https://doi.org/10.1039/d0ta11775g.

[129] Oswald, S.; Bock, M.; Gasteiger, H. A. Elucidating the Implications of Morphology on Fundamental Characteristics of Nickel-Rich NCMs: Cracking, Gassing, Rate Capability, and Thermal Stability of Poly- and Single-Crystalline NCM622. *J. Electrochem. Soc.*, **2022**, *169* (5), 050501. https://doi.org/10.1149/1945-7111/ac5f7f.

[130] Sun, Y. K.; Myung, S. T.; Park, B. C.; Prakash, J.; Belharouak, I.; Amine, K. High-Energy Cathode Material for Long-Life and Safe Lithium Batteries. *Nat. Mater.*, **2009**, *8* (4), 320–324. https://doi.org/10.1038/nmat2418.

[131] Huang, Z.; Wang, Z.; Zheng, X.; Guo, H.; Li, X.; Jing, Q.; Yang, Z. Effect of Mg Doping on the Structural and Electrochemical Performance of LiNi0.6Co0.2Mn0.2O2 Cathode Materials. *Electrochim. Acta*, **2015**, *182*, 795–802. https://doi.org/10.1016/j.electacta.2015.09.151.

[132] Chen, M.; Zhao, E.; Chen, D.; Wu, M.; Han, S.; Huang, Q.; Yang, L.; Xiao, X.; Hu, Z. Decreasing Li/Ni Disorder and Improving the Electrochemical Performances of Ni-Rich LiNi0.8Co0.1Mn0.1O2 by Ca Doping. *Inorg. Chem.*, **2017**, *56* (14), 8355–8362. https://doi.org/10.1021/acs.inorgchem.7b01035.

[133] Bai, Y.; Wang, X.; Yang, S.; Zhang, X.; Yang, X.; Shu, H.; Wu, Q. The Effects of FePO 4-Coating on High-Voltage Cycling Stability and Rate Capability of Li[Ni 0.5Co 0.2Mn 0.3] O 2. *J. Alloys Compd.*, **2012**, *541* (3), 125–131. https://doi.org/10.1016/j.jallcom.2012.06.101.

[134] Kang, J.; Pham, H. Q.; Kang, D. H.; Park, H. Y.; Song, S. W. Improved Rate Capability of Highly Loaded Carbon Fiber-Interwoven LiNi0.6Co0.2Mn0.2O2 Cathode Material for High-Power Li-Ion Batteries. *J. Alloys Compd.*, **2016**, *657*, 464–471. https://doi.org/10.1016/j.jallcom.2015.10.127.

[135] Qian, Y.; Kang, Y.; Hu, S.; Shi, Q.; Chen, Q.; Tang, X.; Xiao, Y.; Zhao, H.; Luo, G.; Xu, K.; et al. Mechanism Study of Unsaturated Tripropargyl Phosphate as an Efficient Electrolyte Additive Forming Multifunctional Interphases in Lithium Ion and Lithium Metal Batteries. *ACS Appl. Mater. Interfaces*, **2020**, *12* (9), 10443–10451. https://doi.org/10.1021/acsami.9b21605.

[136] Aurbach, D.; Gamolsky, K.; Markovsky, B.; Gofer, Y.; Schmidt, M.; Heider, U. On the Use of Vinylene Carbonate (VC) as an Additive to Electrolyte Solutions for Li-Ion Batteries. *Electrochim. Acta*, **2002**, *47* (9), 1423–1439. https://doi.org/10.1016/S0013-4686(01)00858-1.

[137] Wang, Y.; Nakamura, S.; Tasaki, K.; Balbuena, P. B. Theoretical Studies to Understand Surface Chemistry on Carbon Anodes for Lithium-Ion Batteries: How Does Vinylene Carbonate Play Its Role as an Electrolyte Additive? *J. Am. Chem. Soc.*, **2002**, *124* (16), 4408–4421. https://doi.org/10.1021/ja017073i.

[138] El Ouatani, L.; Dedryvère, R.; Siret, C.; Biensan, P.; Reynaud, S.; Iratçabal, P.; Gonbeau,

D. The Effect of Vinylene Carbonate Additive on Surface Film Formation on Both Electrodes in Li-Ion Batteries. *J. Electrochem. Soc.*, **2009**, *156* (2), A103. https://doi.org/10.1149/1.3029674.

[139] Michan, A. L.; Parimalam, B. S.; Leskes, M.; Kerber, R. N.; Yoon, T.; Grey, C. P.; Lucht, B. L. Fluoroethylene Carbonate and Vinylene Carbonate Reduction: Understanding Lithium-Ion Battery Electrolyte Additives and Solid Electrolyte Interphase Formation. *Chem. Mater.*, **2016**, *28* (22), 8149–8159. https://doi.org/10.1021/acs.chemmater.6b02282.

[140] Grugeon, S.; Jankowski, P.; Cailleu, D.; Forestier, C.; Sannier, L.; Armand, M.; Johansson, P.; Laruelle, S. Towards a Better Understanding of Vinylene Carbonate Derived SEI-Layers by Synthesis of Reduction Compounds. *J. Power Sources*, **2019**, *427* (April), 77–84. https://doi.org/10.1016/j.jpowsour.2019.04.061.

[141] Wang, D. Y.; Sinha, N. N.; Burns, J. C.; Aiken, C. P.; Petibon, R.; Dahn, J. R. A Comparative Study of Vinylene Carbonate and Fluoroethylene Carbonate Additives for LiCoO2 /Graphite Pouch Cells. *J. Electrochem. Soc.*, **2014**, *161* (4), A467–A472. https://doi.org/10.1149/2.001404jes.

[142] McMillan, R.; Slegr, H.; Shu, Z. X.; Wang, W. Fluoroethylene Carbonate Electrolyte and Its Use in Lithium Ion Batteries with Graphite Anodes. *J. Power Sources*, **1999**, *81–82*, 20–26. https://doi.org/10.1016/S0378-7753(98)00201-8.

[143] Markevich, E.; Salitra, G.; Aurbach, D. Fluoroethylene Carbonate as an Important Component for the Formation of an Effective Solid Electrolyte Interphase on Anodes and Cathodes for Advanced Li-Ion Batteries. *ACS Energy Lett.*, **2017**, *2* (6), 1337–1345. https://doi.org/10.1021/acsenergylett.7b00163.

[144] Markevich, E.; Salitra, G.; Fridman, K.; Sharabi, R.; Gershinsky, G.; Garsuch, A.; Semrau, G.; Schmidt, M. A.; Aurbach, D. Fluoroethylene Carbonate as an Important Component in Electrolyte Solutions for High-Voltage Lithium Batteries: Role of Surface Chemistry. *ACS Energy Lett.*, **2017**, *2* (6), 1337–1345.

[145] Im, J.; Lee, J.; Ryou, M.-H.; Lee, Y. M.; Cho, K. Y. Fluorinated Carbonate-Based Electrolyte for High-Voltage Li(Ni 0.5 Mn 0.3 Co 0.2)O 2 /Graphite Lithium-Ion Battery . *J. Electrochem. Soc.*, **2017**, *164* (1), A6381–A6385. https://doi.org/10.1149/2.0591701jes.

[146] Zhang, X. Q.; Cheng, X. B.; Chen, X.; Yan, C.; Zhang, Q. Fluoroethylene Carbonate Additives to Render Uniform Li Deposits in Lithium Metal Batteries. *Adv. Funct. Mater.*, **2017**, *27* (10). https://doi.org/10.1002/adfm.201605989.

[147] Ryou, M. H.; Han, G. B.; Lee, Y. M.; Lee, J. N.; Lee, D. J.; Yoon, Y. O.; Park, J. K. Effect of Fluoroethylene Carbonate on High Temperature Capacity Retention of LiMn2O4/Graphite Li-Ion Cells. *Electrochim. Acta*, **2010**, *55* (6), 2073–2077. https://doi.org/10.1016/j.electacta.2009.11.036.

[148] Park, J.; Choi, I.; Lee, M. J.; Kim, M. H.; Lim, T.; Park, K. H.; Jang, J.; Oh, S. M.; Cho, S. K.; Kim, J. J. Effect of Fluoroethylene Carbonate on Electrochemical Battery Performance and the Surface Chemistry of Amorphous MoO2 Lithium-Ion Secondary Battery Negative Electrodes. *Electrochim. Acta*, **2014**, *132*, 338–346.

https://doi.org/10.1016/j.electacta.2014.03.173.

[149] Jaumann, T.; Balach, J.; Langklotz, U.; Sauchuk, V.; Fritsch, M.; Michaelis, A.; Teltevskij, V.; Mikhailova, D.; Oswald, S.; Klose, M.; et al. Lifetime vs. Rate Capability: Understanding the Role of FEC and VC in High-Energy Li-Ion Batteries with Nano-Silicon Anodes. *Energy Storage Mater.*, **2017**, *6* (May 2016), 26–35. https://doi.org/10.1016/j.ensm.2016.08.002.

[150] Park, Y.; Shin, S. H.; Hwang, H.; Lee, S. M.; Kim, S. P.; Choi, H. C.; Jung, Y. M. Investigation of Solid Electrolyte Interface (SEI) Film on LiCoO 2 Cathode in Fluoroethylene Carbonate (FEC)-Containing Electrolyte by 2D Correlation X-Ray Photoelectron Spectroscopy (XPS). *J. Mol. Struct.*, **2014**, *1069* (1), 157–163. https://doi.org/10.1016/j.molstruc.2014.01.041.

[151] Profatilova, I. A.; Kim, S. S.; Choi, N. S. Enhanced Thermal Properties of the Solid Electrolyte Interphase Formed on Graphite in an Electrolyte with Fluoroethylene Carbonate. *Electrochim. Acta*, **2009**, *54* (19), 4445–4450. https://doi.org/10.1016/j.electacta.2009.03.032.

[152] Shkrob, I. A.; Wishart, J. F.; Abraham, D. P. What Makes Fluoroethylene Carbonate Different? *J. Phys. Chem. C*, **2015**, *119* (27), 14954–14964. https://doi.org/10.1021/acs.jpcc.5b03591.

[153] Zhao, X.; Zhuang, Q. C.; Xu, S. D.; Xu, Y. X.; Shi, Y. L.; Zhang, X. X. A New Insight into the Content Effect of Fluoroethylene Carbonate as a Film Forming Additive for Lithium-Ion Batteries. *Int. J. Electrochem. Sci.*, **2015**, *10* (3), 2515–2534.

[154] Okuno, Y.; Ushirogata, K.; Sodeyama, K.; Tateyama, Y. Decomposition of the Fluoroethylene Carbonate Additive and the Glue Effect of Lithium Fluoride Products for the Solid Electrolyte Interphase: An Ab Initio Study. *Phys. Chem. Chem. Phys.*, **2016**, *18* (12), 8643–8653. https://doi.org/10.1039/c5cp07583a.

[155] Nie, M.; Demeaux, J.; Young, B. T.; Heskett, D. R.; Chen, Y.; Bose, A.; Woicik, J. C.; Lucht, B. L. Effect of Vinylene Carbonate and Fluoroethylene Carbonate on SEI Formation on Graphitic Anodes in Li-Ion Batteries. *J. Electrochem. Soc.*, **2015**, *162* (13), A7008–A7014. https://doi.org/10.1149/2.0021513jes.

[156] Liu, D.; Qian, K.; He, Y. B.; Luo, D.; Li, H.; Wu, M.; Kang, F.; Li, B. Positive Film-Forming Effect of Fluoroethylene Carbonate (FEC) on High-Voltage Cycling with Three-Electrode LiCoO2/Graphite Pouch Cell. *Electrochim. Acta*, **2018**, *269*, 378–387. https://doi.org/10.1016/j.electacta.2018.02.151.

[157] Hu, Y.; Kong, W.; Li, H.; Huang, X.; Chen, L. Experimental and Theoretical Studies on Reduction Mechanism of Vinyl Ethylene Carbonate on Graphite Anode for Lithium Ion Batteries. *Electrochem. commun.*, **2004**, *6* (2), 126–131. https://doi.org/10.1016/j.elecom.2003.10.024.

[158] Chen, G.; Zhuang, G. V.; Richardson, T. J.; Liu, G.; Ross, P. N. Anodic Polymerization of Vinyl Ethylene Carbonate in Li-Ion Battery Electrolyte. *Electrochem. Solid-State Lett.*, **2005**, *8* (7). https://doi.org/10.1149/1.1921127.

[159] Tsubouchi, S.; Domi, Y.; Doi, T.; Ochida, M.; Nakagawa, H.; Yamanaka, T.; Abe, T.; Ogumi, Z. Spectroscopic Characterization of Surface Films Formed on Edge Plane

Graphite in Ethylene Carbonate-Based Electrolytes Containing Film-Forming Additives. *J. Electrochem. Soc.*, **2012**, *159* (11), A1786–A1790. https://doi.org/10.1149/2.028211jes.

[160] Xu, S. D.; Zhuang, Q. C.; Wang, J.; Xu, Y. Q.; Zhu, Y. B. New Insight into Vinylethylene Carbonate as a Film Forming Additive to Ethylene Carbonate-Based Electrolytes for Lithium-Ion Batteries. *Int. J. Electrochem. Sci.*, **2013**, *8* (6), 8058–8076.

[161] Petibon, R.; Rotermund, L.; Nelson, K. J.; Gozdz, A. S.; Xia, J.; Dahn, J. R. Study of Electrolyte Components in Li Ion Cells Using Liquid-Liquid Extraction and Gas Chromatography Coupled with Mass Spectrometry. *J. Electrochem. Soc.*, **2014**, *161* (6), A1167–A1172. https://doi.org/10.1149/2.117406jes.

[162] Petibon, R.; Henry, E. C.; Burns, J. C.; Sinha, N. N.; Dahn, J. R. Comparative Study of Vinyl Ethylene Carbonate (VEC) and Vinylene Carbonate (VC) in LiCoO 2 /Graphite Pouch Cells Using High Precision Coulometry and Electrochemical Impedance Spectroscopy Measurements on Symmetric Cells . *J. Electrochem. Soc.*, **2014**, *161* (1), A66–A74. https://doi.org/10.1149/2.030401jes.

[163] Zuo, X.; Wu, J.; Zhao, M.; Wang, C.; Liu, J.; Nan, J. Vinyl Ethylene Carbonate as an Electrolyte Additive for High-Voltage LiNi0.4Mn0.4Co0.2O2/Graphite Li-Ion Batteries. *Ionics (Kiel).*, **2016**, *22* (2), 201–208. https://doi.org/10.1007/s11581-015-1536-6.

[164] Forestier, C.; Jankowski, P.; Wizner, A.; Davoisne, C.; Gachot, G.; Sannier, L.; Grugeon, S.; Johansson, P.; Armand, M.; Laruelle, S. Comparative Investigation of Solid Electrolyte Interphases Created by the Electrolyte Additives Vinyl Ethylene Carbonate and Dicyano Ketene Vinyl Ethylene Acetal. *J. Power Sources*, **2017**, *345*, 212–220. https://doi.org/10.1016/j.jpowsour.2017.01.131.

[165] Shu, Z. X.; McMillan, R. S.; Murray, J. J.; Davidson, I. J. Use of Chloroethylene Carbonate as an Electrolyte Solvent for a Lithium Ion Battery Containing a Graphitic Anode. *J. Electrochem. Soc.*, **1995**, *142* (9), L161–L162. https://doi.org/10.1149/1.2048734.

[166] Shu, Z. X.; McMillan, R. S.; Murray, J. J.; Davidson, I. J. Use of Chloroethylene Carbonate as an Electrolyte Solvent for a Graphite Anode in a Lithium-Ion Battery. *J. Electrochem. Soc.*, **1996**, *143* (7), 2230–2235. https://doi.org/10.1149/1.2048734.

[167] Winter, M.; Novák, P. Chloroethylene Carbonate, a Solvent for Lithium-Ion Cells, Evolving CO 2 during Reduction. *J. Electrochem. Soc.*, **1998**, *145* (2), L27–L30. https://doi.org/10.1149/1.1838270.

[168] Winter, M.; Imhof, R.; Joho, F.; Novák, P. FTIR and DEMS Investigations on the Electroreduction of Chloroethylene Carbonate-Based Electrolyte Solutions for Lithium-Ion Cells. *J. Power Sources*, **1999**, *81–82*, 818–823. https://doi.org/10.1016/S0378-7753(99)00116-0.

[169] Larkin, P. J. *Infrared and Raman Spectroscopy Principles and Spectral Interpretation*; 2011. https://doi.org/10.1016/b978-0-12-804162-8.00001-x.

[170] Fleischmann, M.; Hendra, P. J.; McQuillan, A. . Raman Spectra of Piridyne Adsorbed at a Silver Electrode. *Chem. Phys. Lett.*, **1974**, *26* (2), 163–166. https://doi.org/10.1021/acsami.6b02905.

[171] Pilot, R.; Signorini, R.; Durante, C.; Orian, L.; Bhamidipati, M.; Fabris, L. A Review on Surface-Enhanced Raman Scattering. *Biosensors*, **2019**, *9* (2). https://doi.org/10.3390/bios9020057.

[172] Messinger, B. J.; Von Raben, K. U.; Chang, R. K.; Barber, P. W. Local Fields at the Surface of Noble-Metal Microspheres. *Phys. Rev. B*, **1981**, *24* (2), 649–657. https://doi.org/10.1103/PhysRevB.24.649.

[173] Baddour-Hadjean, R.; Pereira-Ramos, J. P. Raman Microspectrometry Applied to the Study of Electrode Materials for Lithium Batteries. *AIP Conf. Proc.*, **2010**, *1267*, 1137–1138. https://doi.org/10.1063/1.3482342.

[174] Stancovski, V.; Badilescu, S. In Situ Raman Spectroscopic-Electrochemical Studies of Lithium-Ion Battery Materials: A Historical Overview. *J. Appl. Electrochem.*, **2014**, *44* (1), 23–43. https://doi.org/10.1007/s10800-013-0628-0.

[175] Li, H.; Mo, Y.; Pei, N.; Xu, X.; Huang, X.; Chen, L. Surface-Enhanced Raman Scattering Study on Passivating Films of Ag Electrodes in Lithium Batteries. *J. Phys. Chem. B*, **2000**, *104* (35), 8477–8480. https://doi.org/10.1021/jp000837g.

[176] Ha, Y.; Tremolet De Villers, B. J.; Li, Z.; Xu, Y.; Stradins, P.; Zakutayev, A.; Burrell, A.; Han, S. D. Probing the Evolution of Surface Chemistry at the Silicon-Electrolyte Interphase via in Situ Surface-Enhanced Raman Spectroscopy. *J. Phys. Chem. Lett.*, **2020**, *11* (1), 286–291. https://doi.org/10.1021/acs.jpclett.9b03284.

[177] Liu, K.; Yu, Z.; Zhu, X.; Zhang, S.; Zou, F.; Zhu, Y. A Universal Surface Enhanced Raman Spectroscopy (SERS)-Active Graphene Cathode for Lithium-Air Batteries. *RSC Adv.*, **2016**, *6* (104), 102272–102279. https://doi.org/10.1039/c6ra23331g.

[178] Tang, S.; Gu, Y.; Yi, J.; Zeng, Z.; Ding, S. Y.; Yan, J. W.; Wu, D. Y.; Ren, B.; Tian, Z. Q.; Mao, B. W. An Electrochemical Surface-Enhanced Raman Spectroscopic Study on Nanorod-Structured Lithium Prepared by Electrodeposition. *J. Raman Spectrosc.*, **2016**, *47* (9), 1017–1023. https://doi.org/10.1002/jrs.4970.

[179] Schmitz, R.; Ansgar Müller, R.; Wilhelm Schmitz, R.; Schreiner, C.; Kunze, M.; Lex-Balducci, A.; Passerini, S.; Winter, M. SEI Investigations on Copper Electrodes after Lithium Plating with Raman Spectroscopy and Mass Spectrometry. *J. Power Sources*, **2013**, *233*, 110–114. https://doi.org/10.1016/j.jpowsour.2013.01.105.

[180] Chen, D.; Mahmoud, M. A.; Wang, J. H.; Waller, G. H.; Zhao, B.; Qu, C.; El-Sayed, M. A.; Liu, M. Operando Investigation into Dynamic Evolution of Cathode-Electrolyte Interfaces in a Li-Ion Battery. *Nano Lett.*, **2019**, *19* (3), 2037–2043. https://doi.org/10.1021/acs.nanolett.9b00179.

[181] Nanda, J.; Yang, G.; Hou, T.; Voylov, D. N.; Li, X.; Ruther, R. E.; Naguib, M.; Persson, K.; Veith, G. M.; Sokolov, A. P. Unraveling the Nanoscale Heterogeneity of Solid Electrolyte Interphase Using Tip-Enhanced Raman Spectroscopy. *Joule*, **2019**, *3* (8), 2001–2019. https://doi.org/10.1016/j.joule.2019.05.026.

[182] Cabo-Fernandez, L.; Bresser, D.; Braga, F.; Passerini, S.; Hardwick, L. J. In-Situ Electrochemical SHINERS Investigation of SEI Composition on Carbon-Coated Zn0.9Fe0.1O Anode for Lithium-Ion Batteries. *Batter. Supercaps*, **2019**, *2* (2), 168–177. https://doi.org/10.1002/batt.201800063.

[183] Lin, K. Q.; Yi, J.; Zhong, J. H.; Hu, S.; Liu, B. J.; Liu, J. Y.; Zong, C.; Lei, Z. C.; Wang, X.; Aizpurua, J.; et al. Plasmonic Photoluminescence for Recovering Native Chemical Information from Surface-Enhanced Raman Scattering. *Nat. Commun.*, **2017**, *8*. https://doi.org/10.1038/ncomms14891.

[184] Galloway, T. A.; Cabo-Fernandez, L.; Aldous, I. M.; Braga, F.; Hardwick, L. J. Shell Isolated Nanoparticles for Enhanced Raman Spectroscopy Studies in Lithium-Oxygen Cells. *Faraday Discuss.*, **2017**, *205*, 469–490. https://doi.org/10.1039/c7fd00151g.

[185] Gajan, A.; Lecourt, C.; Torres Bautista, B. E.; Fillaud, L.; Demeaux, J.; Lucas, I. T. Solid Electrolyte Interphase Instability in Operating Lithium-Ion Batteries Unraveled by Enhanced-Raman Spectroscopy. *ACS Energy Lett.*, **2021**, *6* (5), 1757–1763. https://doi.org/10.1021/acsenergylett.1c00436.

[186] Hy, S.; Felix; Chen, Y. H.; Liu, J. Y.; Rick, J.; Hwang, B. J. In Situ Surface Enhanced Raman Spectroscopic Studies of Solid Electrolyte Interphase Formation in Lithium Ion Battery Electrodes. *J. Power Sources*, **2014**, *256*, 324–328. https://doi.org/10.1016/j.jpowsour.2014.01.092.

[187] Schmiegel, J. Unraveling the Working Mechanism of Tailor - Made Electrolyte Additives for High - Energy Lithium Ion Batteries, Westfälischen Wilhelms-Universität Münster, 2021.

[188] Solchenbach, S.; Pritzl, D.; Kong, E. J. Y.; Landesfeind, J.; Gasteiger, H. A. A Gold Micro-Reference Electrode for Impedance and Potential Measurements in Lithium Ion Batteries. *J. Electrochem. Soc.*, **2016**, *163* (10), A2265–A2272. https://doi.org/10.1149/2.0581610jes.

[189] Shan, X.; Zhong, Y.; Zhang, L.; Zhang, Y.; Xia, X.; Wang, X.; Tu, J. A Brief Review on Solid Electrolyte Interphase Composition Characterization Technology for Lithium Metal Batteries: Challenges and Perspectives. *J. Phys. Chem. C*, **2021**, *125* (35), 19060–19080. https://doi.org/10.1021/acs.jpcc.1c06277.

[190] Edström, K.; Herstedt, M.; Abraham, D. P. A New Look at the Solid Electrolyte Interphase on Graphite Anodes in Li-Ion Batteries. *J. Power Sources*, **2006**, *153* (2), 380–384. https://doi.org/10.1016/j.jpowsour.2005.05.062.

[191] Tripathi, A. M.; Su, W. N.; Hwang, B. J. In Situ Analytical Techniques for Battery Interface Analysis. *Chem. Soc. Rev.*, **2018**, *47* (3), 736–751. https://doi.org/10.1039/c7cs00180k.

[192] Haryanto, A.; Lee, C. W. Shell Isolated Nanoparticle Enhanced Raman Spectroscopy for Mechanistic Investigation of Electrochemical Reactions. *Nano Converg.*, **2022**, *9* (1), 1–14. https://doi.org/10.1186/s40580-022-00301-1.

[193] Horsthemke, F.; Winkler, V.; Diehl, M.; Winter, M.; Nowak, S. Concept for the Analysis of the Electrolyte Composition within the Cell Manufacturing Process: From Sealing to Sample Preparation. *Energy Technol.*, **2020**, *8* (2), 1–4. https://doi.org/10.1002/ente.201801081.

[194] Peschel, C.; Horsthemke, F.; Winter, M.; Nowak, S. Implementation of Orbitrap Mass Spectrometry for Improved GC-MS Target Analysis in Lithium Ion Battery Electrolytes. *MethodsX*, **2022**, *9*, 101621. https://doi.org/10.1016/j.mex.2022.101621.

[195] Peschel, C.; Nowak, S.; Roberts, D. Identification of Lithium-Ion Battery Degradation Products Using GC Orbitrap Mass Spectrometry. *Thermo Fish. Tech. Note 00413*, **2022**.

[196] Li, J. F.; Tian, X. D.; Li, S. B.; Anema, J. R.; Yang, Z. L.; Ding, Y.; Wu, Y. F.; Zeng, Y. M.; Chen, Q. Z.; Ren, B.; et al. Surface Analysis Using Shell-Isolated Nanoparticle-Enhanced Raman Spectroscopy. *Nat. Protoc.*, **2013**, *8* (1), 52–65. https://doi.org/10.1038/nprot.2012.141.

[197] Fu, J.; Mu, D.; Wu, B.; Bi, J.; Liu, X.; Peng, Y.; Li, Y.; Wu, F. Enhanced Electrochemical Performance of LiNi0.6Co0.2Mn0.2O2 Cathode at High Cutoff Voltage by Modifying Electrode/Electrolyte Interface with Lithium Metasilicate. *Electrochim. Acta*, **2017**, *246*, 27–34. https://doi.org/10.1016/j.electacta.2017.06.038.

[198] Kubot, M.; von Holtum, B.; Winter, M.; Wiemers-Meyer, S.; Nowak, S. Organofluorophosphates as Oxidative Degradation Products in High-Voltage Lithium Ion Batteries with NMC or LNMO Cathodes. *J. Electrochem. Soc.*, **2022**, *169* (11), 110534. https://doi.org/10.1149/1945-7111/aca2e8.

[199] Zhu, J.; Mathews, I.; Ren, D.; Li, W.; Cogswell, D.; Xing, B.; Sedlatschek, T.; Kantareddy, S. N. R.; Yi, M.; Gao, T.; et al. End-of-Life or Second-Life Options for Retired Electric Vehicle Batteries. *Cell Reports Phys. Sci.*, **2021**, *2* (8), 100537. https://doi.org/10.1016/j.xcrp.2021.100537.

[200] Jung, R.; Metzger, M.; Maglia, F.; Stinner, C.; Gasteiger, H. A. Oxygen Release and Its Effect on the Cycling Stability of LiNi x Mn y Co z O 2 (NMC) Cathode Materials for Li-Ion Batteries . *J. Electrochem. Soc.*, **2017**, *164* (7), A1361–A1377. https://doi.org/10.1149/2.0021707jes.

[201] Osaka, T.; Momma, T.; Mukoyama, D.; Nara, H. Proposal of Novel Equivalent Circuit for Electrochemical Impedance Analysis of Commercially Available Lithium Ion Battery. *J. Power Sources*, **2012**, *205*, 483–486. https://doi.org/10.1016/j.jpowsour.2012.01.070.

[202] Meddings, N.; Heinrich, M.; Overney, F.; Lee, J. S.; Ruiz, V.; Napolitano, E.; Seitz, S.; Hinds, G.; Raccichini, R.; Gaberšček, M.; et al. Application of Electrochemical Impedance Spectroscopy to Commercial Li-Ion Cells: A Review. *J. Power Sources*, **2020**, *480* (August). https://doi.org/10.1016/j.jpowsour.2020.228742.

[203] Yoshida, H.; Fukunaga, T.; Hazama, T.; Terasaki, M.; Mizutani, M.; Yamachi, M. Degradation Mechanism of Alkyl Carbonate Solvents Used in Lithium-Ion Cells during Initial Charging. *J. Power Sources*, **1997**, *68* (2), 311–315. https://doi.org/10.1016/S0378-7753(97)02635-9.

[204] Henschel, J.; Peschel, C.; Klein, S.; Horsthemke, F.; Winter, M.; Nowak, S. Clarification of Decomposition Pathways in a State-of-the-Art Lithium Ion Battery Electrolyte through 13C-Labeling of Electrolyte Components. *Angew. Chemie - Int. Ed.*, **2020**, *59* (15), 6128–6137. https://doi.org/10.1002/anie.202000727.

[205] chloromethyl ethyl ester https://scifinder-n.cas.org/searchDetail/substance/6164505df373d914af77d008/substanceDetails (accessed Jan 25, 2023).

[206] 1-chloroethyl methyl ester https://scifinder-

n.cas.org/searchDetail/substance/6164505df373d914af77d008/substanceDetails (accessed Jan 25, 2023).

[207] 2-chloroethyl methyl ester https://scifinder-n.cas.org/searchDetail/substance/6164505df373d914af77d008/substanceDetails (accessed Jan 25, 2023).

[208] Rosser, T. E.; Dickinson, E. J. F.; Raccichini, R.; Hunter, K.; Searle, A. D.; Kavanagh, C. M.; Curran, P. J.; Hinds, G.; Park, J.; Wain, A. J. Improved Operando Raman Cell Configuration for Commercially-Sourced Electrodes in Alkali-Ion Batteries. *J. Electrochem. Soc.*, **2021**, *168* (7), 070541. https://doi.org/10.1149/1945-7111/ac132d.

[209] Naudin, C.; Bruneel, J. L.; Chami, M.; Desbat, B.; Grondin, J.; Lassègues, J. C.; Servant, L. Characterization of the Lithium Surface by Infrared and Raman Spectroscopies. *J. Power Sources*, **2003**, *124* (2), 518–525. https://doi.org/10.1016/S0378-7753(03)00798-5.

[210] Piernas-Muñoz, M. J.; Tornheim, A.; Trask, S.; Zhang, Z.; Bloom, I. Surface-Enhanced Raman Spectroscopy (SERS): A Powerful Technique to Study the SEI Layer in Batteries. *Chem. Commun.*, **2021**, *57* (18), 2253–2256. https://doi.org/10.1039/d0cc08001b.

[211] Sokrates, G. *Infrared and Raman Characteristic Group Frequencies*; 2001. https://doi.org/10.1093/occmed/kqs085.

[212] Li, G.; Li, H.; Mo, Y.; Chen, L.; Huang, X. Further Identification to the SEI Film on Ag Electrode in Lithium Batteries by Surface Enhanced Raman Scattering (SERS). *J. Power Sources*, **2002**, *104* (2), 190–194. https://doi.org/10.1016/S0378-7753(01)00908-9.

[213] Schwenke, K. U.; Solchenbach, S.; Demeaux, J.; Lucht, B. L.; Gasteiger, H. A. The Impact of CO2 Evolved from VC and FEC during Formation of Graphite Anodes in Lithium-Ion Batteries. *J. Electrochem. Soc.*, **2019**, *166* (10), A2035–A2047. https://doi.org/10.1149/2.0821910jes.

[214] Wilmshurst, K. J. Vibrational Assignment for Sodium Acetate. *J. Chem. Phys.*, **1955**, *23* (12), 2463. https://doi.org/10.1063/1.1741932.

11 AKNOWLEDGEMENTS

In the end I want to thank everyone that made this work possible, but also who was at my side along it and helped me to get through my degree and complete it.

First of all, I want to thank to my supervisor Masoud Baghernejad who allowed me to work in the Interfacial SpectroElectrochemistry Group. I also want to thank Christoph Peschel, Peter Lennartz, Nella Vargas-Barbosa and Friederike Reiβig for their help respectively for GC-MS, EIS and SEM measurements and analysis. A big thank to my group mates Felix and Matthias for their precious help, fruitful discussion, and support throughout my time at the Helmholtz Institute Muenster. Felix's "jaaa, it's fine" and Matthias' "you look tired" will not be forgotten. To HI MS all, thanks for the possibility to have such an interesting first experience in research: there were struggles, but the fact that I could experience many ups and downs of the academic life will be precious for my future career path.

A great thank to Melanie, my closest colleague and friend. We have befriended immediately, and she has always been there for me, was it for scientific discussion, lunch, dinner, shopping, crying, laughing or a daytrip. With her I also want to thank Angie and Alicia for the nice time together in Münster. From my german experience I must also thank the flatmates of all the WGs that I lived in. Living so close with so many different amazing people really made me grow as a person.

I can't thank enough my family, mum Luigina, dad Gino, my brothers Fabio and Matteo, as well as the in-laws Giorgia and Luca, to have helped me to stay strong, but most of all my sister Claudia: the understanding and patience you had during my hard times and the joy that you brought in my life with Lia kept me standing.

To all the materials science friends. The time of my studies and leisure with you is full of lovely memories and I am really thankful to have shared this path with you, but also, I am grateful and happy to have gained such great friends for life, that have been there besides long distance.

To my “fantagenitori” Miriam and Saif: you are my best friends in the world and being away from you was unspeakably hard, but you found your ways to show up for me always in the right way and I could not be more thankful.

Thank to my friends of a life Anna, Laura, Luca, Camilla and to my skating and life mates Ilaria and Sara for making me feel at home every time I came back.

I would like also to thank all the friends that I have met in Bordeaux, and in particular my study mates and Giorgio, who has shared this adventure with me. I would have never taken this very big jump for my internship if my first study experience abroad had not left me with such good memories, positivity, and faith in my possibilities, that you all helped me to mature a bit more.

Tons of other people has been there for me along this year in one way or another, even when I felt completely alone, and I have you all in my heart.

As last a little thank to myself, to have had the courage to take the opportunity and the persistency to take it to the end despite all.

Alla fine voglio ringraziare tutti coloro che hanno reso possibile questo lavoro, ma anche chi è stato al mio fianco lungo tutto il percorso e mi ha aiutato a portare a termine la mia laurea.

Innanzitutto, voglio ringraziare il mio supervisore Masoud Baghernejad che mi ha permesso di lavorare nel gruppo di spettroelettrochimica interfacciale. Desidero inoltre ringraziare Christoph Peschel, Peter Lennartz, Nella Vargas-Barbosa e Friederike Reißig per il loro aiuto rispettivamente per le misure e analisi di GC-MS, EIS e SEM. Un grande ringraziamento va ai miei compagni di gruppo Felix e Matthias per il loro prezioso aiuto, le proficue discussioni e il sostegno durante tutto il periodo trascorso all'Helmholtz Institute di Muenster. I "jaaa, va bene" di Felix e i "sembri stanca" di Matthias non saranno dimenticati. All'HI MS tutto, grazie per avermi dato la possibilità di fare una prima esperienza di ricerca così interessante: ci sono state difficoltà, ma il fatto di aver potuto sperimentare molti alti e bassi della vita accademica sarà prezioso per il mio futuro percorso professionale.

Un grande ringraziamento a Melanie, la mia più cara collega e amica. Abbiamo fatto subito amicizia e lei è sempre stata presente per me, che si trattasse di discussioni scientifiche, pranzi, cene, shopping, pianti, risate o gite. Con lei voglio ringraziare anche Angie e Alicia per i bei momenti passati insieme a Münster. Per quanto riguarda la mia esperienza tedesca, devo

ringraziare anche i coinquilini di tutte le WG in cui ho vissuto. Vivere a stretto contatto con così tante persone diverse mi ha fatto crescere come persona.

Non ringrazierò mai abbastanza la mia famiglia, mamma Luigina, papà Gino, i miei fratelli Fabio e Matteo, così come i cognati Giorgia e Luca, che mi hanno aiutato a non arrendermi, ma soprattutto mia sorella Claudia: la comprensione e la pazienza che hai avuto nei miei momenti difficili e la gioia che hai portato nella mia vita con Lia mi hanno tenuta in piedi.

A tutti gli amici di scienza dei materiali. Il periodo di studio e di svago trascorso con voi è pieno di bei ricordi e sono davvero grata di aver condiviso questo percorso con voi, ma sono anche grata e felice di aver acquisito amici così fantastici per la vita, che sono stati presenti al di là della lontananza.

Ai miei "fantagenitori" Miriam e Saif: siete i miei migliori amici al mondo e la distanza da voi è stata indicibilmente dura, ma avete trovato il modo di essere presenti per me sempre nel modo giusto e non potrei essere più grata.

Grazie ai miei amici di una vita Anna, Laura, Luca, Camilla e alle mie compagne di pattinaggio e di vita Ilaria e Sara per avermi fatto sentire a casa ogni volta che sono tornata.

Vorrei ringraziare anche tutti gli amici che ho conosciuto a Bordeaux, in particolare i miei compagni di studio e Giorgio, che ha condiviso con me questa avventura. Non avrei mai fatto questo grande salto per il mio tirocinio se la mia prima esperienza di studio all'estero non mi avesse lasciato ricordi così belli, positività e fiducia nelle mie possibilità, che tutti voi mi avete aiutato a maturare un po' di più.

Tante altre persone mi sono state vicine in questo anno in un modo o nell'altro, anche quando mi sentivo completamente sola, e vi porto tutti nel mio cuore.

Infine, un piccolo ringraziamento a me stessa, per aver avuto il coraggio di cogliere l'opportunità e la tenacia di portarla a termine nonostante tutto.

12 APPENDIX

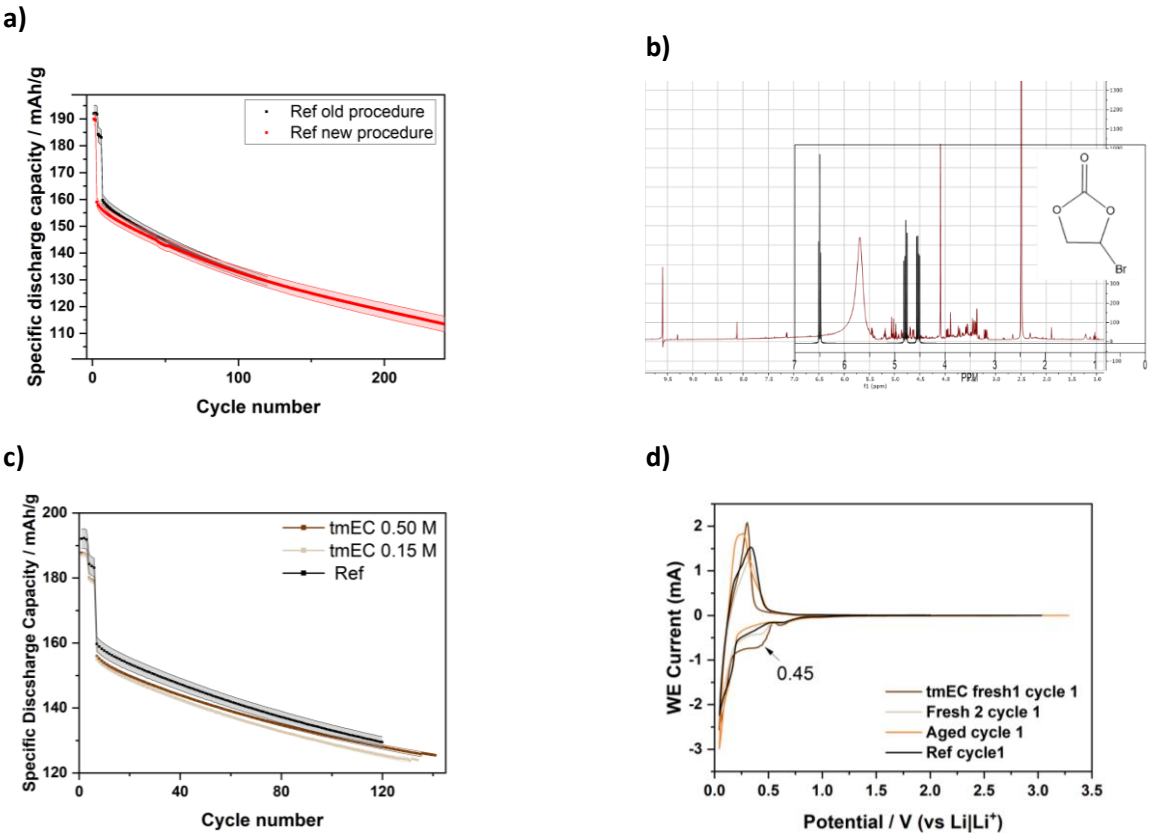

Figure A 1: a) Specific discharge capacity for the reference electrolyte obtained from the two different cycling procedures applied. **b)** Measured NMR of the BrEC additive in DMSO (red) and calculated NMR of BrEC from NIST database (black) **c)** Specific discharge capacity tmEC 0.15 M and 0.5 M **d)** CV of tmEC containing additive and reference, with *aged* indicating the electrolyte stored in dryroom for 2 weeks.

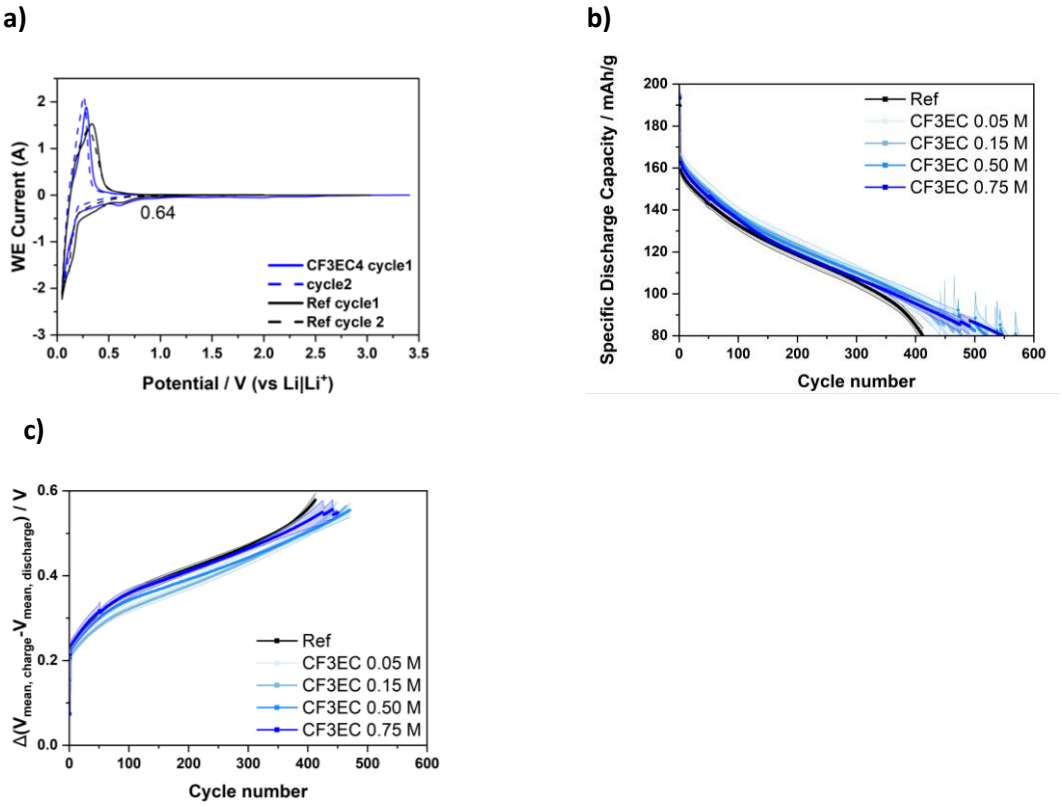

Figure A 2: a) CV of CF_3EC containing additive and reference **b)** Specific discharge capacity for CF3EC investigated concentrations and reference **c)** Difference between average charge and discharge voltage ΔV for CF3EC

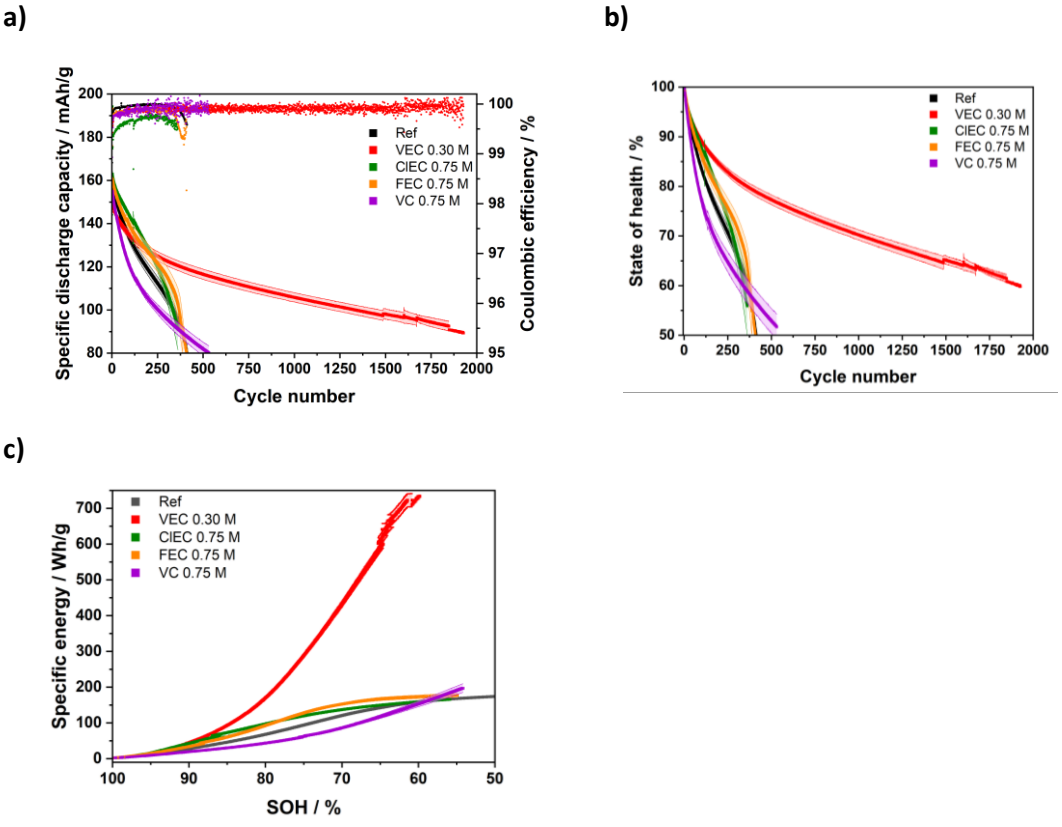

Figure A 3: Complete range data **a)** discharge capacity, **b)** normalized capacity (state of health), **c)** accumulated energy for the optimum concentration of each additive.

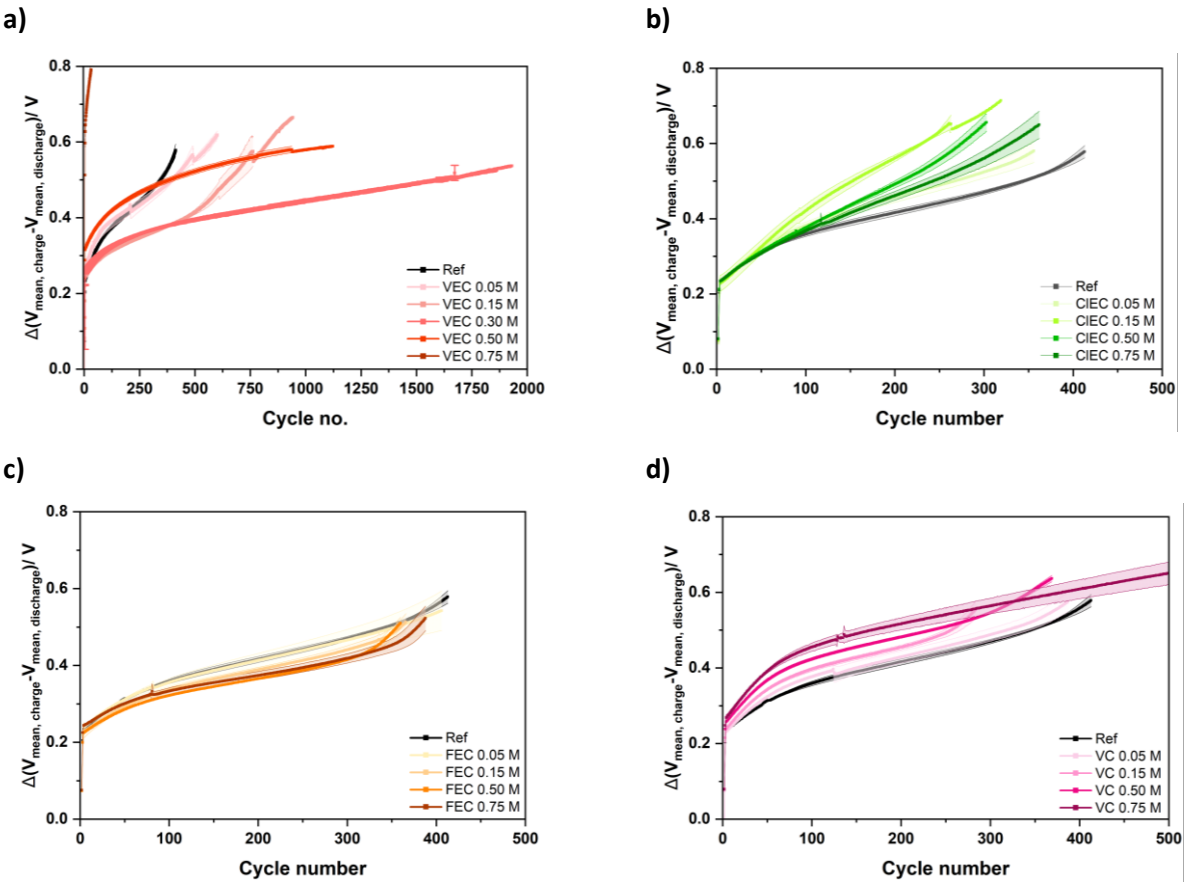

Figure A 4: ΔV for each investigated concentration ***a)*** *VEC,* ***b)*** *ClEC,* ***c)*** *FEC,* ***d)*** *VC*

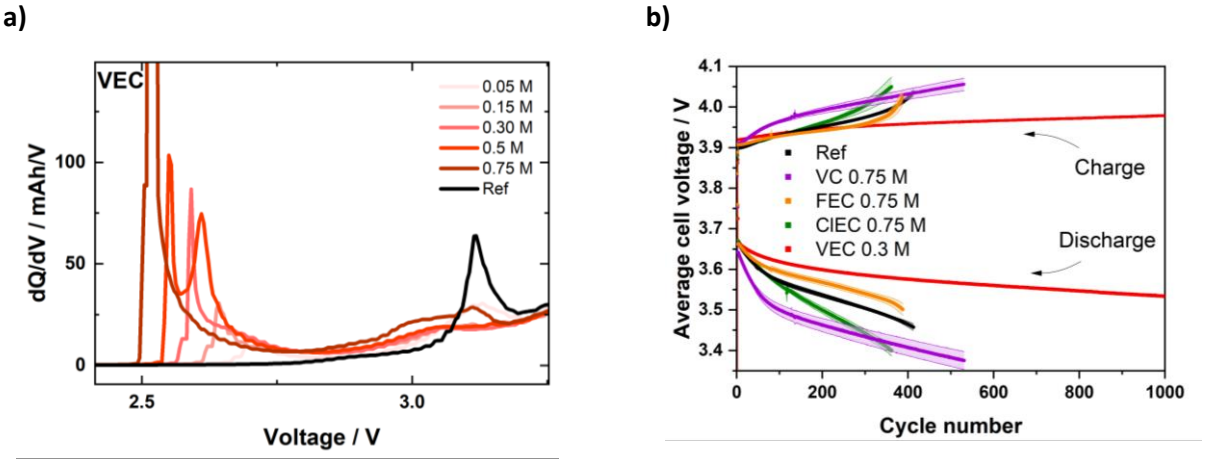

Figure A 5: a) dQ/dV plot for the first charge of VEC investigated concentrations **b)** Average cell voltage during charge and discharge.

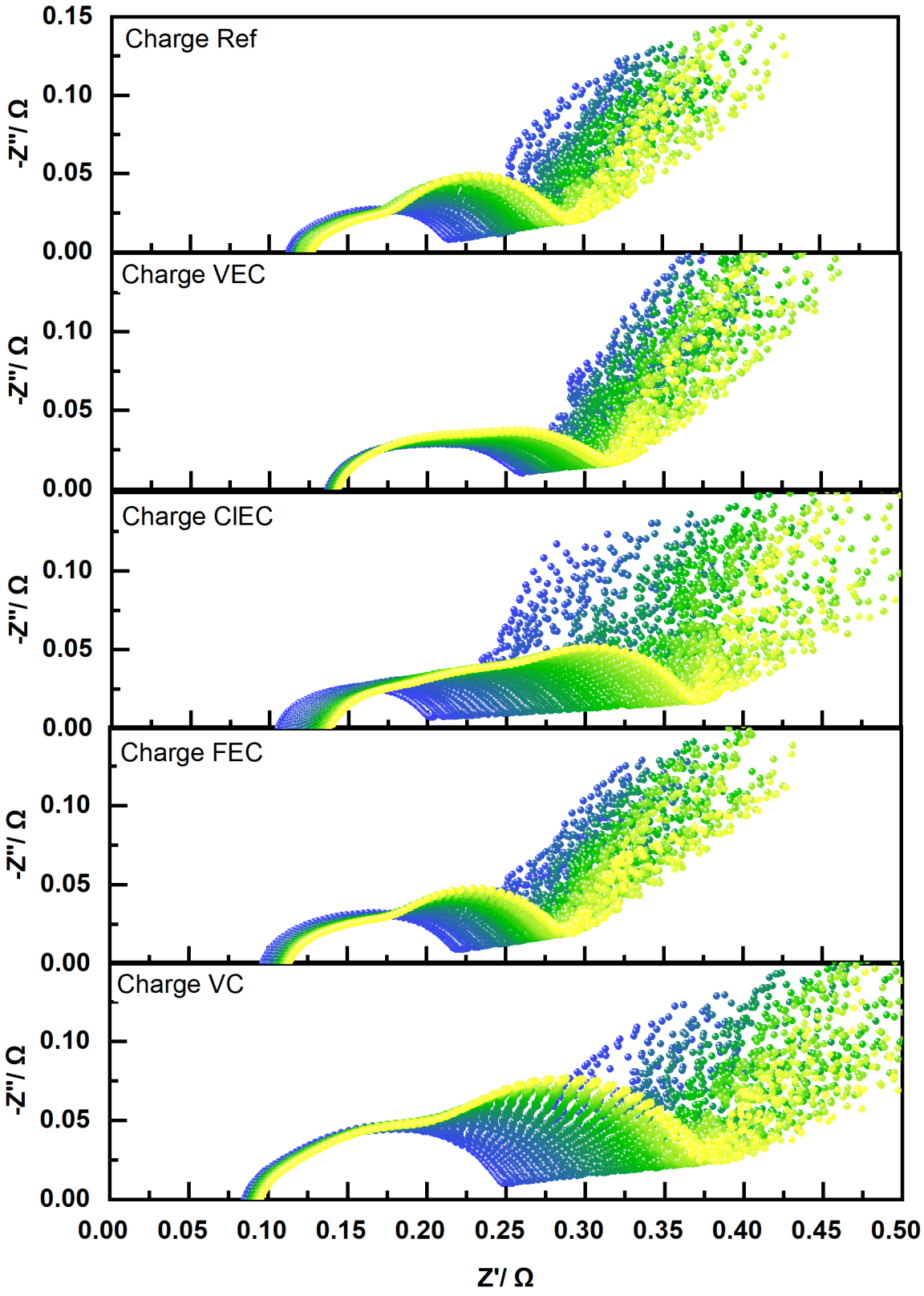

Figure A 6: Nyquist plot for each cycle at 50% SOC during charge for reference and each additive optimum concentration.

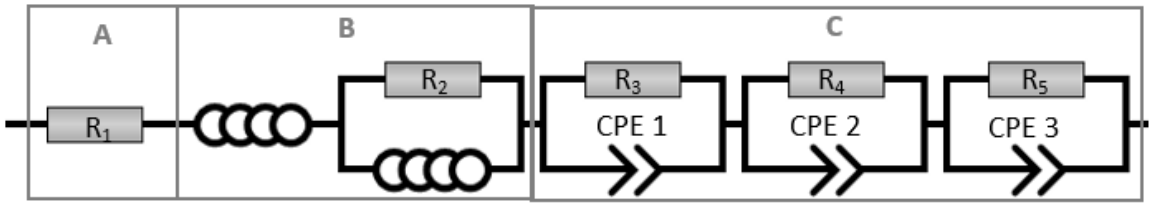

Figure A 7: Equivalent circuit used to fit EIS data. Block A models the ohmic resistance of the electrolyte. Block B is to take in account inductive effects of the external circuitry and from cell geometric effects, evident for data points with -Z"< 0. Block C reproduces the semicircles with so-called ZARC elements, describing the dynamics of the double layer and the charge transfer.

Table A 1: Values of Resistance (R), Q and α of CPE elements from the fitted set of EIS data

1st cycle	**Ref**		**VEC**		**ClEC**		**FEC**		**VC**	
	Value	***Error***	**Value**	***Error***	**Value**	***Error***	**Value**	***Error***	**Value**	***Error***
R1 / Ω	0.1007	*0.0002*	0.1261	*0.0005*	0.0922	*0.0002*	0.0864	*0.0003*	0.0735	*0.0004*
R3 / Ω	0.100	*0.003*	0.060	*0.010*	0.1067	*0.0017*	0.067	*0.004*	0.058	*0.005*
CPE Q 1 / $Fs^{(\alpha-1)}$	0.339	*0.008*	0.144	*0.018*	0.229	*0.004*	0.123	*0.009*	0.142	*0.018*
CPE α1	0.504	*0.004*	0.59	*0.02*	0.522	*0.003*	0.613	*0.001*	0.586	*0.016*
R4 / Ω	0.021	*0.003*	0.081	*0.010*	0.0095	*0.0015*	0.074	*0.004*	0.127	*0.005*
CPE Q 2 / $Fs^{(\alpha-1)}$	0.47	*0.02*	0.47	*0.06*	0.41	*0.05*	0.360	*0.017*	0.164	*0.004*
CPE α2	0.89	*0.04*	0.610	*0.015*	1.00	*0.05*	0.703	*0.010*	0.722	*0.007*
100th cycle										
	Value	***Error***	**Value**	***Error***	**Value**	***Error***	**Value**	***Error***	**Value**	***Error***
R1 / Ω	0.1163	*0.0004*	0.1251	*0.0003*	0.1039	*0.0012*	0.1004	*0.0002*	0.0810	*0.0005*
R3 / Ω	0.090	*0.003*	0.192	*0.004*	0.100	*0.004*	0.1053	*0.0017*	0.081	*0.009*
CPE Q 1 / $Fs^{(\alpha-1)}$	0.48	*0.03*	0.373	*0.013*	0.035	*0.004*	0.2876	*0.011*	0.18	*0.02*
CPE α1	0.477	*0.008*	0.441	*0.004*	0.557	*0.013*	0.510	*0.005*	0.536	*0.015*
R4 / Ω	0.087	*0.002*	0.017	*0.003*	0.057	*0.004*	0.0866	*0.0016*	0.052	*0.007*
CPE Q 2 / $Fs^{(\alpha-1)}$	0.542	*0.007*	1.50	*0.07*	0.116	*0.007*	0.576	*0.006*	0.095	*0.003*
CPE α2	0.944	*0.008*	1.00	*0.05*	0.782	*0.019*	0.913	*0.007*	0.88	*0.02*
R5 / Ω					0.1132	*0.0019*			0.1602	*0.0017*
CPE Q 3 / $Fs^{(\alpha-1)}$					0.480	*0.006*			0.448	*0.004*
CPE α3					0.837	*0.006*			0.887	*0.004*

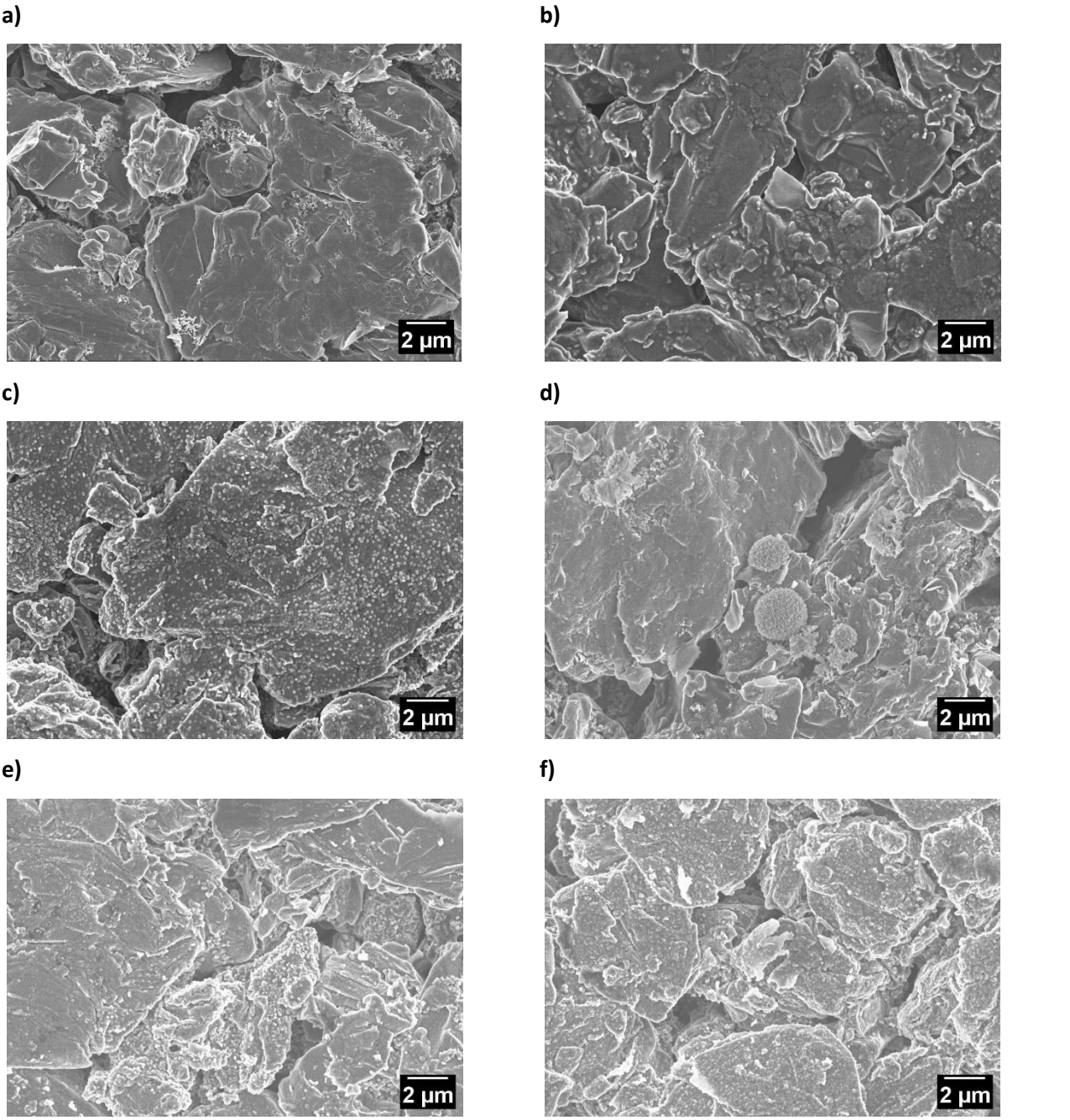

Figure A 8: Scanning Electron Microscopy images of graphite anodes respectively **a)** pristine**,** or after 100 cycles in **b)** reference **c)** VEC **d)** ClEC **e)** FEC **f)** VC electrolytes with optimum additive concentration.

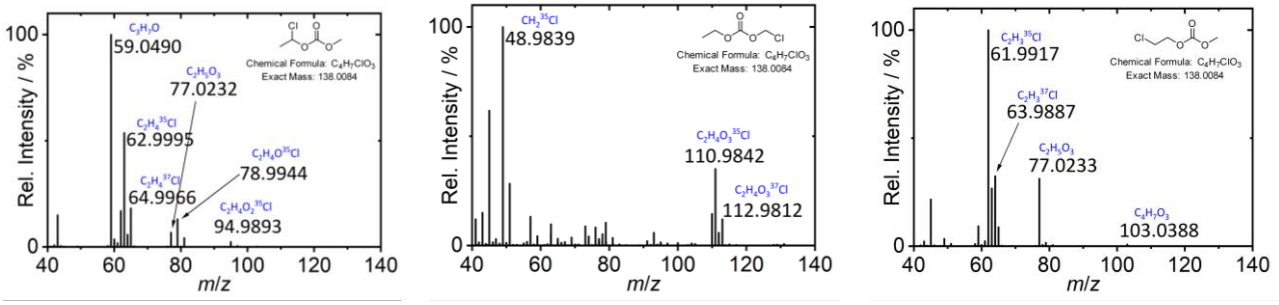

Figure A 9: HRAM-MS fragment pattern for ClEC decomposition products

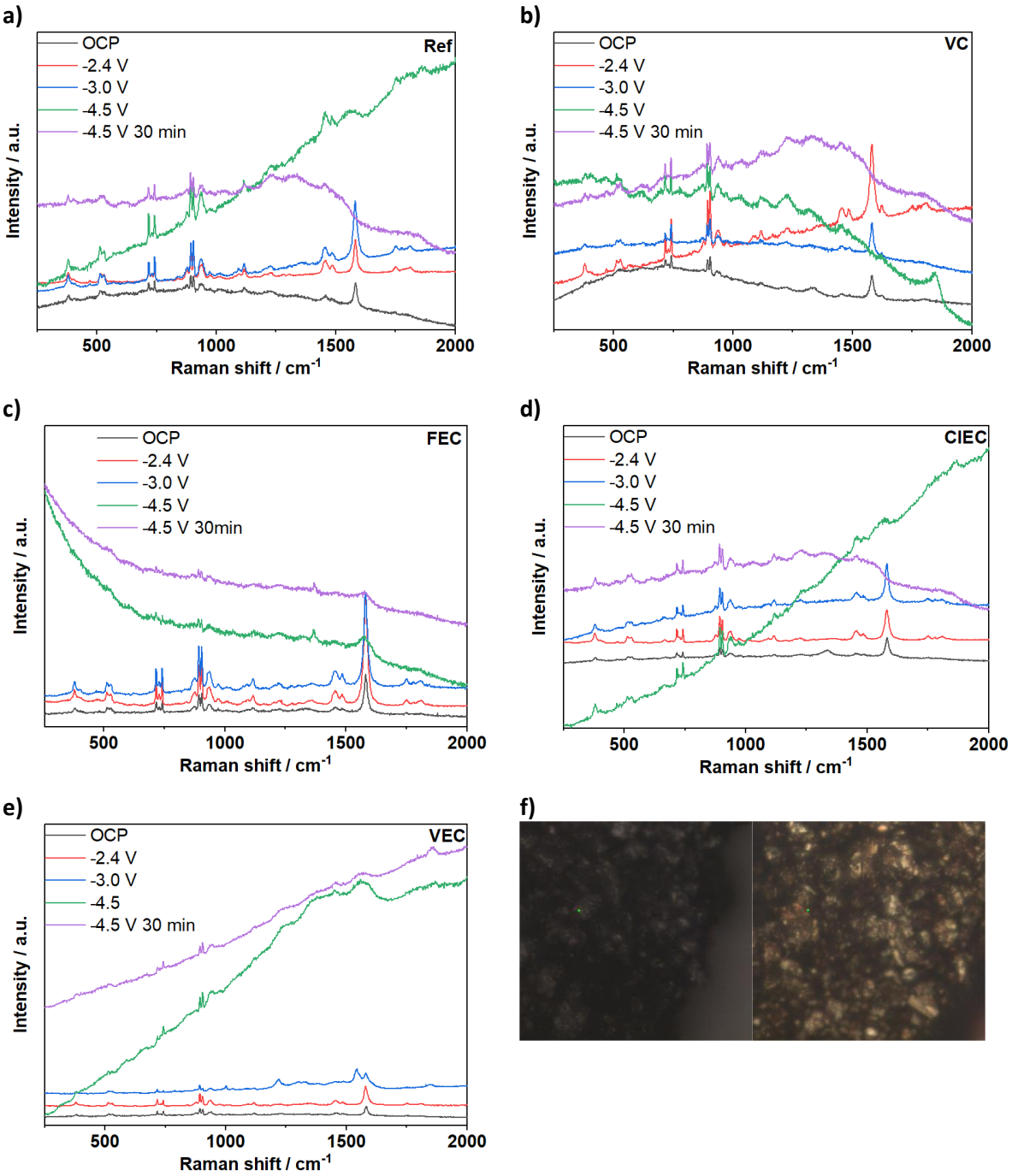

Figure A 10: Unelaborated SHINERS spectra of graphite surface for **a)** Ref (OCP, -4.5 V 30 min red laser, others green laser), **b)** VC (red laser) **c)** FEC (-2.4 V green laser, others green laser) **d)** ClEC (OCP, -4.5 V 30 min red laser, others green laser) **e)** VEC (OCP, -2.4 V red laser, others green laser) at -2.4, -3 and -4.5 V vs NMC. **f)** Microscope image of graphite surface before and after charge, acquired from the Raman microscope at OCP and at the end of charge in the optical cell.

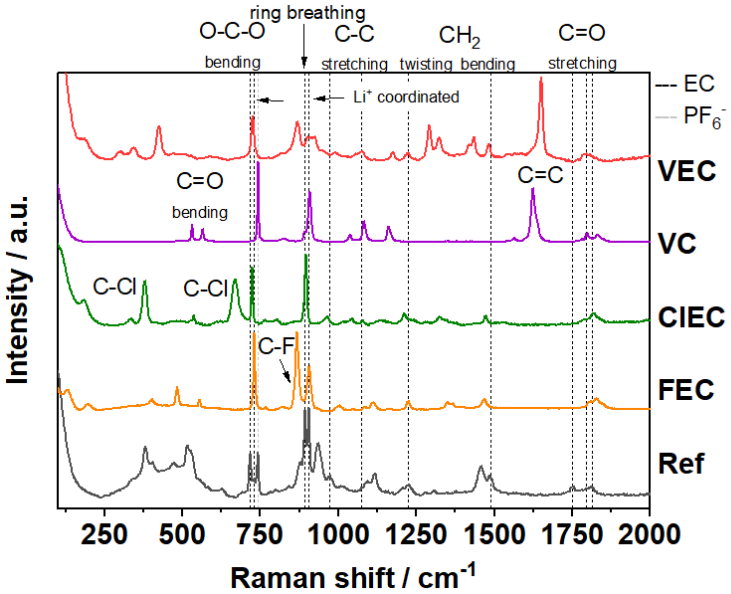

Figure A 11: Spectra of the pure reference electrolyte and pure additives. Baseline corrected with LabSpec 6.6.2. software. All acquired at 100% laser power. Reference red laser, 10 s, 5 acq., FEC red laser, 10 s, 3 acq., ClEC red laser 30 s 3 acq., VC green laser 30 s, 3 acq, VEC green laser, 10 s 3 acq.. Dashed lines indicate EC and PF_6^- peaks as assigned in the figure. Peaks non assigned in reference spectra belong to EMC.[176]